Lattice investigations of the QCD phase diagram

Dissertation

by

Jana Günther

Major: Physics

Matriculation number: 821980

Supervisor: Prof. Dr. Z. Fodor

Hand in date: 15. December 2016

Die Dissertation kann wie folgt zitiert werden:

urn:nbn:de:hbz:468-20170213-111605-3
[http://nbn-resolving.de/urn/resolver.pl?urn=urn%3Anbn%3Ade%3Ahbz%3A468-20170213-111605-3]

Acknowledgement

I want to thank my advisor Prof. Dr. Z. Fodor for the opportunity to work on such fascinating topics. Also I want to thank Szabolcs Borsanyi for his support and the discussions during the last years, as well as for the comments on this thesis.

In addition I want to thank the whole Wuppertal group for the friendly working atmosphere.

I also thank all my co-authors for the joint work in the various projects.

Special thanks I want to say to Lukas Varnhorst and my family for their support throughout my whole studies.

I gratefully acknowledge the Gauss Centre for Supercomputing (GCS) for providing computing time for a GCS Large-Scale Project on the GCS share of the supercomputer JUQUEEN [1] at Jülich Supercomputing Centre (JSC). GCS is the alliance of the three national supercomputing centres HLRS (Universität Stuttgart), JSC (Forschungszentrum Jülich), and LRZ (Bayerische Akademie der Wissenschaften), funded by the German Federal Ministry of Education and Research (BMBF) and the German State Ministries for Research of Baden-Württemberg (MWK), Bayern (StMWFK) and Nordrhein-Westfalen (MIWF).

I am also grateful to the DFG for the SFB/TR55 grant and the GSI for their scholarship that I was working on during the last years.

Contents

1 Introduction

The theory of the big bang describes the evolution of our Universe. It starts from a state with high temperature and pressure. During the expansion it cools down to today's temperature measured from the cosmic microwave background of approximately 3 K. In the course of this extreme cooling several cross-over transitions happen leading to our matter today. [2, 3]

The metric of the Universe was found by Friedmann as

$$\mathrm{d}s^2 = \mathrm{d}t^2 - a^2(t)(\mathrm{d}x^2 + \mathrm{d}y^2 + \mathrm{d}z^2) \tag{1.1}$$

where a is the so called scale factor. With the Einstein equations the energy conservation can be written in the form

$$\dot{\rho}a^3 - 3(\rho + p)a^2\dot{a} = 0 \tag{1.2}$$

with the energy density ρ and the pressure p of both matter and radiation [2]. To describe the development of the Universe one needs the equation of state that relates energy density and pressure. It can be obtained from calculations in the framework of the standard model of particle physics.

However in today's Universe only a fraction of the matter in our Universe is made of baryonic matter, which is described by the standard model. We know, for example from the rotation curves of galaxies and from the large scale structures in the Universe, that there must be some form of matter that does interact through gravity and only very weakly, if at all, though other forces. It is called dark matter [4]. Both the development of the Universe and a possible candidate for a dark matter particle will be discussed in this work.

This thesis is structured as follows: It starts with a brief introduction to the phases of the early Universe and the standard model of particle physics in chapter 2. Then the theory of strong interaction will be discussed in more detail in chapter 3. After a discussion of the main ingredients of the theory of strong interactions, Quantum Chromodynamics (QCD) in section 3.1, the main focus of this chapter lies on the techniques used in lattice QCD calculations. These are presented in section 3.2. In this section I describe the techniques that are later used for computations in this work. Starting from the gauge action, I discuss staggered fermions which were used for most computations in this thesis. In addition I introduce overlap fermions, as the overlap operator was used for some calculations in chapter 5. After establishing the lattice formulation I briefly explain the main simulation techniques to make lattice simulations computationally feasible in section 3.2.3. Afterwards I focus on lattice QCD at finite temperature and density, giving a summary of the field. Then I describe the current status of investigations of the QCD phase diagram, focusing on the hadronic phase and the quark gluon plasma. In some energy ranges QCD is accessible perturbatively. An important technique for high energy perturbative QCD, the hard thermal loop expansion, is presented in section 3.4. Finally I discuss the strong CP problem of QCD that could could give insight to some beyond standard model physics.

In the next two chapters I concentrate on computations I was working on. In chapter 4 I focus on computations at finite density QCD. These are especially relevant to understand the physics in heavy ion collisions. Section 4.1 describes the efforts made to meet the conditions in those experiments. The next section gives an overview over the configurations that were used. There are two main analysises from those configurations. First the computation of the cross over temperature in section 4.3 and second the computation of the equation of state in section 4.4 both at non zero baryon chemical potential. The two analysises are described in detail.

In chapter 5 I discuss some aspects of the search for axions. In section 5.1 I describe the computation of the topological susceptibility that is necessary to estimate the mass of axions but is very difficult to compute on the lattice. In section 5.2 I present some properties of a possible experiment that could be used to detect axions. This computations have not been published previously. The thesis closes with a conclusion.

The results obtained in the course of this thesis have been published in [5, 6, 7, 8]. Since the work for this papers was done in a large working group that is necessary to handle all the different aspects of the computations I will give a short overview of my contribution to this results. All calculations were done at least by two people independently.

Tuning to the strangeness neutral point: I made the calculations necessary to tune a simulation to the strangeness neutral point and wrote a program that extrapolates the data to the strangeness neutral point, to reduce the numerical error.

Calculating T_c: I performed the analysis for the crossover temperature on all the used observables. It includes the renormalization of $\bar{\psi}\psi$ and $\chi_{\bar{\psi}\psi}$, fits in several directions and the extrapolation of T_c to finite μ_B with an estimate of both statistical and systematic errors.

Extrapolating data at high temperatures: I wrote a program that extrapolates the data for $\frac{1}{\hat{\mu}_B}\frac{\mathrm{d}\hat{P}}{\mathrm{d}\hat{\mu}_B}$ from zero to imaginary chemical potential at high temperatures as described in section 4.4.1.

The equation of state: I performed the analysis for the equation of state at finite chemical potential. It includes various fits, the determination of the Taylor coefficients of the pressure, the matching of the isentropic trajectories to the beam energies of RHIC and an estimate of both statical and systematic errors.

HRG results: I wrote a program that calculates the pressure for an ideal HRG model and tested the influence of different particles to the result.

Generating configurations: I generated some of the configurations at imaginary chemical potential, using our simulation code *Janos*, on the Blue Gene/Q at the Forschungszentrum Jülich.

Topological susceptibility: I performed the eigenvalue reweighing described in section 5.1.1 and tested for the influence of a different definition for the included number of zero modes. I also performed a continuum extrapolation for χ and b form 3+1-flavour simulations, investigating different fit choices to estimate the systematic error.

Dielectric mirror: I performed the computations necessary to generalize the matrix formalism for classical electrodynamics to a theory with coupling between photons and axions. I wrote a program that computes different properties of a dielectric mirror both for classical electrodynamics and with the new theory for axions.

2 Theory

In this section there will be given a brief overview over the topics covered in this thesis and put them into the context of the general framework of high energy physics. Values given through-out this thesis are usually in units of energy. This is possible in a system of units where $c = \hbar = 1$, with c the speed of light and $\hbar$ the Planck constant divided by 2π, is used. As a unit of energy we use electron Volt (eV). In SI units 1 eV = 1.602 $\frac{\mathrm{kg \cdot m^2}}{\mathrm{s^2}}$. Also μeV = 10^{-6} eV, keV = 10^3 eV, MeV = 10^6 eV and GeV = 10^9 eV are used.

2.1 The early Universe

The Standard Model of Cosmology describes the different eras of the Universe. An overview can be seen in figure 2.1. In this section the early phases will be discussed. These are the phases most interesting for particle physics at the moment. This discussion follows [4].

Experimental determination yields a positive Hubble parameter. This means that we live in an expanding Universe. Also, if one extrapolates back in time, it implies that the Universe was denser and hotter in the past. The hot big bang theory describes a Universe that was very hot and very dense at early stages and can be investigated by means of thermodynamics. It is assumed that the Universe was nearly all the time in thermal equilibrium.

During the recombination era, at temperatures of approximately 0.3 eV the nuclei and electrons that were free at higher temperatures combined to atoms. This made the Universe transparent for photons. Also the cosmic microwave background was formed during this epoch. The cosmic microwave background contains information about the Universe up to temperatures of approximately 0.26 eV and it is and has been under investigation by different experiments for example COBE, WMAP and Planck [10].

Before the recombination the nuclei had to be formed as a combination of neutrons and protons. There are several mechanism how nuclei are created in the Universe. Heavier nuclei are formed during stellar evolution in thermonuclear reactions within the stars or in supernova explosions. Light nuclei were already produced in the early Universe at temperatures between 1 MeV and 50 keV. This timespan is called the era of nucleosynthesis. At that time the Universe was only between 1 and 300 seconds old. Consequently earlier phases of the Universe latest for very brief times compared to everyday time scales.

While decoupling of photons happened in the era of recombination, neutrinos became free at an earlier point, at temperatures of 2 to 3 MeV. This makes them an interesting subject for cosmological observations. Directly observing the neutrino background would allow for observations at higher temperatures than the temperatures reachable by photon observation. Several experiments try to observe neutrinos, investigating the early Universe as well as younger sources of neutrinos like for example supernovae. However due to their weakly

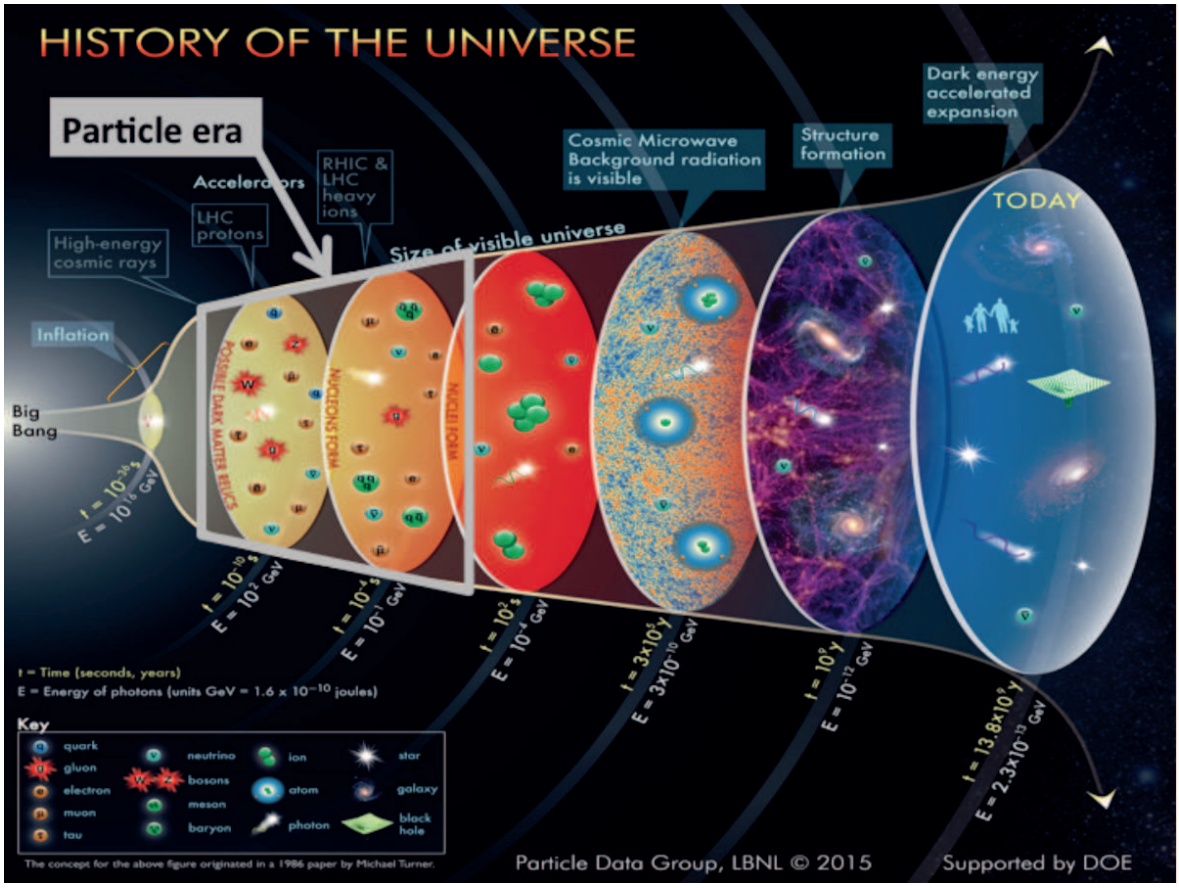

Figure 2.1: *An overview of the phases of the Universe. [9]*

interacting nature neutrinos are extremely hard to detect and a direct observation of the neutrino background is not possible with today's technology.

At even higher temperatures the time of cosmological transitions took place. They can be studied by lattice calculations. There were several transitions in this epoch. While frequently being called phase transitions they were in fact analytic crossovers. In the latest of these transitions at approximately 160 MeV [11, 12, 13] the quark gluon plasma, consisting of quarks and gluons goes over to hadronic states. A more detailed description of this transition and about its investigation can be found in section 3.3. During the same time also the chiral symmetry breaking takes place.

Going to even higher temperatures, the next transition is the electroweak cross over [14]. It takes place at a time approximately 10^{-12} s to 10^{-11} s after the big bang at a temperature of $\mathcal{O}(100)$ GeV [15]. At higher temperatures the elementary particles were massless [3]. The spontaneous symmetry breaking in the electroweak theory yields a transition between the symmetric or high temperature phase and the Higgs phase or broken phase. However this transition is not responsible for the majority of mass that is experienced in daily live. Nearly all of this mass is due to the energy of strong interaction within the hadrons [16]. The mass of elementary particles like the W- and Z-boson is generated due to the Higgs mechanism.

At temperatures of about 10^{16} GeV there might have been the so called Grand Unification transition prior to which the strong, weak and electromagnetic force can not be distinguished any longer. It is not clear if the early Universe ever had such a high temperature especially in models that include inflation. Therefore it might never have happened and remains a theoretical model. [4]

Up to here the particle content of the early Universe can be described within the Standard Model of particle physics (see section 2.2). However within this framework some questions can not be answered. For example the excess of baryons over anti-baryons in the Universe. If matter is created form energy, as it is done in collision experiments and presumably also happened during the big bang, matter and anti-matter is created in equal parts. Since the electroweak transition has been found to be a crossover there is no mechanism where the baryon number non-conversation is strong enough to fully explain the baryon asymmetry. Also the configuration of matter that can be measured today would require quite complicated initial conditions. Another problem is, that in the hot phase of the Universe there were density fluctuations that can be seen in the cosmic microwave background, but can not be explained within the Standard Model. [4]

This problems can be solved by the introduction of an inflationary period. This is a period of rapid expansion prior to the epoch of cosmological phase transitions. It can be described by adding new fields to the Standard Model or extra terms in the action of gravity. The rapid expansion leads to a magnification of small fluctuations, for example vacuum fluctuations, that leads to the density fluctuations in the normal matter which can be observed today.

2.2 The Standard Model of particle physics

The Standard Model of particle physics is the theory that describes with great success our current knowledge of the elementary particles in the Universe. It contains the strong and electroweak interaction, but does not include gravity, which is described by general relativity. It contains 17 particles and their corresponding anti particles. Twelve particles are fermions and five are bosons. The fermions can be divided in two groups. Each group contains three so called families and each family contains again two particles. An overview over the particles is given in figure 2.2.

One of the groups contains the quarks, which make up the elementary building blocks of nuclei and therefore of atoms. The lightest family contains the up and the down quark which are the valence quarks of protons and neutrons. The heavier families contain the charm and the strange quark and the top and the bottom quark. While they are not contained as valence quarks in everyday matter, they become important at high temperature and density, as for example in the early Universe or in particle colliders. Every quark carries a so called colour charge as well as a fractional electric charge. Below the crossover temperature of approximately 150 MeV quarks only exist in bound states, which are called hadrons. Every bound state has an integer electric charge and is colour neutral. The fact that quarks only exist in bound states is called confinement.

The other group contains the leptons. Similar to the quarks the leptons can be divided into three families. Each family contains one charged particle: Either electron, muon, or tau and

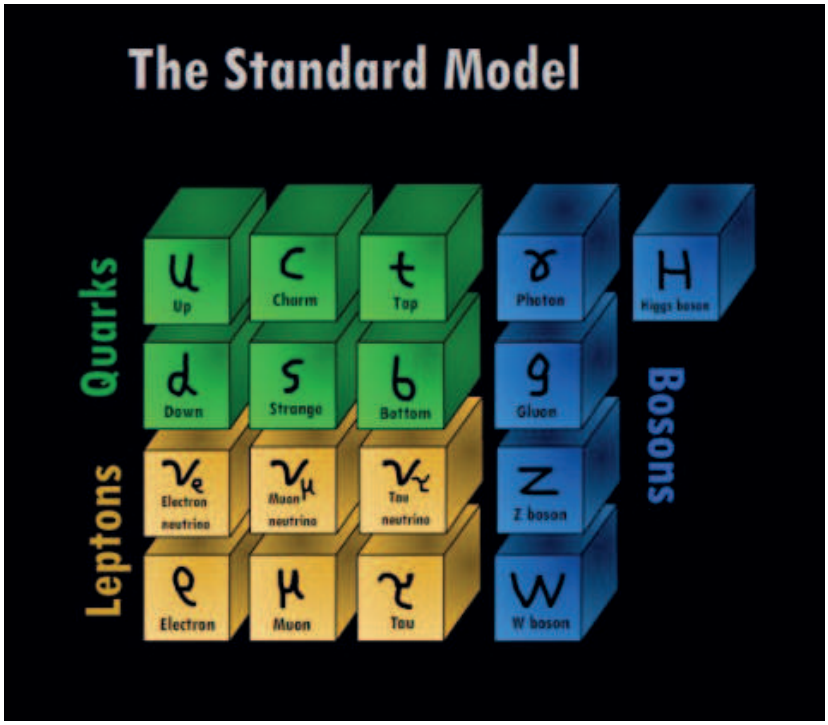

Figure 2.2: *An overview over the elementary particles in the standard model taken from [17]. In the quark and lepton section the particles placed in the same column belong to the same family.*

their corresponding neutral partner which is called a neutrino. Neutrinos are extremely light particles that where thought to be massless in previous versions of the standard model. The fact that neutrinos actually have a mass was shown experimentally by the Sudbury Neutrino Observatory [18] and Super-Kamiokande [19], which measured neutrino oscillation. Neutrions only interact very weakly with matter which makes them hard to detect and to measure. As with the quarks only the first family contributes to our "normal" matter. The muon and the tau are mainly relevant for astronomical observations and collision experiments.

The remaining five particles are the so called bosons. Four of these five are the so called gauge bosons that carry the forces between the particles. The standard model describes three of the four known forces: the strong interaction, the electromagnetic interaction and the weak interaction. It does not include gravity. The exchange particles of the weak force are the massive Z- and W-bosons. This interaction is the weakest of the three forces in the standard model, even though it is stronger than gravity. The electromagnetic interaction acts on electrically charged particles: the quarks, electron, muon, tau and the W-bosons. Its exchange particle is the massless photon. Since the photons are not charged they do not interact with each other directly. The last interaction, the so called *strong interaction*, acts on particles with a colour charge. These are the quarks and the gluons, which are the carriers of the strong force. Since the gluons themselves carry the colour charge the gluons have self interaction. While the coupling of the strong interaction is large at low energies, which prevents a proper perturbative treatment of QCD in that regime, the coupling reduces with increasing energy. This concept is called asymptotic freedom.

The last particle is the Higgs boson. Even though it was predicted a long time ago in 1964 [20, 21, 22, 23, 24], it was discovered only in 2012 [25, 26] at the Large Hadron Collider (LHC). While nearly all the mass we encounter in our daily life is a result of the spontaneous chiral symmetry breaking, the mass of the elementary particles themselves is produced via spontaneous symmetry breaking in the so called Higgs mechanism that is described, for example in [27, 28]. In this mechanism the Higgs particle is created. Its detection at the LHC completed the standard model.

3 Strong interactions

A main topic of this thesis is the investigation of the transition between the quark gluon plasma and the hadronic phase. Since the participants in this transition, the quarks and gluons, are colour charged particles they are subjected to the strong interaction. Therefore we will discuss in this chapter some aspects of the theory of strong interaction. We will briefly introduce the Lagrangian of the theory. In this thesis the tool of choice for investigating the deconfinement transition is lattice QCD. Therefore it will be also be discussed in this section. Another important topic in this thesis is idea of an axion as a dark matter candidate. Its introduction is strongly related to the vacuum structure of QCD and the strong CP-problem that will also be discussed in this chapter.

3.1 Quantum Chromodynamics

Quantum Chromodynamics (QCD) is the widely accepted theory of strong interactions. In this section there will be given a very brief introduction in the most basic principles of QCD. More extensive textbooks on the subject are for example [29, 30], on which this discussion is based.

The Lagrangian of QCD is given as:

$$\mathcal{L} = -\frac{1}{4} F^a_{\mu\nu} F^{a\mu\nu} + \sum_{k=1}^{N_f} \bar{\psi}^k \left(i\gamma^\mu D_\mu - m_k \right) \psi^k \tag{3.1}$$

where k is summed over all flavours, a is summed over the $SU(3)$ degrees of freedom $a = 1, 2, \ldots 8$, and

$$F^a_{\mu\nu} = \partial_\mu A^a_\nu - \partial_\nu A^a_\mu + g f^{abc} A^b_\mu A^c_\nu \tag{3.2}$$

$$D_\mu = \partial_\mu - \mathrm{i} g T^a A^a_\mu. \tag{3.3}$$

Here f^{abc} are the $SU(3)$ structure constants and T^a the eight $SU(3)$ generators. Therefore the indices a, b and c run from one to eight [30]. The A^a_μ are the gauge fields. They are elements of $\mathfrak{su}(3)$, the Lie algebra of $SU(3)$. As colour octets they transform under the adjoint representation of the Lie group $SU(3)$. The ψ represent the quark fields. As colour triplets they transform under the fundamental representation of $SU(3)$. Since the quarks are fermions (they have a spin of $\frac{1}{2}$) they transform as spinors in the Dirac space and are denoted by Grassmann variables in the path integral formalism, meaning that

$$\{\psi_i, \psi_j\} = 0 \tag{3.4}$$

The Lagrangian is gauge invariant. This means it does not change under a local gauge transformation where [31]

$$\psi(x) \longrightarrow e^{\mathrm{i}\alpha^a(x)T^a}\psi(x) \tag{3.5}$$

$$A^a_\mu(x) \longrightarrow e^{f^{abc}\alpha^b(x)}A^c_\mu(x). \tag{3.6}$$

In principle there could be an extra term in the Lagrangian of the form

$$\mathcal{L}_{CP} = \frac{g^2}{32\pi^2}\bar{\theta}F^{a\mu\nu}\tilde{F}^a_{\mu\nu} \tag{3.7}$$

where $\bar{\theta}$ is the so called vacuum angle and $\tilde{F}_{\mu\nu}$ is the dual field strength tensor given as $\tilde{F}_{\mu\nu} = \frac{1}{2}\epsilon_{\mu\nu\sigma\lambda}F^{\sigma\lambda}$. As described in section 3.5, $\bar{\theta}$ is constrained by the measurement of the neutron electric dipole moment to $|\theta| < 10^{-9}$ [32]. Therefore this term vanishes in the standard model [33].

Unlike the electric charge the colour charge of quarks cannot be observed directly in experiments. However there are convincing arguments for the existence of the colour charge. First it ensures confinement. If all hadrons transform as singlets under colour transformation, it explains why no free particles with fractional electric charges are observed. Another motivation comes from the Δ^{++} particle. It is interpreted as a state with three u valence quarks. Its wave function would be completely symmetric under the exchange of spin or flavour quantum numbers. At the same time the quarks are fermions and have to obey the Fermi-Dirac statistics (or Pauli principle). This contradiction is solved if the three quarks do not have the same quantum numbers, due to the different colour charges.

An indirect measurement of the colour charge can be done using the process of Bhabha scattering, where two electrons (e^+e^-) annihilate. The produced virtual photon creates pairs of charged particles with a probability proportional to the crossections of the final states. The crossection for this process can be analysed and split by whether there are hadrons or muons ($\mu^+\mu^-$) in the final state. Each color state is produced with equal probability, thus the ratio of the two crossections

$$R = \frac{\sigma_{e^+e^-\longrightarrow\text{hadrons}}}{\sigma_{e^+e^-\longrightarrow\mu^+\mu^-}} \tag{3.8}$$

is proportional to the number of different colour charges N_c. R is a factor of three larger than one would expect without consideration of the colour charge. Therefore $N_c = 3$.

In addition to the local gauge symmetry of the Lagrangian, $\mathcal{L}$ is invariant or nearly invariant under several global transformations of the quark fields. In the case of N_f fermion flavours with equal mass $\mathcal{L}$ is invariant under a transformation

$$\psi \longrightarrow \psi' = e^{\mathrm{i}\Gamma^a\alpha_a}\psi, \tag{3.9}$$

where Γ^a are the generators of either $U(1)$ or $SU(N_f)$. The corresponding conserved Nöther current is defined as

$$J^a_\mu = -\frac{\partial \mathcal{L}}{\partial(\partial^\mu \psi)} \frac{\partial \psi'}{\partial \alpha_a} \tag{3.10}$$

$$= \bar{\psi} \gamma_\mu \Gamma^a \psi. \tag{3.11}$$

From the zeroth component one can then defined the corresponding charge Q_a as

$$Q_a = \int \mathrm{d}^3x \; J^0_a(x) \tag{3.12}$$

$$= \int \mathrm{d}^3x \; \psi^\dagger(x) \Gamma_a \psi(x). \tag{3.13}$$

Q_a is constant in time implying that

$$\frac{\mathrm{d}Q_a}{\mathrm{d}t} = 0. \tag{3.14}$$

There are several choices for $\Gamma^a \alpha_a$. If the Γ^a are taken to be the generators of $U(1)$ (just meaning that $\Gamma_a = 1$) this leads to the transformation of

$$\psi \longrightarrow e^{\mathrm{i}\alpha} \psi \tag{3.15}$$

and to the charge

$$Q = \int \mathrm{d}^3x \; \psi^\dagger(x) \psi(x). \tag{3.16}$$

This is the definition of the baryon number. Therefore the baryon number is conserved under the strong interaction.

For $N_f = 2$ and equal masses $m_u = m_d = m_{ud}$ the Lagrangian is invariant under a transformation of $SU(2)$ where the generators are

$$\Gamma_a = \frac{\tau_a}{2} \tag{3.17}$$

with the three Pauli matrices τ_a. This corresponds to the conservation of the isospin in QCD and is called isospin symmetry. Although in reality [34]

$$m_u \approx \frac{m_d}{2} \tag{3.18}$$

these masses are sufficiently small in comparison to the scale of the spontaneous breaking of the chiral symmetry. Therefore in QCD thermodynamic calculations with degenerate u and d quarks are common. They are precise enough to allow for percent level accuracy in the final results.

In the case of $N_f = 3$ and equal masses $m_u = m_d = m_s$ the Lagrangian is invariant under a $SU(3)$ transformation with the generators

$$\Gamma_a = \frac{\lambda_a}{2} \tag{3.19}$$

where λ_a are the eight Gell-Mann matrices. This leads to the conserved current

$$J_a^\mu = \bar{\psi}\gamma^\mu \frac{\lambda_a}{2}\psi. \tag{3.20}$$

However in nature the mass of the strange quark is larger than the mass of the u or d quark. Therefore the derivative of the current does not vanish exactly but

$$J_a^\mu \propto (m_s - m_{ud}). \tag{3.21}$$

Another not exactly realized symmetry is the so called chiral symmetry. Classically it exists in the limit of massless quarks and describes the invariance to opposite rotations of ψ_R and ψ_L in flavour space where

$$\psi_R = \frac{1}{2}\left(1+\gamma_5\right)\psi \tag{3.22}$$

$$\psi_L = \frac{1}{2}\left(1-\gamma_5\right)\psi \tag{3.23}$$

and $\gamma_5 = \mathrm{i}\gamma^0\gamma^1\gamma^2\gamma^3$. The Lagrangian of massless QCD can be written as

$$\mathcal{L}_{\chi QCD} = -\frac{1}{2}F_{\mu\nu}F^{\mu\nu} + \sum_{k=1}^{N_f}\bar{\psi}_R^k\left(i\gamma^\mu D_\mu\right)\psi_R^k + \sum_{k=1}^{N_f}\bar{\psi}_L^k\left(i\gamma^\mu D_\mu\right)\psi_L^k \tag{3.24}$$

However the mass term breaks the chiral symmetry explicitly and mixes left and right handed quarks. Since the masses of up and down quarks are very small, massless QCD can be the starting point for a systematic approximation to $N_f = 2$-QCD. This gives rise to the field of chiral perturbation theory that also has a strong influence on lattice QCD.

3.2 Lattice QCD

Since the theory of the strong interaction, Quantum Chromodynamics (QCD), can not be treated perturbatively in every parameter region, a common way of solving QCD is the use of lattice QCD (LQCD). The concept of lattice QCD can be understood in the path integral formalism. As a first step one Wick rotates the path integral

$$\langle\mathcal{O}\rangle = \frac{1}{Z}\int \mathcal{D}[U]\mathcal{D}\bar{\psi}\mathcal{D}\psi\mathcal{O}e^{-\mathrm{i}S_{\mathrm{Minkowski}}}, \tag{3.25}$$

thus replacing the Minkowski time τ with the Euklidean time it. This results in the Euclidean path integral

$$\langle\mathcal{O}\rangle = \frac{1}{Z}\int \mathcal{D}[U]\mathcal{D}\bar{\psi}\mathcal{D}\psi\mathcal{O}e^{-S_F-S_G}. \tag{3.26}$$

Here U are the gauge links, and $\bar{\psi}$ and ψ denote the fermion fields. The $\mathcal{D}$ symbol denotes the integrals over the field at every point in space time. For example

$$\mathcal{D}\psi = \prod_x \mathrm{d}\psi(x). \tag{3.27}$$

So every integral in equation (3.26) actually denotes infinitely many integrals. LQCD replaces the continuous space time by a discrete four dimensional lattice, thus allowing to solve the path integral with a finite number of integrals. The discrete lattice points serve as ultraviolet regulator while the finite extent of the lattice supplies an infrared cut-off.

The integral over the Grassmann fields ψ and $\bar{\psi}$ can be solved analytical yielding

$$\langle \mathcal{O} \rangle = \frac{1}{Z} \int \mathcal{D}[U] \mathcal{O} \det[M] e^{-S_G} \tag{3.28}$$

where M is the fermion matrix given as

$$\int \mathcal{D}\bar{\psi}\mathcal{D}\psi e^{-S_F} = \det M. \tag{3.29}$$

$\det[M]e^{-S_G}$ can be interpreted as Boltzmann weight for $\det M \geq 0$, thus allowing importance sampling for solving the integral.

In this section some of the techniques that made it possible to determine the results of this thesis will be presented. A more detailed and complete introduction to LQCD can be found for example in [27, 35, 36, 37].

3.2.1 Gauge actions

Here the relation of the lattice action with the continuum action is derived. The derivation follows [27] and [38]. Also some improvement program will be discussed. The standard unimproved gauge action on the lattice is the Wilson action, which is given as

$$S[U] = \frac{\beta}{3} \sum_x \sum_{\mu<\nu} \Re \operatorname{tr} \left(\mathbb{1} - U_{x,\mu\nu} \right) \tag{3.30}$$

with the gauge fields $U \in SU(3)$ and the plaquette $U_{x,\mu\nu}$ that is depicted in figure 3.2.

The link variables U are the so called gauge fields that build the links of the lattice. They are related to the continuum fields A_μ via the formula

$$U_{x\mu} = e^{\mathrm{i}gA_{x\mu}}. \tag{3.31}$$

Since the $A_{x\mu}$ are in the $SU(3)$ algebra, $\mathfrak{su}(3)$, this yields that $U \in SU(3)$. From figure 3.1 the relation

$$U^\dagger_{x-\hat{\mu},\mu} = U_{x,-\mu} \tag{3.32}$$

becomes apparent.

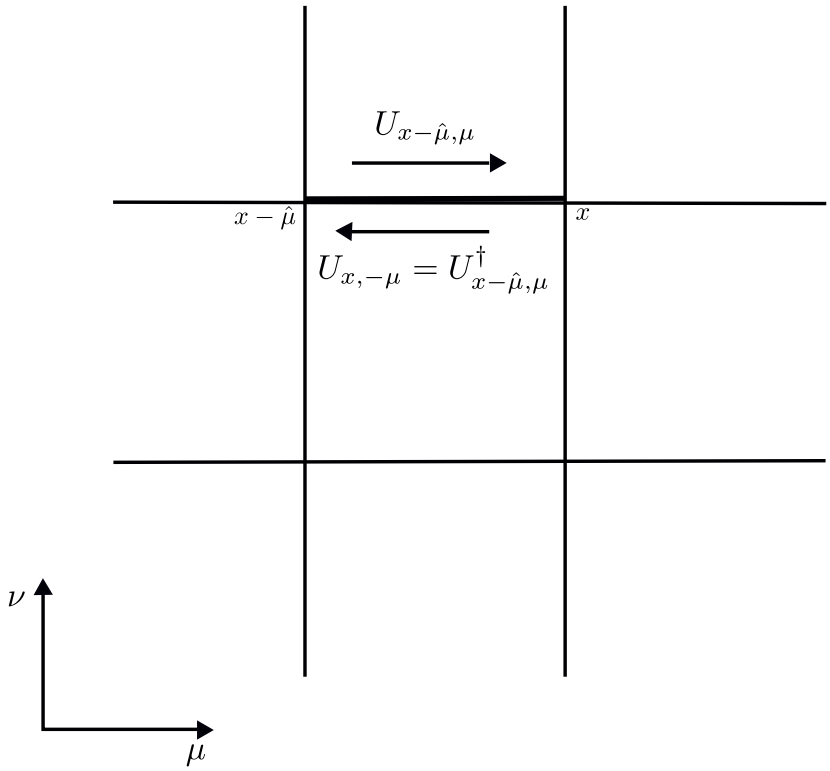

Figure 3.1: *The interchanging of the orientation of a link variable.*

In the continuum the Lagrangian of the pure gauge theory includes the square of the field strength tensor $F_{\mu\nu}$, which is given as

$$F_{\mu\nu} = \partial_\mu A_\nu - \partial_\nu A_\mu - \mathrm{i}g[A_\mu, A_\nu]. \tag{3.33}$$

The field strength tensor describes the infinitesimal change of the fields per area, if they are transported in an infinitesimal circle. Due to the discrete nature of the lattice there cannot be an object like an infinitesimal circle. Instead one uses a plaquette, which is the smallest square on the lattice. A graphic representation of this plaquette can be found in figure 3.2. The plaquette is calculated as the product of the four link variables in the direction of the arrow. If necessary the orientation of the gauge fields can be changed by the use of equation 3.32. This gives the formula

$$U_{x,\mu\nu} = U_{x\mu} U_{x+\hat{\mu},\nu} U^{\dagger}_{x+\hat{\nu},\mu} U^{\dagger}_{x\nu}. \tag{3.34}$$

To relate this with the continuum action one can Taylor expand this expression to recover the field strength tensor in equation (3.33). Since the gauge fields do not commute with each other on has to make use of the Baker-Cambell-Hausdorff-formula

$$e^A e^B = e^{A+b+\frac{1}{2}[A,B]+\cdots} \tag{3.35}$$

during this expansion.

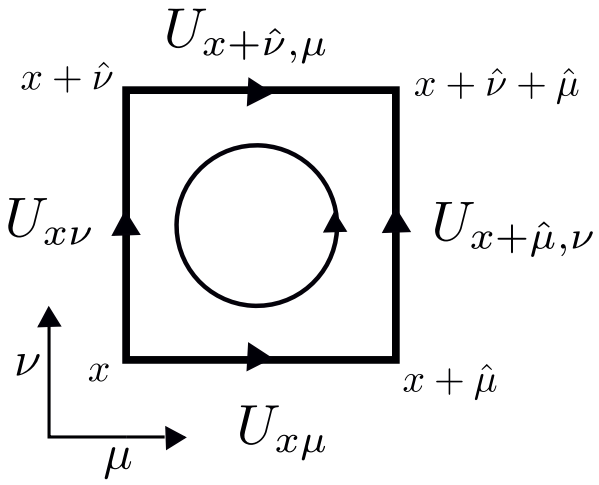

Figure 3.2: *Schematic of a plaquette.*

If one replaces the link variables in the plaquette with the the continuum fields as given in (3.31) this yields

$$U_{x,\mu\nu} = e^{\mathrm{i}gaA_{x\mu}} e^{\mathrm{i}gaA_{x+\hat{\mu},\nu}} e^{-\mathrm{i}gaA_{x+\hat{\nu},\mu}} e^{-\mathrm{i}gaA_{x\nu}}. \tag{3.36}$$

After applying the Baker-Cambell-Hausdorff-formula (equation (3.35))

$$U_{x,\mu\nu} = e^{\mathrm{i}gaA_{x\mu}+\mathrm{i}gaA_{x+\hat{\mu},\nu}-\frac{a^2g^2}{2}[A_{x\mu},A_{x+\hat{\mu},\nu}]+\mathcal{O}(a^3)} e^{-\mathrm{i}gaA_{x+\hat{\nu},\mu}-\mathrm{i}gaA_{x\nu}-\frac{a^2g^2}{2}[A_{x+\hat{\nu},\mu},A_{x\nu}]+\mathcal{O}(a^3)}.$$

Applying the formula a second time, yields

$$\begin{aligned} U_{x,\mu\nu} = \exp\big(&\mathrm{i}gaA_{x\mu} + \mathrm{i}gaA_{x+\hat{\mu},\nu} - \mathrm{i}gaA_{x+\hat{\nu},\mu} - \mathrm{i}gaA_{x\nu} \\ &+\frac{a^2g^2}{2}\left(-[A_{x+\hat{\nu},\mu},A_{x\nu}] - [A_{x\mu},A_{x+\hat{\mu},\nu}] + [A_{x\mu},A_{x+\hat{\nu},\mu}]\right. \\ &\left.+[A_{x\mu},A_{x\nu}] + [A_{x+\hat{\mu},\nu},A_{x+\hat{\nu},\mu}] + [A_{x+\hat{\mu},\nu},A_{x\nu}]) + \mathcal{O}(a^3)\right). \end{aligned} \tag{3.37}$$

The A fields themselves can now be expanded in a as

$$A_{x+\hat{\mu},\nu} = A_{x\nu} + a\partial_\mu A_{x\nu} + \mathcal{O}(a^2). \tag{3.38}$$

This results in the expression

$$U_{x,\mu\nu} = e^{\mathrm{i}a^2g(\partial_\mu A_{x\nu}-\partial_\nu A_{x\mu}+ig[A_{x\mu},A_{x\nu}])+\mathcal{O}(a^3)} \tag{3.39}$$

$$= e^{\mathrm{i}a^2gF_{\mu\nu}} \tag{3.40}$$

for the plaquette. Another expansion in a^2 yields

$$U_{x,\mu\nu} = \mathbb{1} + ia^2gF_{\mu\nu} - \frac{a^4g^2}{2}\left(F_{\mu\nu}\right)^2 + \mathcal{O}(a^6) \tag{3.41}$$

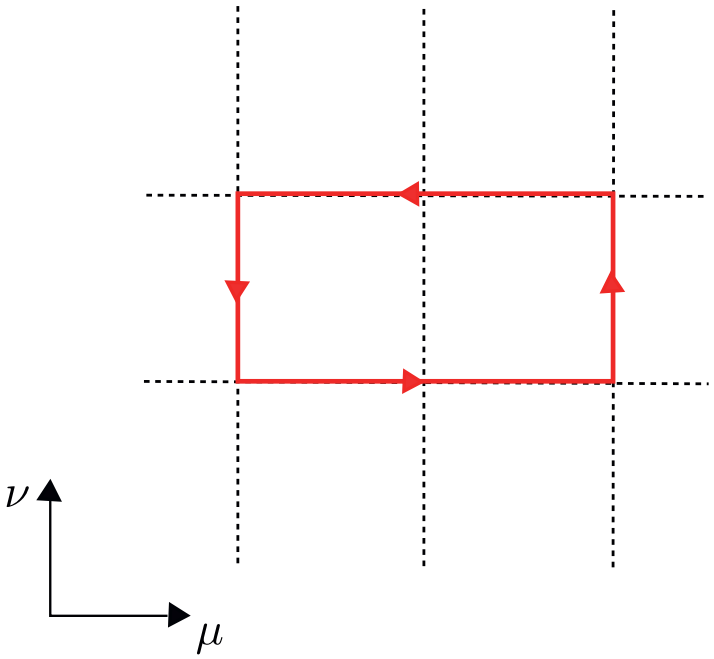

Figure 3.3: *A Wilson loop of size* 2×1.

This Successfully relates the Wilson gauge action

$$S[U] = \frac{\beta}{N} \sum_x \sum_{\mu<\nu} \Re \operatorname{tr} (\mathbb{1} - U_{x,\mu\nu}) \tag{3.42}$$

$$= \frac{\beta}{N} \sum_{pl} \Re \operatorname{tr} (\mathbb{1} - U_{pl}) \tag{3.43}$$

with the continuum action

$$S[A] = \int \mathrm{d}^4 x \frac{1}{4} \operatorname{tr} F_{\mu\nu} F^{\mu\nu}. \tag{3.44}$$

for

$$\beta = \frac{6}{g^2}. \tag{3.45}$$

Of course the discretization of the action is not unique. It is possible to add other terms that do not change the continuum limit. This allows to add terms that cancel contributions of low order in a thus improving on the convergence towards the continuum. Simulations on large lattice that are required to achieve a continuum limit are computationally very expensive. Therefore it is usually worth heaving extra effort in computing the action in exchange for an improved continuum behaviour. For the simulations contributing to this work a Symanzik improved gauge action was used [39, 40, 41]. For the Symanzik gauge action S_{Symanzik} one does not only use the plaquette, but also 2×1 rectangles $R_{\mu\nu}$ as shown in figure 3.3. Such a closed loop is called a *Wilson loop*. The improved action can then be written as [42]

$$S_{\text{Symanzik}} = \beta \sum_x \sum_{\mu<\nu} \left(c_0 \left(1 - \frac{1}{3} \Re(U_{\mu\nu}) \right) + c_1 \left(1 - \frac{1}{3} \Re(R_{\mu\nu}) \right) \right). \tag{3.46}$$

The optimal choice for c_0 and c_1 has to be computed. This can be done by lattice perturbation theory. At tree level this yields

$$c_0 = \frac{5}{3} \tag{3.47}$$

$$c_1 = -\frac{1}{12} \tag{3.48}$$

resulting in an action that is of order $\mathcal{O}(\alpha_s a^2)$ [42].

3.2.2 Fermions

Apart from the gauge fields which are the links on the lattice also the fermions have to be discretized. The fermions are denoted by the Grassmann fields ψ and $\bar{\psi}$ and are located on the lattice sites. This sections starts from the naive discretization and then introduces the two formulations that were used in the simulations for this thesis.

3.2.2.1 Naive discretization

The action of a free fermion

$$S_F[\psi, \overline{\psi}] = \int \mathrm{d}^4 x \overline{\psi}(x) \left(\gamma_\mu \partial_\mu + m\right) \psi(x). \tag{3.49}$$

can be discretized on a lattice by replacing the derivative by the central differential quotient as

$$S_F[\psi, \overline{\psi}] = a^4 \sum_{n \in \Lambda} \overline{\psi}(n) \left(\sum_{\mu=1}^{4} \gamma_\mu \frac{\psi(n+\mu) - \psi(n-\mu)}{2a} + m\psi(n) \right). \tag{3.50}$$

However if one wants to couple the gauge fields with the fermions one has to take into account that the action should be invariant under rotation in colour space. Therefore the action is not allowed to change under a transformation

$$\psi(n) \to \psi'(n) = \Omega(n)\psi(n) \tag{3.51}$$

$$\overline{\psi}(n) \to \overline{\psi'}(n) = \overline{\psi}(n)\Omega(n)^\dagger \tag{3.52}$$

where $\Omega \in SU(3)$. For this to hold one has to add the discretized covariant derivatives so that the action reads

$$S_F[\psi, \overline{\psi}, U] = a^4 \sum_{n \in \Lambda} \overline{\psi}(n) \left(\sum_{\mu=1}^{4} \gamma_\mu \frac{U_\mu(n)\psi(n+\mu) - U_{-\mu}(n)\psi(n-\mu)}{2a} + m\psi(n) \right). \tag{3.53}$$

By Taylor expansion of the gauge fields, similar to the calculations in section 3.2.1, this can be related to the continuum action

$$S_F[\psi, \overline{\psi}, A] = \int \mathrm{d}^4 x \overline{\psi}^{(f)}(x) \left(\gamma_\mu(\partial_\mu + iA_\mu(x)) + m^{(f)}\right) \psi^{(f)}(x). \tag{3.54}$$

Note that it is possible to rewrite this action as

$$\begin{aligned} S_F[\psi,\overline{\psi},U] = a^4 \sum_{n\in\Lambda} \overline{\psi}(n) \sum_{\mu=1}^{4} \gamma_\mu \frac{U_\mu(n)\psi(n+\mu)}{2a} \\ - a^4 \sum_{n\in\Lambda} \overline{\psi}(n) \sum_{\mu=1}^{4} \gamma_\mu \frac{U_{-\mu}(n)\psi(n-\mu)}{2a} \\ + a^4 \sum_{n\in\Lambda} \overline{\psi}(n) m \psi(n) \qquad (3.55) \\ = \overline{\psi} M[U] \psi \qquad (3.56) \end{aligned}$$

for an appropriately chosen fermion matrix M. This allows for the fermionic fields which are Grassmann variables to be integrated out in a way that

$$\int \mathcal{D}\bar{\psi}\mathcal{D}\psi e^{-S_F} = \det M \qquad (3.57)$$

However if the fermion propagator is calculated for this action a problem with this naive discretization becomes obvious. On the lattice the propagator is proportional to a term of the form

$$\frac{1}{\sum_\mu \sin^2(p_\mu a)} \qquad (3.58)$$

while in the continuum the propagator is proportional to

$$\frac{1}{p^2}. \qquad (3.59)$$

The continuum propagator has a pole at $p = (0,0,0,0)$ corresponding to one fermion. On the other hand the lattice propagator has a pole whenever each component of p is equal either to 0 or to $\frac{\pi}{a}$. Since there are 16 possible ways of arranging the components of p fulfilling this condition this corresponds to 16 fermions, of which only one represents the desired continuum fermion while the others are the so called doublers. To get rid of those doublers other fermion discretizations have to be found. Two possible discretizations are described in the following to sections.

For the discussion of fermion discretizations on the lattice the Nielsen-Ninomiya-no-go theorem [43, 44, 45] is important. It states that under some reasonable assumptions it is impossible to discretize fermions on the lattice in a way that removes the doublers and fulfils the chiral symmetry relation

$$D\gamma_5 + \gamma_5 D = 0 \qquad (3.60)$$

at the same time.

3.2.2.2 Staggered-Fermions

The idea of the Staggered-Fermions (or Kogut-Susskind-Fermions) is to construct an action that is diagonal in Spinor space, thus sorting the extra fermions in four groups, that are exact

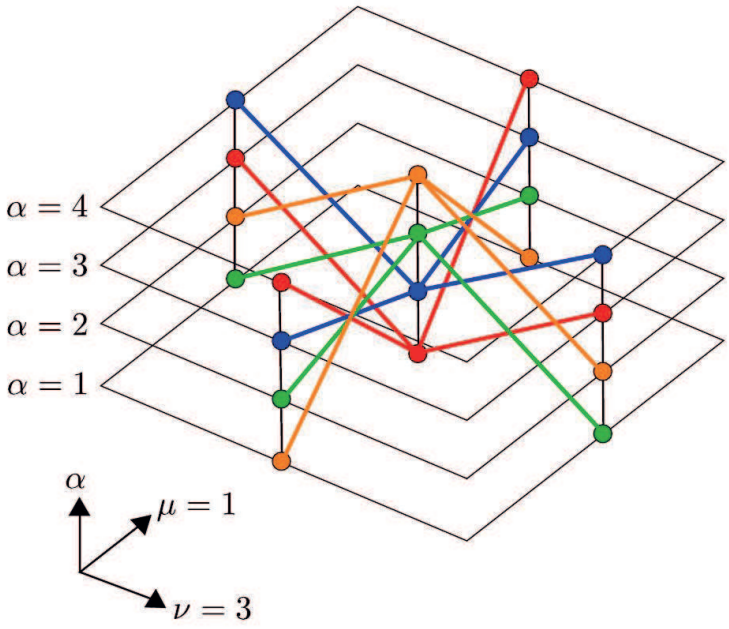

Figure 3.4: *The distribution of a fermion field in the staggered fields on a two dimensional lattice [46]. The coupling to the neighbouring lattice sites comes from the derivative.*

copies of each other. Then the unwanted replica spinors can be droped, leaving instead of fifteen only three doubler fermions. This is possible because at each lattice point a spinor only couples to itself and one spinor component at the next neighbor lattice site. This situation is illustrated in figure 3.4. By transforming the fermion fields with a transformation that mixes spinor and space-time indices it is possible to rearrange the fermion degrees of freedom in a way that the transformed fields, on the corners of a hypercube, can be identified with dirac spinors. This is achieved by replacing the fermion fields in the naive fermion action in equation 3.53 with $\psi'(n)$ as

$$\psi(n) = \gamma_1^{n_1}\gamma_2^{n_2}\gamma_3^{n_3}\gamma_4^{n_4}\psi(n)' \tag{3.61}$$
$$\bar{\psi}(n) = \bar{\psi}(n)'\gamma_4^{n_4}\gamma_3^{n_3}\gamma_2^{n_2}\gamma_1^{n_1}, \tag{3.62}$$

where $n_1 \dots n_4$ are the coordinates of the site n. Since $\gamma_\mu^2 = \mathbb{1}$ it is obvious that the mass term is invariant under this transformation. In the kinematic term there is an imbalance in the number of γ-matrices for ψ and $\bar{\psi}$ since they are not at the same lattice point but at neighboring spots. However this gets exactly compensated by the extra γ-matrix in the action. Because of the anticommutation of γ-matrices the interchanging necessary to achieve the correct order of γ-matrices may result in an extra sign. Therefore the γ_μ in the action has to be replaced by the staggered sign functions

$$\begin{aligned}\eta_1 &= 1\\ \eta_2 &= (-1)^{n_1}\\ \eta_3 &= (-1)^{n_1+n_2}\\ \eta_4 &= (-1)^{n_1+n_2+n_3}.\end{aligned}$$

This results in the action

$$S_F[\psi,\overline{\psi},U] = a^4 \sum_{n\in\Lambda} \overline{\psi}(n)' \left(\sum_{\mu=1}^{4} \eta_\mu(n) \mathbb{1} \frac{U_\mu(n)\psi(n+\mu)' - U_{-\mu}(n)\psi(n-\mu)'}{2a} + m\psi(n)' \right). \tag{3.63}$$

Since there are no more γ-matrices appearing in the action it is diagonal in spinor space. It also has the same form for every spinor index. Therefore the fermion field ψ' can be replaced by an other field χ that has only color but no spinor indices. Keeping only one copy of the spinor structure yields the equation

$$S_F[\chi,\overline{\chi},U] = a^4 \sum_{n\in\Lambda} \overline{\chi}(n)' \left(\sum_{\mu=1}^{4} \eta_\mu(n) \frac{U_\mu(n)\chi(n+\mu)' - U_{-\mu}(n)\chi(n-\mu)'}{2a} + m\chi(n)' \right). \tag{3.64}$$

To interpret the χ fields one can rewrite the action in terms of dirac spinors where a quark field is given as

$$q(n)_{at} = \frac{1}{8} \sum_{s_i=0,1} \left(\gamma_1^{s_1}\gamma_2^{s_2}\gamma_3^{s_3}\gamma_4^{s_4}\right)_{\alpha t} \chi(2n+s), \tag{3.65}$$

if one assumes an even number of lattice sites in all directions. The index t is the so called *taste*. It distinguishes between the four remaining copies of the fermions. The action in terms of the q fields can then be written as

$$S_F[q,\bar{q}] = (2a)^4 \sum_n (m\bar{q}(n)q(n)) + \sum_\mu \mathrm{tr}\left(\bar{q}(n)\gamma_\mu \nabla_\mu q(n)\right) - a\sum_\mu \mathrm{tr}\left(\bar{q}(n)\gamma_5 \triangle_\mu q(n)\gamma_\mu\gamma_5\right). \tag{3.66}$$

The first two terms are the same as in the naive fermion action. However now instead of neighbouring terms there are next-to neighbouring terms in the derivatives. These two terms are diagonal in the taste. The last term mixes the tastes. Therefore it is called the *taste breaking* term.

There are still three fermion doublers one has to deal with. A common practice is the so called *rooting* to remove the extra fermions. This means, that one takes the fourth root of the fermion determinant assuming that the four different fermions are approximately the same and the taste splitting is small. The reduction of the fermion fields by a factor of four makes the staggered fermions computational cheap, thus allowing for simulations that are not feasible with other fermion discretizations. Computations that have been repeated with other fermions did not reveal any problems due to the rooting [47]. Another feature of staggered fermions in comparison to for example Wilson fermions is that a remnant of the chiral symmetry survives the removal of the doubles, resulting in the absence of an additive quark mass renormalisation.

3.2.2.3 Overlap-Fermions

Overlap fermions [48] are the theoretically most elegant fermion discretization used in lattice simulations. They implement exact chiral symmetry on the lattice without the difficulties that

arise with the rooting in staggered fermions. However they are at the same time the computational most expensive choice, which makes their use unfeasible in many computations.

The Ginspark-Wilson relation [49], that is a requirement for chiral symmetry on the lattice, replaces the continuum condition of chiral symmetry

$$D\gamma_5 + \gamma_5 D = 0 \tag{3.67}$$

for the Dirac operator D by

$$D\gamma_5 + \gamma_5 D = aD\gamma_5 D. \tag{3.68}$$

This allows chiral symmetry to be defined on a finite lattice. The overlap operator fulfills the Ginspark-Wilson relation thus realizing chiral symmetry.

The Overlap operator is given as

$$D_{\text{overlap}} = \frac{1}{a}\left(\mathbb{1} + \gamma_5 \operatorname{sgn} H\right) \tag{3.69}$$

with

$$H = \gamma_5 A \tag{3.70}$$

and A a suitable Dirac operator that is projected to chiral symmetry by the overlap operator. The simplest choice for the kernel A is

$$A = aD_W - \mathbb{1}(1+s) \tag{3.71}$$

where D_W is the Wilson Dirac operator and s is a parameter that can be tuned to optimize the locality of the overlap operator. The sgn function in the operator can be either defined via the spectral representation or by writing

$$\operatorname{sgn} H = H\left(H^2\right)^{-\frac{1}{2}}. \tag{3.72}$$

Here the inverse square root is a matrix that is not necessarily sparse, thus introducing entries that relate terms form all over the lattice instead of only nearest neighbor terms. Therefore the overlap operator is not ultralocal. However it still fulfils the relation

$$|D(n|m)_{\alpha\beta,ac}| \leq Ce^{-\gamma||n-m||} \tag{3.73}$$

with constants C and γ that do not depend on the gauge fields. $\frac{1}{\gamma}$ is a fixed length in lattice units and therefore reduces to zero in the continuum limit yielding a local field theory as required.

3.2.3 Monte Carlo Simulations

To evaluate the path integral in lattice QCD Monte Carlo simulations are the usual choice. The expectation value of an observable $\mathcal{O}$ is given as

$$\langle O\rangle = \frac{\int \mathcal{D}[U]\mathcal{O}\det M e^{-S_G}}{\int \mathcal{D}[U]\det M e^{-S_G}} \tag{3.74}$$

Instead of using naive uniformly distributed random numbers to solve the integral (3.74), as that would take way to long, one rewrites the expectation value to

$$\langle \mathcal{O} \rangle = \lim_{N \longrightarrow \infty} \frac{1}{N} \sum_{n=1}^{N} \mathcal{O}, \tag{3.75}$$

with fields that are generated according to the probability distribution

$$\mathrm{d}P(U, \bar{\psi}\psi) = \frac{\mathcal{D}[U] \det M e^{-S_G}}{\int \mathcal{D}[U] \det M e^{-S_G}}. \tag{3.76}$$

This approach is called importance sampling.

The generation of configurations with this probability distribution can be achieved via different algorithms that have to meet certain requirements:

1. The probability $T(U'|U)$ to move from U to U' has to bee larger than zero:

$$T(U'|U) \geq 0 \quad \forall U \tag{3.77}$$

2. The sum of all probabilities $T(U'|U)$ is normalized. This implies

$$\sum_{U'} T(U'|U) = 1 \quad \forall U. \tag{3.78}$$

3. For the probability $P(U')$ for the system to be in a state U' the stability equation

$$P(U') = \sum_{U} T(U'|U) P(U). \tag{3.79}$$

   is fulfilled.

4. For every U and U' it exists a k, so that

$$T^k(U'|U) > 0 \tag{3.80}$$

   is fulfilled. This condition is called ergodicity.

An even stronger form of the third condition is the so called *detailed balance condition*:

$$T(U'|U) P(U) = T(U|U') P(U'). \tag{3.81}$$

This is fulfilled by most common algorithms.

One of the simplest algorithms that fulfills these conditions for lattice QCD is the Metropolis algorithm, that was introduced in 1953 [50]. However it is also rather inefficient and therefore hardly used in lattice simulations. For pure gauge theory, quenched QCD or any model where the action is bosonic and ultralocal the heat bath algorithm is a common choice. For $SU(3)$ gauge theory it was introduced by N. Cabibbo and E. Marinari in 1982 [51].

The most common algorithm for full lattice QCD simulations that is also used for the generation of configurations in this thesis is the Hybrid Monte Carlo (HMC) algorithm. A detailed description of this algorithm can be found in [27]. The idea of the Hybrid Monte Carlo algorithm is to use molecular dynamics to move along hypersurfaces with constant energy in phase space by solving fictitious Hamilton equation of motion

$$\frac{\mathrm{d}P}{\mathrm{d}t} = -\frac{\partial H}{\partial Q} \tag{3.82}$$

$$\frac{\mathrm{d}Q}{\mathrm{d}t} = -\frac{\partial H}{\partial P}. \tag{3.83}$$

However one should note that this is not the Hamilton function of the physical system but an artificial or fictitious Hamilton function which allows for an efficient computation. To solve this equations one needs the momenta π that are generated according to a Gaussian probability distribution. The evolution of this equations is done by Leap Frog algorithm (a description can be found in [27]) along a fictitious Monte Carlo time τ. This procedure allows for large steps in phase space which reduces the autocorrelation time of the simulations. Since the calculation of the hyperplanes is done numerically the energy is not strictly conserved. Therefore the molecular dynamics needs to be combined with an accept reject step as in the Metropolis algorithm. Then the algorithm is exact for any choice of $\tau > 0$. Each update with the Hybrid Monte Carlo Algorithm consist of the following steps:

1. Generation of the momenta π according to a Gaussian probability distribution
2. Determination of the Energy E on the current configuration
3. Using the molecular dynamics with a Monte Carlo time τ to generate a new configuration
4. Deriving the energy E' of the new configuration
5. Accepting the new configuration with the probability

$$p = \min\left(1, e^{E-E'}\right) \tag{3.84}$$

During the the update the fermion determinant $\det M$ has to be evaluated. Due to the large size of the fermion matrix M a direct evaluation is not feasible. Instead one can do a stochastic evaluation of the determinant. One introduces the pseudo fermion fields ξ that are chosen randomly from a probability distribution

$$p \propto e^{-\xi^\dagger \xi}. \tag{3.85}$$

The square of the fermion determinant can then be calculated as

$$\det(MM^\dagger) = \frac{\int \mathcal{D}\xi \mathcal{D}\,\xi^\dagger e^{-\xi^\dagger (MM^\dagger)^{-1}\xi}}{\int \mathcal{D}\xi \mathcal{D}\xi^\dagger\, e^{-\xi^\dagger \xi}}. \tag{3.86}$$

For the HMC algorithm only the application of the fermion matrix to a vector has to be known. The inverse $(MM^\dagger)^{-1}$ applied to a vector can be determined by solving the corresponding system of linear equations for example by applying the conjugate gradient algorithm [52].

The square of the fermion determinant is only relevant for a simulation with an even number of degenerate flavours and without rooting. Since in QCD most simulations use 2+1 or 2+1+1 flavor and one wants to be able to use staggered fermions (see section 3.2.2.2) one needs to determine the fermion determinant to the power of some rational number r. This can be done by using the rational approximation

$$x^r \approx \alpha_0 + \sum_i \frac{\alpha_i}{x + \beta_i}. \tag{3.87}$$

The coefficients α_i and β_i can be determined with the Remes algorithm [53]. A Hybrid Monte Carlo algorithm that uses this rational approximation is then called a Rational Hybrid Monte Carlo (RHMC) algorithm.

3.2.4 Finite temperature and thermodynamics

To study thermodynamics on the lattice one has to introduce some definition of a temperature. This can be done by identifying the path integral on the lattice with the partition sum of statistical mechanics. The partition sum reads

$$Z = \int \mathcal{D}[U]\mathcal{D}\bar{\psi}\mathcal{D}\psi e^{-S}. \tag{3.88}$$

For a quantum mechanical system the partition sum is

$$Z(T) = \mathrm{tr}\left(e^{-\frac{\hat{H}}{k_B T}}\right) = \mathrm{tr}\left(e^{-\beta\hat{H}}\right) \tag{3.89}$$

with $\beta = \frac{1}{T}$, if k_B is set to one. Note that this is not the same β as the inverse gauge coupling introduced in section 3.2.1 and also $\hat{H}$ is not the H from the HMC algorithm, but the physical Hamiltonian. If we identify this with our path integral on the lattice the trace implies that we have to have periodicity (up to a phase factor) in the time direction. The bosonic fields are periodic in time while the fermionic fields are antiperiodic. This allows to identify the temporal extent of the lattice aN_t with the inverse temperature

$$aN_t = \frac{1}{T} = \beta. \tag{3.90}$$

If one takes the limit $\beta \longrightarrow \infty$ at constant N_t the temperature vanishes, while if $\beta \longrightarrow 0$ the temperature rises to infinity. To keep the temperature constant while taking the continuum limit aN_t has to be constant while a goes to zero. This is achieved by keeping the ratio $\frac{N_s}{N_t}$ constant while increasing N_t and N_s to approach the continuum.

As expected from a regularized theory the bare parameters depend on the cutoff, in this case the lattice spacing a. The behaviour of a and g while the continuum limit is approached can be studied in perturbation theory by the so called β-function [54]

$$-\beta(g) = a\frac{\mathrm{d}g}{\mathrm{d}a}. \tag{3.91}$$

Here one should confuse the β-function neither with the inverse coupling nor the inverse temperature. For small couplings the β-function can be expanded and then reads

$$\beta(g) = -g^3 \left(\beta_0 + \beta_1 g^2 + \beta_2 g^4 + \dots\right). \tag{3.92}$$

The first two coefficients are independent of the renormalisation scheme and were calculated in [55, 56, 57, 58] as

$$\beta_0 = \frac{1}{(4\pi)^2}\left(11 - \frac{2}{3}N_f\right), \tag{3.93}$$

$$\beta_1 = \frac{1}{(4\pi)^2}\left(102 - \frac{38}{3}N_f\right). \tag{3.94}$$

To two loop order the dependence of the lattice spacing on the bare parameter then reads [54]

$$a = \frac{1}{\Lambda}\left(\beta_0 g^2\right)^{-\frac{\beta_1}{2\beta_0^2}} \; e^{-\frac{1}{2\beta_0 g^2}}, \tag{3.95}$$

where the parameter Λ has to be determined. However if one is interested in the difference between two couplings g_1 and g_2, Λ will cancel.

If the simulation is meant to describe a physical system, this implies that the physics has to be constant as well. Therefore one has to tune the quark masses to their desired physical values for each new N_t, thus moving along a *line of constant physics* (LCP). The LCP is obtained by repeated tuning of the bare quark masses at several lattice spacings. The bare masses are tuned such that the ratios of physical observables, for example hadron masses, match the experimental results.

Historically the idea to study the confinement of quarks in gauge theories on the lattice has been introduced in 1974 by K. G. Wilson [59]. The earliest simulation algorithm is the *Metropolis* algorithm that had already been invented in 1953 [50]. 1980 M. Creutz introduced the heat bath algorithm for $SU(2)$-gauge theory on a lattice [60] that reduces the autocorrelation time compared to the Metropolis algorithm significantly. This allowed early numerical studies of the deconfinement transition in $SU(2)$ gauge theory [61, 60, 62, 63, 64]. In 1982 the heat bath algorithm was extended to $SU(N)$ gauge theories by N. Cabibbo and E. Marinari [51]. This new algorithmic development then allowed to study the $SU(3)$ deconfinement transition and thermodynamic quantities like the latent heat [65, 66, 67] on relatively small lattices with a temporal extend of typically $N_t = 4$ or $N_t = 6$. The heat bath algorithm was advanced 1985 to the so called *Kennedy-Pendleton-algorithm* [68]. In the 1990s this was used together with the overrelaxation algorithm [69] to investigate the electroweak symmetry breaking transition in the $SU(2)$-Higgs-model [70].

However in a calculation that also includes fermions the heat bath algorithm and local update algorithms in general are very inefficient due to the fermion determinant and the non locality of the action (see section 3.2.2 and section 3.2.3). A remedy for this, the Hybrid Monte Carlo algorithm, has been introduced in 1887 [71]. Anyway simulations of real QCD with dynamical fermions and physical quark masses were far out of reach at that point. In 1990 while the order of the deconfinement transition in pure $SU(3)$ gauge theory was not finally settled [72, 73], first simulations with dynamical fermions where performed [74]. This simulations where done

with staggered fermions mostly either for two or four degenerate flavours [75, 76, 77, 78]. Also first attempts towards the continuum extrapolation of the transition temperature with lattices as large as $N_t = 8$ were made [79, 80, 81].

Five years later by 1995 the value for the transition temperature in the $SU(3)$ gauge theory could be continuum extrapolated with lattices as large as $N_t = 12$ [82]. Simulations with dynamical fermions were now mostly done with two or three flavours [83], though some simulations with 2+1-flavours [84] were done as well. Besides the staggered quarks also first simulations with Wilson quarks were performed in thermodynamics [84]. Also in addition to the computation of the kind of the transition and the transition temperature other thermodynamic quantities like the equation of state were computed [85]. First steps towards finite chemical potential, at that point restricted to pure gauge simulations, were taken as well [86, 87].

About six years later in 2001 it was believed that the cost of Hybrid Monte Carlo simulations scale with the inverse quark masses as m_q^{-3} [88] making it impossible to ever reach physical quark masses on lattices large enough for continuum extrapolation. This was later known as the *Berlin Wall* problem, due to the venue of the lattice conference in 2001 in Berlin [89]. However this pessimistic outlook has been mitigated mostly due to algorithmic developments as well as the development of faster computers as for example described in [90].

Today the equation of state is known at 2+1+1-flavour over a large temperature range [7] and several attempts for calculations at finite density are made as described in section 3.2.5. The deconfinement transition at physical quark masses has been established to be crossover [91]. However the detailed structure of the Columbia plot (as described in section 3.3) still remains a mystery (see section 3.3). Also the study of some realtime quantities is now a topic for lattice QCD [92].

3.2.5 Chemical potential

The following arguments follow the discussion in [27]. For simulation without chemical potential there are on average the same number of particles and antiparticles. Therefore the expectation value of the overall baryon number density $\langle n_B \rangle$ is zero. To describe a system with finite baryon density we need to introduce a finite quark chemical potential μ_q to the Lagrangian. In the continuum this is relatively simple to achive by adding a term of the form $\overline{\psi}\gamma_4\psi$. However, on the lattice, it is not that simple. Adding a similar term to the Dirac operator leads to a divergent energy density in the continuum limit [27], which is clearly unphysical. Instead one follows the idea of Hasenfratz and Karsch in [93] where the chemical potential is understood as the temporal component of an imaginary vector field. The temporal hopping term has then the form

$$-\frac{1}{2a}\sum_{n\in\Lambda}\left(e^{\frac{\mu}{T}}(\eta_4)_{\alpha\beta}U_{\hat{4}}(n)_{ab}\delta_{n+\hat{4},m} + e^{-\frac{\mu}{T}}(\eta_4)_{\alpha\beta}U^{\dagger}_{\hat{4}}(n-\hat{4})_{ab}\delta_{n-\hat{4},m}\right). \tag{3.96}$$

It recovers the original action for $\mu = 0$ and at linear order in $a\mu$ it reproduces the correct density term with $\frac{\mu}{T} = a\mu N_t$. However this term breaks the γ_5-hermiticity of the Dirac operator and leads for real μ to a complex fermion determinant. Instead of the γ_5-hermicity of the Dirac operator where

$$\gamma_5 D \gamma_5 = D^{\dagger} \tag{3.97}$$

with a chemical potential one gets

$$\gamma_5 D(\mu)\gamma_5 = D^\dagger(-\mu). \tag{3.98}$$

This means that $e^{-\frac{\mu}{T}} = f$ is replaced by $(e^{\frac{\mu}{T}})^* = \frac{1}{f^*}$. For the determinant this yields

$$\det\left(D(f)\right) = \det\left(D\left(\frac{1}{f^*}\right)\right), \tag{3.99}$$

meaning that the determinant is only real if

$$f = \frac{1}{f^*}. \tag{3.100}$$

For real f this is only fulfilled if $f = e^{-\frac{\mu}{T}} = 1$, and therefore $\mu = 0$. However if $\mu = \mathrm{i}\mu^I$ is chosen to be purely imaginary this yields

$$f = e^{-\mathrm{i}\frac{\mu^I}{T}} \tag{3.101}$$

$$= \left(e^{\mathrm{i}\frac{\mu^I}{T}}\right)^* \tag{3.102}$$

$$= \frac{1}{f^*}. \tag{3.103}$$

Thus the determinant is real for a purely imaginary chemical potential. As described in section 3.2.3 the fermion determinant enters in the Boltzmann weight factor which has to be real to allow a Monte Carlo simulation. There have been several ideas in lattice QCD on how to obtain results at real finite chemical potential like reweighting techniques [94, 95, 96, 97], Taylor expansion [98, 99, 100, 101, 102], density of state methods [103, 104], using the canonical ensemble [105, 106, 107], formulations with dual variables [108], Lefschetz thimbles [109, 110] or complex Langevin [111, 112]. In this work we will use the fact that while we cannot do simulations at real μ, there is no problem with introducing a purely imaginary chemical potential. From this calculations we can then do an analytical continuation form $-\mu^2$ to μ^2 as illustrated in figure 3.5.

3.3 The phase diagram of QCD

In current lattice QCD there are two main phase diagrams of QCD under investigation. One is at vanishing chemical potential. It shows the dependence of the order of the deconfinement transition on the quark masses resulting in the Columbia plot (figure 3.6b) [113]. The second one is the T-μ_B-plane of the phase diagram at physical quark masses as shown in figure 3.7. For both the inclusion of imaginary chemical potential can be helpful.

For physical quark masses and $\mu_B = 0$ the deconfinement transition has been found to be an analytical crossover [114], at a temperature of approximately 160 MeV [11, 12, 13]. This is the "physical point" in figure 3.6b. For infinitely large quark masses (upper right corner) the quarks decouple and $SU(3)$ gauge theory remains. Here the deconfinement transition is

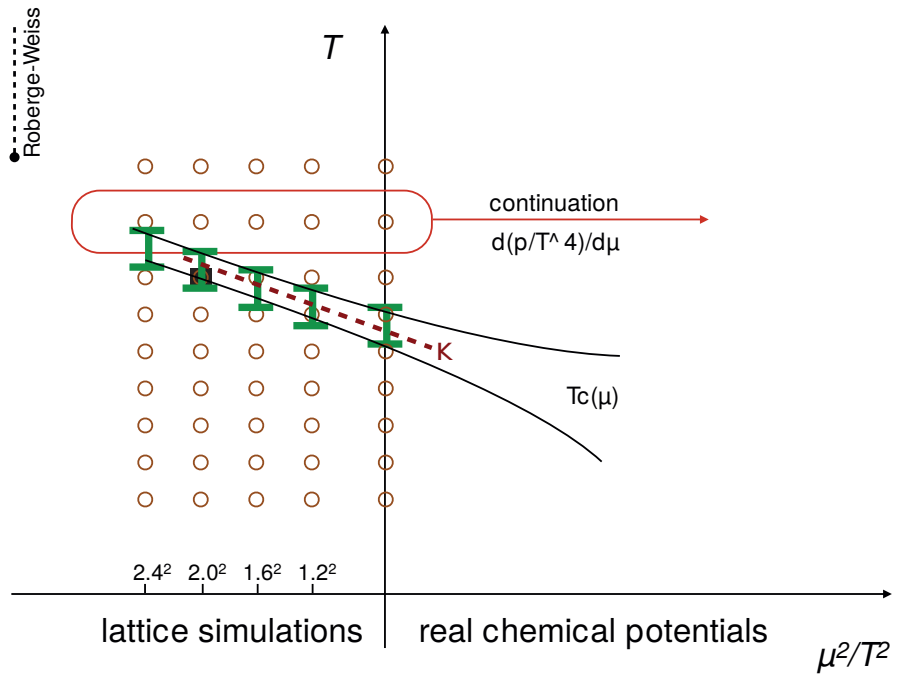

Figure 3.5: *Ilustration of the analytical continuation to real chemical potential*

well established to be of first order [91]. Since a first order phase transition does not appear isolated, a region of first order is expected. It is limited by a second order critical line, before at intermediate quark masses the transition becomes analytical. This scenario has been confirmed in [114]. While studies with only heavy quarks are computationally easier on a lattice the opposite is true for light quarks. While a similar scenario as in the upper right corner is also expected for the lower left corner, it has not been possible to find the second order critical line for low quark masses in the continuum. Therefore this topic is still under investigation [91]. Here it is helpful to extend the simulations to imaginary chemical potential where a second order transition may be realized at higher, thus more feasible, quark masses [115]. It also remains unclear whether the first order region ends for a finite strange mass as shown in figure 3.6b or if it extends to infinitely heavy strange quarks as shown in figure 3.6c.

An other popular representation of the QCD phase diagram is in the T-μ_B-plane (figure 3.7). The $\mu_B = 0$ axis is well investigated by lattice QCD [91]. For low chemical potential and temperature there is a hadronic phase of colour neutral bound states which is described in more detail in section 3.3.1. At high temperatures the effective degrees of freedom are the quarks and gluons. This phase is called the quark gluon plasma (see section 3.3.2). This two phases are separated by a crossover at low and zero chemical potential. The transition is expected to change to a first order transition for higher μ_B with a critical second order point in between. The position of the critical point is under investigation at the moment both by heavy ion collision experiments [117] and by theoretic calculations [118, 119]. For very large chemical potential a colour super conducting phase [120, 121] is expected.

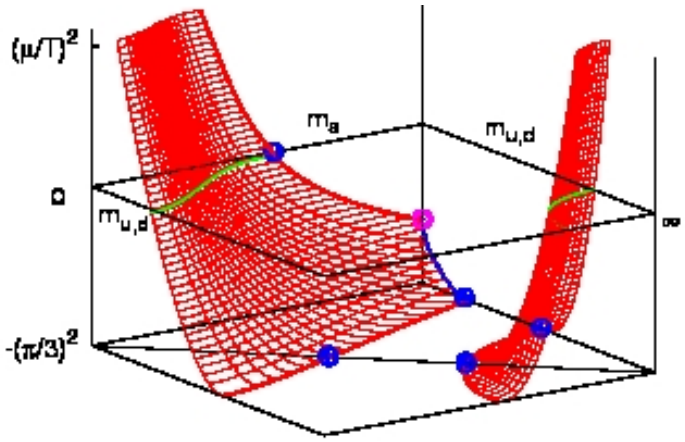

(a) *The 3d phase diagram [116]*

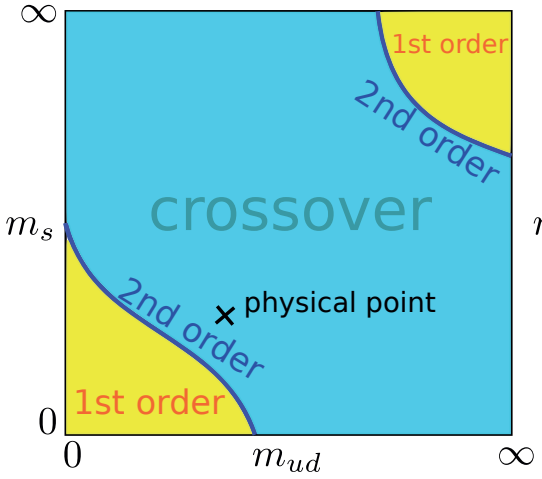

(b) *The first scenario of the Columbia plot*

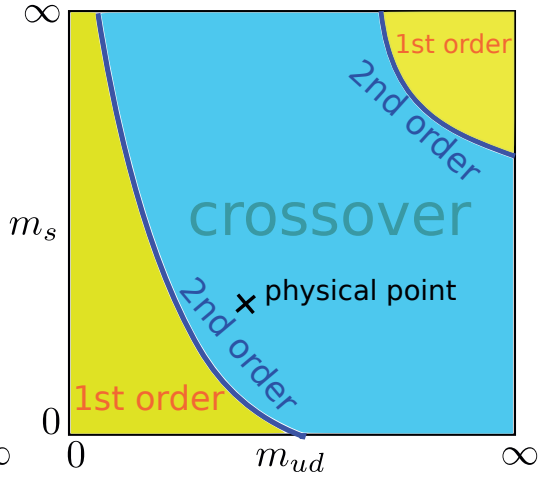

(c) *The second scenario of the Columbia plot*

Figure 3.6: *The QCD phase diagram with varied quark masses*

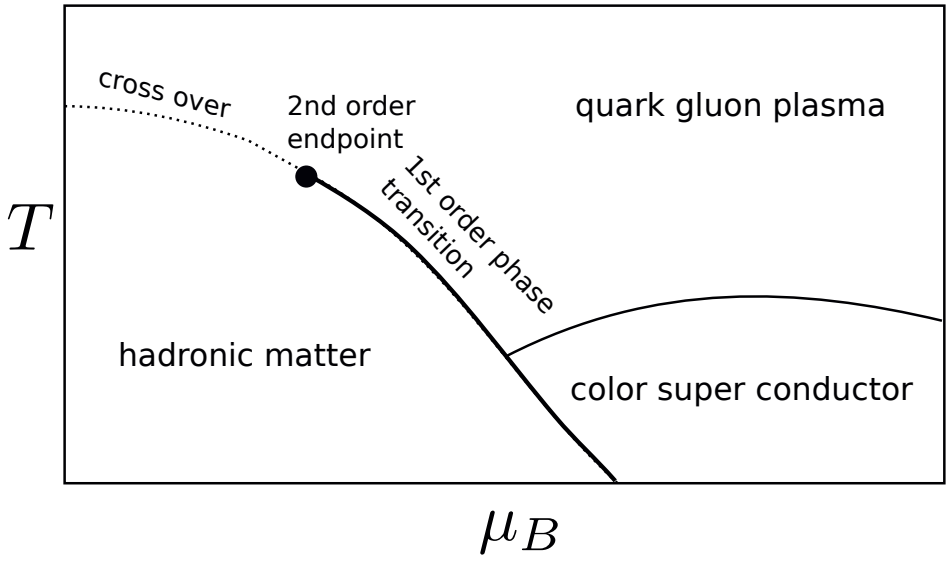

Figure 3.7: *The μ_B-T-plane of the QCD phase diagram*

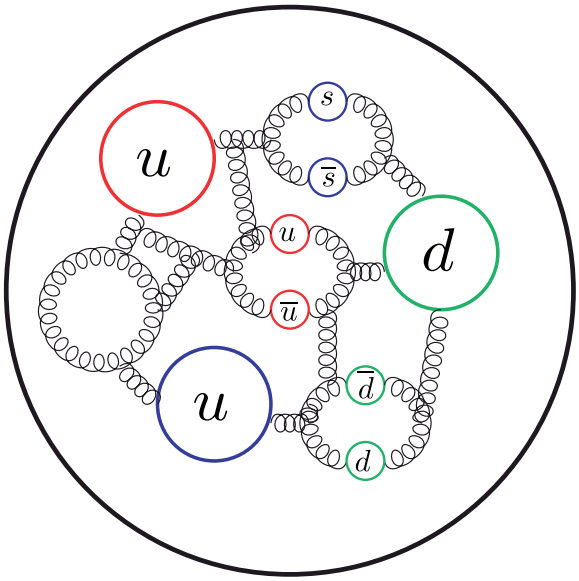

Figure 3.8: *An illustration of the quark content and the interactions for the proton. The larger quarks u, u and d represent the valence quarks while the smaller quarks always appearing as a quark-anti-quark-pair represent the sea quarks. The spirals represent the gluons. In QCD quarks and gluons as well as gluons and gluons interact with each other.*

3.3.1 Hadronic description of strong interactions

Below a transition temperature of approximately 160 MeV [11, 12, 13] quarks can only be found in colour neutral bound states: the hadrons. Hadrons can be divided in two groups of either a quark and an antiquark (mesons) or three quarks (baryons), that have been proven to exist. In principle other bound states of four, five or even more quarks are possible. Even though until now there has been no definite prove for their existence [122, 123], there is growing experimental evidence for tetra quarks, a bound state of two quarks and two antiquarks [124, 125, 126]. In the following the formulation that a particle contains quarks, refers to the so called valence quarks. Beside the valence quarks also the sea quark content is present in every state. These are quark-anti-quark-pairs that are created from the vacuum. A graphical representation for the proton with valence and sea quarks can be found in figure 3.8. The main part of the hadronic mass comes from this interaction and not from the masses of the valence quarks [16].

The first group of hadrons are the mesons. These are particles containing one quark and one antiquark. The lightest mesons are the pions that consist of up and down quarks. The second group are the baryons that consist of three quarks each with a different colour. The lightest baryon is the proton, which together with the neutron, is the main building block for common matter on earth. Other hadrons were mostly discovered by particle colliders. The largest momentarily active particle colliders are the Large Hadron Collider (LHC) at Cern in Geneva, Switzerland and the Relativistic Heavy Ion Collider (RHIC) at the Brookhaven National Laboratory (BNL) in Upton, New York, USA. A complete overview over all known hadrons and their properties can be found in [127].

On the lattice the masses of hadrons can be calculated from first principles. To do so the hadron correlators have to be calculated on zero temperature lattices. The short summary of correlators and the mass extraction that is presented here follows the discussion in [27] where a more detailed introduction can be found.

A general Euclidean corrlator $\langle \mathcal{O}_2(t)\mathcal{O}_1(0)\rangle_T$ can be defined as

$$\langle \mathcal{O}_2(t)\mathcal{O}_1(0)\rangle_T = \frac{1}{Z_T}\,\mathrm{tr}\left[e^{-(T-t)\hat{H}}\mathcal{O}_2 e^{-t\hat{H}}\mathcal{O}_1\right] \tag{3.104}$$

where $\mathcal{O}_1$ and $\mathcal{O}_2$ are two operators. In the case of hadrons they are the creation and the annihilation operator of the respective hadron. Here t is the time of the observation and T is a maximal time that will be taken to infinity later on. Z_T can be rewritten as

$$Z_T = \mathrm{tr}\left[e^{-T\hat{H}}\right] = \sum_n \langle n|e^{-T\hat{H}}|n\rangle = \sum_n e^{-TE_n}, \tag{3.105}$$

if $|n\rangle$ is a compete set of eigenstates, corresponding to the eigenvalues E_n. With another complete set of eigenvalues $|m\rangle$ the correlator can be rewritten as

$$\langle \mathcal{O}_2(t)\mathcal{O}_1(0)\rangle_T = \frac{\sum_{m,n} e^{-(T-t)E_m}e^{-tE_n}\langle m|\mathcal{O}_2|n\rangle\langle n|\mathcal{O}_1|m\rangle}{\sum_n e^{-TE_n}} \tag{3.106}$$

$$= \frac{e^{-tE_0}e^{-(T-t)E_0}\sum_{m,n} e^{-(T-t)(E_m-E_0)}e^{-t(E_n-E_0)}\langle m|\mathcal{O}_2|n\rangle\langle n|\mathcal{O}_1|m\rangle}{e^{-TE_0}\sum_n e^{-T(E_n-E_0)}} \tag{3.107}$$

$$= \frac{\sum_{m,n} e^{-(T-t)(E_m-E_0)}e^{-t(E_n-E_0)}\langle m|\mathcal{O}_2|n\rangle\langle n|\mathcal{O}_1|m\rangle}{\sum_n e^{-T(E_n-E_0)}}. \tag{3.108}$$

After taking the limit $T \longrightarrow \infty$ this yields

$$\langle \mathcal{O}_2(t)\mathcal{O}_1(0)\rangle = \sum_n \langle 0|\mathcal{O}_2|n\rangle\langle n|\mathcal{O}_1|0\rangle e^{-t\Delta E_n}. \tag{3.109}$$

with $E_n - E_0 = \Delta E_n$. For a large Euclidean time separation t the exponential functions for all ΔE_n except the lowest have vanished, leaving the energy of the ground state as the dominating contribution. Since the energy of the ground state is equivalent to the mass of a particle, the mass can be extracted from the correlator. For the determination of the mass there are two main methods. The first one is to fit the correlator $\Gamma(t)$ with one or several exponential functions. Here it might be a difficult decision which t to choose as starting point for the fit. Alternatively one uses the method of an effective mass fit, where instead of the correlator one looks at plot of $\frac{\Gamma(t)}{\Gamma(t+1)}$. This will show a plateau if the correlator is dominated by the ground state. However here it can also be difficult to identify the extend of the plateau.

Figure 3.9 shows the calculation of the light hadron spectrum form [16]. π, K and Σ were used for scale setting and to identify the physical point. They appear therefore without errorbars and in perfect agreement with the experimental values. An overview over the research effort on for the light hadron spectrum can be found in [128].

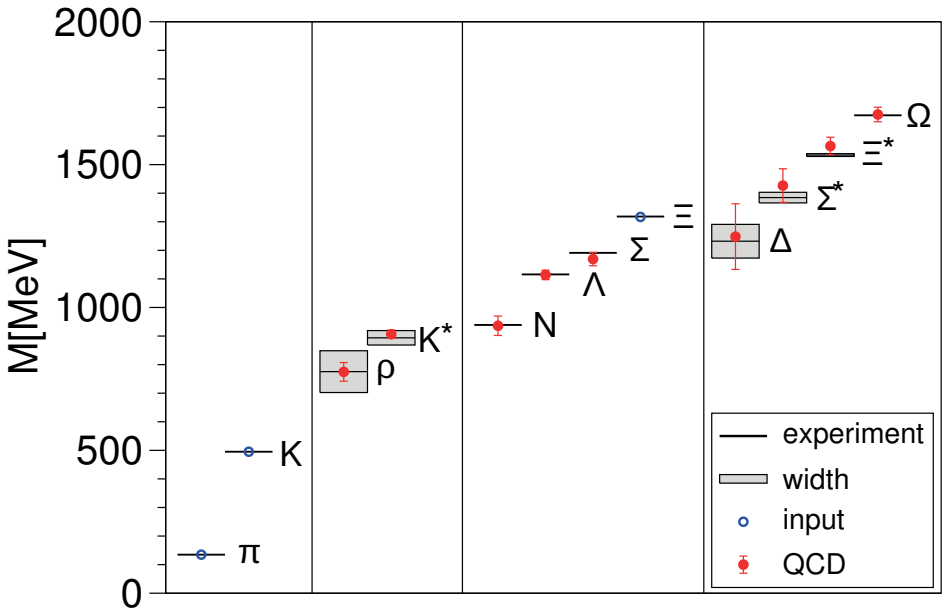

Figure 3.9: *The light hadron spectrum from [16]. For the scale setting π, K and Σ were used. Therefore they appear without errorbars and in perfect agreement with the experimental values in the plot.*

Even though the main contribution to the hadron masses comes from the strong interaction, by now lattice calculations are precise enough that QED effects become relevant. Figure 3.10 shows the mass splitting of hadrons due to QED effects from [34]. $\Delta\Xi$, $\Delta\Xi_{CC}$ and Δ_{CG} have not been found by experiment or have a larger experimental error. Therefore they are listed as predictions. If one compares the scales of figure 3.9 and figure 3.10 it becomes obvious how tiny these QED effects are.

To describe the behaviour of hadronic matter in lattice simulation one can use finite temperature simulation to compute for example the equation of state. For vanishing chemical potential it has been computed over a large temperature range [7]. Computations for the equation of state at finite chemical potential are presented in section 4.4.

Another approach to describe the behaviour of hadronic matter is the Hadron Resonance Gas (HRG) Model. It assumes that hadronic matter can be described as free gas of hadronic bound states. Then the partition sum for QCD is given as

$$\frac{1}{V}\ln Z = -\int \frac{\mathrm{d}^3 p}{(2\pi)^3} \sum_a \zeta_a g_a \ln\left(1 - \zeta_a e^{-\sqrt{p^2+M_a^2}/T}\right), \tag{3.110}$$

where M_a is the mass of a hadron or resonance, g_a is the degeneracy factor , $\zeta_a = 1$ for bosons and $\zeta_a = -1$ for fermions [129]. The thermodynamic features of QCD emerges from the summation over the infinite hierarchy of resonances [130]. This is the formula for an ideal HRG model with stable, non-interacting hadrons. There are several methods to reintroduce interactions or the broadness of the resonances (see for example [129, 131, 132]). Some of them are also including results from lattice simulations. However the results always depend on which particles are included in the first place. Figure 3.11 shows results for the calculation

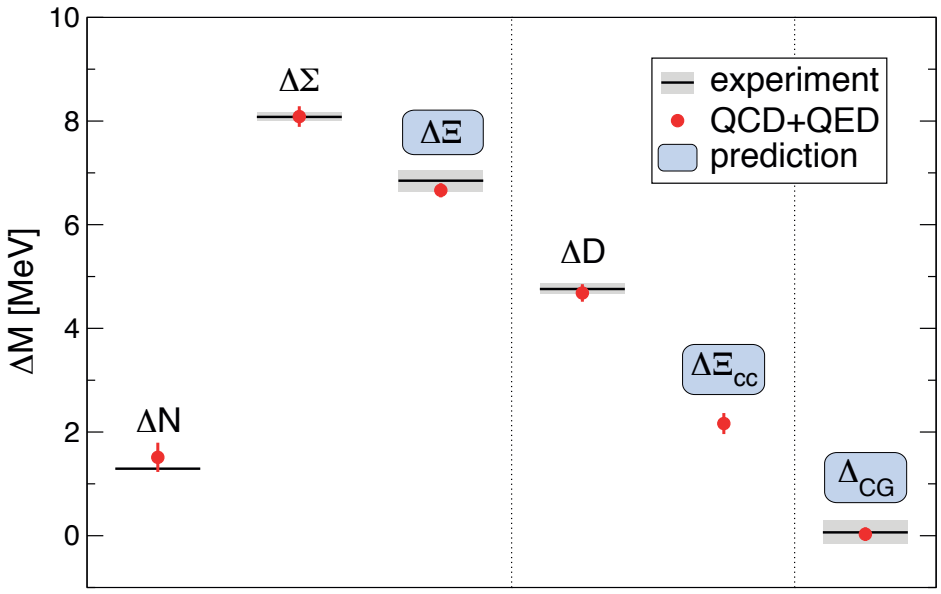

Figure 3.10: *The mass splitting of hadrons due to QED effects from [34]. $\Delta\Xi$, $\Delta\Xi_{CC}$ and Δ_{CG} had not been found by experiment at the time of the calculation or have a larger experimental error and are therefore listed as predictions.*

of the pressure within an ideal HRG model using three different lists of particles as input: first the list of the PDG from 2012, second a list of the PDG from 2014 and third a list from the PDG that does also contain particles that have been observed but not yet confirmed. As can be seen from figure 3.11 the HRG model is quite sensitive to the particle input. Therefore it might also be used to estimate areas where particles have not been found yet [133].

In any case the HRG model describes matter only in the hadronic phase. Since the transition to the Quark Gluon Plasma at zero chemical potential is a crossover it is not clear up to which temperature the HRG model is valid and it might even be different for different observables. A good assumption is however that the description by hadrons breaks down around the transition temperature.

3.3.2 Quark gluon plasma

At high temperatures or large densities quarks and gluons do no longer form bound states. The medium is in a state of quark gluon plasma (QGP). Here will only be given a very brief introduction to the QGP. A more detailed overview can be found in [134, 135, 136].

Historically there were two main ideas of what would happen if hadronic matter (see section 3.3.1) was heated to very high temperatures. In the first model, the so called Boostrap model [137], a maximum temperature is predicted. Beyond this so called *Hagedorn temperature* a further heating would produce more species of heavy hadrons but not increase the temperature any further. The second model was the Quark model. There it was thought that free quarks, so called *cosmological* quarks, existed [138]. Finally the concept of *asymptotic freedom* resolved this conflict [55, 56]. Asymptotic freedom means the vanishing of the QCD coupling at infinitely

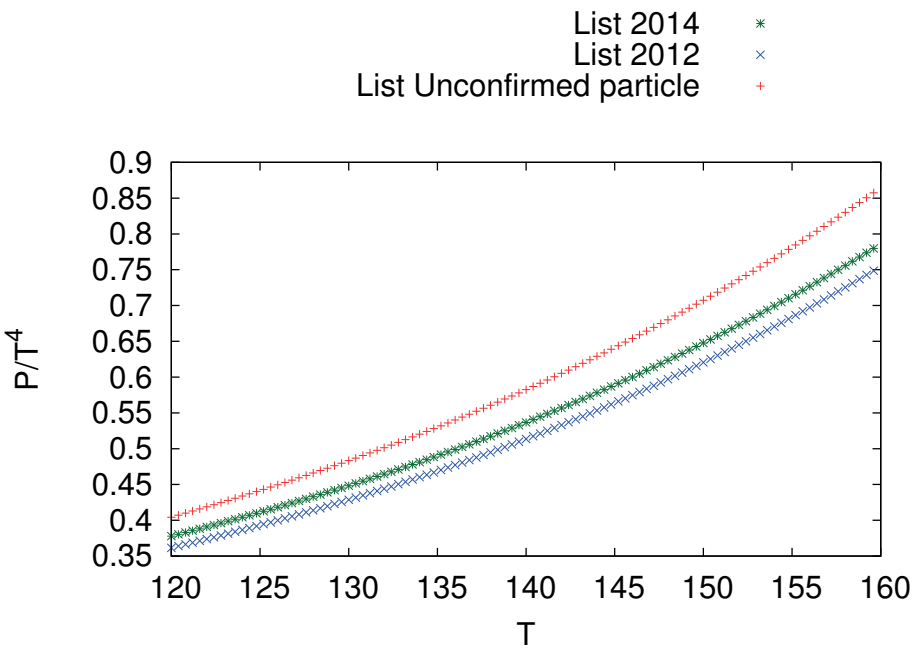

Figure 3.11: *The pressure calculated in an ideal HRG model for different lists of particles.*

high energies. Therefore with increasing temperature the interaction between the quarks gets weaker. At some point the quarks are no longer confined in hadrons [139]. This new state of matter is called quark gluon plasma.

Experimentally the quark gluon plasma was detected at RHIC in 2005 [140, 141, 142, 143]. Some earlier hints of a quark gluon plasma had also been reported from the SPS collider at Cern in collisions of lead [144]. Against common expectations the quark gluon plasma is not a free gas of quarks and gluons but a strongly interacting plasma [145, 146] with plasma parameter of $\Gamma_{QGP} = 1.5 - 6$ [147]. The plasma parameter Γ compares the strength of the coupling to the product of interparton distance and the square of the temperature. A plasma is considered strongly interacting if $\Gamma \geq 1$.

The behaviour of the quark gluon plasma can be calculated in lattice QCD at vanishing chemical potential. Figure 4.27 shows a comparison for the equation of state calculated with different actions and compared to the hadron resonance gas model. In figure 3.12b it can be seen, that even for temperatures above the phase transition the energy density does not reach the non-interacting limit, implying that even at such high energies there is a significant level of interaction left.

An interesting question for the phenomenology of heavy ion collisions is whether there is a so called *softest point* in a transition region as predicted in [150]. The softest point is a minimum in ratio of pressure and energy density $\frac{p}{\epsilon}$ as a function of ϵ. It hints to the energy range where the cooling of the plasma slows down. Since the system spends a longer time in this energy range there are specific signatures expected from that region. It also leads to a very small speed of sound. The speed of sound can be calculated in lattice QCD. The results are shown in figure 3.13.

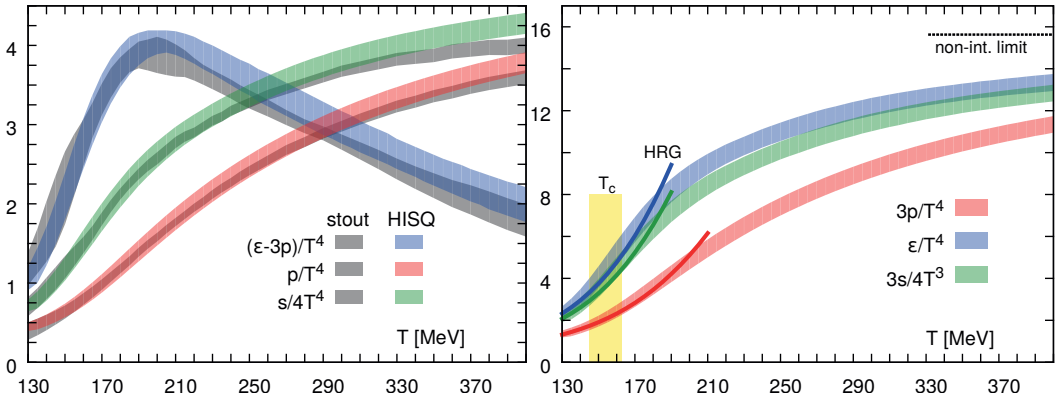

(a) *The equation of state compared for different action.*

(b) *The equation of state compared to the HRG and the ideal gas limit for the energy density.*

Figure 3.12: *The lattice and HRG results for the equation in the crossover region (marked by the yellow band)[148]. The results obtained with the stout action are from [149].*

Again these are results at vanishing chemical potential. Calculations at finite chemical potential are very difficult on the lattice (see section 3.2.5). Some attempts to reach at least small values of the chemical potential for the transition temperature and the equation of state are presented in chapter 4.

3.4 Perturbative regime

At high energies the coupling of QCD becomes small. Therefore QCD quantities become accessible by perturbation theory [151]. Still thermal perturbation theory for QCD is not straightforward due to the slow convergence of perturbative orders [152, 153]. A common remedy is the hard thermal loop resummation technique [154, 152] . A good introduction to the subject of QCD thermodynamics with hard thermal loop perturbation theory can be found in [155]. Here will be given a short summary over the possibilities and restrictions.

A four momentum $P^\mu = \left(-\mathrm{i}\omega, \quad \vec{p}\right)$ is called *soft* if both ω and $|\vec{p}|$ are of order gT for a temperature T. P^μ is called hard if either ω or $|\vec{p}|$ is of order T [156]. The simplest example for a hard loop diagram is the tadpole diagram of a scalar $g\phi^4$ theory. An example of a tadpole diagram is shown in figure 3.14. The hard thermal loop perturbation theory is an effective theory for the soft modes, while the hard loops are integrated out. The resummation scheme for QCD in terms of this hard thermal loops was introduced by Braaten and Pisarki [154]. Their scheme was a development of the static ring resummation scheme for static thermal quantities that had been invented much earlier [157]. However this scheme shows a bad convergence not only in QCD but also for simple toy models like the ϕ^4-theory [158]. This problem was solved by the introduction of a different resummation scheme for hard thermal loops in [159, 160]. The self interaction of gluons which makes QCD a non-abilean gauge theory, limits the applicability of perturbation theory for the thermodynamic potential to order $\mathcal{O}(g^6 \ln g)$ [161]. Also something called *collinear singularities* appear in some real time observables. This

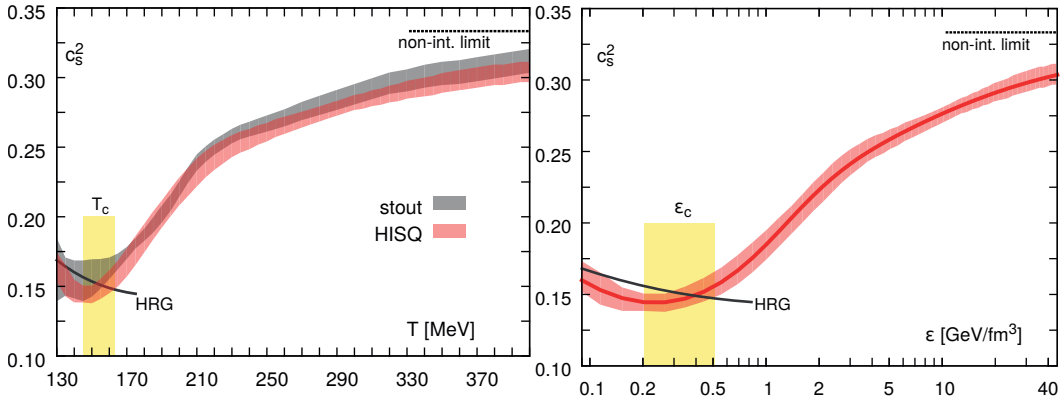

(a) *The speed of sound dependence on the temperature.*

(b) *The speed of sound dependence on the energy density.*

Figure 3.13: *The lattice and HRG results for the speed of sound in the crossover region (marked by the yellow band)[148]. The results obtained with the stout action are from [149].*

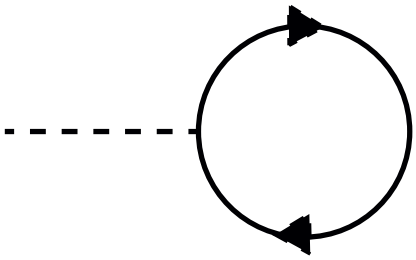

Figure 3.14: *Example of a tadpole diagram.*

is described in detail in [155]. To calculate this quantities some non-perturbative input is required. This can come, for example from lattice QCD.

To test the validity of the hard thermal loop approach it is interesting to compare results with non-perturbative calculations. Fluctuations of conserved charges or quark number susceptibilities have been calculated both in hard thermal loop-resummed thermodynamics and in lattice QCD [162, 163]. Figure 3.15 shows the comparison between calculation in the hadron resonance gas model, lattice calculation and the hard thermal loop expansion for different quark correlators.

3.5 The strong CP problem and axionic dark matter

Even though the standard model is so far extremely successful in describing our Universe, there are some riddles that are not answered completely. One of this riddles is the so called *strong CP problem*. This section will briefly describe the strong CP problem and also one proposed solution by axions as beyond standard model particles. The discussion follows [33] and [166].

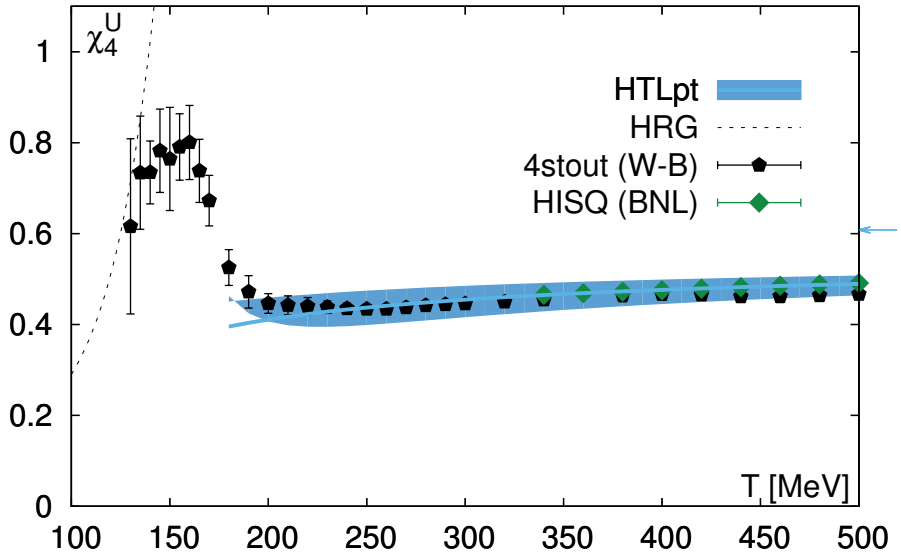

Figure 3.15: *The comparison of the lattice data from [163] and [162] with the result of the hard thermal loop expansion from [164] for the fourth order derivative of the free energy with respect to the chemical potential of the u quark [165].*

The vacuum structure of non abilean gauge theories, thus also of QCD, is non trivial. To understand this, it is convenient to concentrate on an SU(2) subgroup in the temporal gauge $A_a^0 = 0$ [167, 168]. Here the spatial field transforms under a gauge transformation as [167]

$$A^i(\vec{r}) \longrightarrow \Omega(\vec{r})A^i(\vec{r})\Omega^{-1}(\vec{r}) + \frac{\mathrm{i}}{g}\Omega(\vec{r})\nabla^i\Omega^{-1}(\vec{r}). \tag{3.111}$$

For $\vec{r} \longrightarrow \infty$ the $\Omega(\vec{r})$ go to unity. However there are different classes for which

$$\lim_{\vec{r}\longrightarrow\infty} \Omega_n(\vec{r}) = e^{2\pi \mathrm{i} n}. \tag{3.112}$$

Different vacuum configurations can then be characterized by the topological winding number n, given as

$$n = \frac{\mathrm{i}g^3}{24\pi^2}\int \mathrm{d}^3 r\, \mathrm{tr}\left(\epsilon_{ijk}A^iA^jA^k\right). \tag{3.113}$$

This formulas are also valid for QCD. One can construct a gauge invariant vacuum state $|\theta\rangle$ in terms of the degenerate states $|n\rangle$ as

$$|\theta\rangle = \sum_n e^{\mathrm{i}n\theta}|n\rangle. \tag{3.114}$$

This non trivial vacuum structure can be interpreted as an effective interaction, that can be written in the Lagrangian as

$$\mathcal{L}_\theta = \frac{g^2}{32\pi^2}\theta F^{a\mu\nu}\tilde{F}^a_{\mu\nu}. \tag{3.115}$$

This term describes an additional interaction of the gauge fields that violates P and CP. However this is not the only source for CP violation. Another one comes from the spontaneous symmetry breaking of the electroweak gauge symmetry. The mass term for the quark fields reads [169]

$$\mathcal{L}_{\text{mass}} = \bar{q}_R \mathcal{M} q_L + \bar{q}_L \mathcal{M}^\dagger q_R \tag{3.116}$$

with the quark mass matrix $\mathcal{M}$. $\mathcal{M}$ can in general be complex. To write this term in a physical basis one has to diagonalize $\mathcal{M}$. In the process one does a chiral transformation that changes θ by $\arg(\det \mathcal{M})$. Therefore the whole CP violating term for QCD reads

$$\mathcal{L}_{CP} = \frac{g^2}{32\pi^2} \bar{\theta} F^{a\mu\nu} \tilde{F}^a_{\mu\nu} \tag{3.117}$$

where

$$\bar{\theta} = \theta + \arg(\det \mathcal{M}). \tag{3.118}$$

However this extra term in the Lagrangian is not only CP violating, it can also be related to an electric dipole moment for the neutron which is proportional to $\bar{\theta}$. These effects are not observed in nature. If there were at least one massless quark species the term proportional to θ could be removed by a chiral rotation of the quark masses. But this is not the case either. Therefore $\bar{\theta}$ must be extremely small. Experimentally it can be shown [32] that

$$|\bar{\theta}| < 10^{-9}. \tag{3.119}$$

The question of why the two contributions to $\bar{\theta}$ cancel in a way that leaves $\bar{\theta}$ so small (or even zero) is called the strong CP problem.

An attractive solution to this problem was proposed in 1977 by Peccei and Quinn [170]. They proposed to take $\bar{\theta}$ as an dynamical field which goes to zero due to its classical potential [33]. This is accomplished by introducing an additional spontaneously broken $U(1)_{PQ}$ symmetry. The spontaneously broken symmetry results in an additional Nambu-Goldstone boson [171, 172], that is called *axion*. Due to a chiral anomaly in the PQ symmetry the axion has a mass of order $\frac{\Lambda_{QCD}}{f_{PQ}}$ where f_{PQ} is the scale of the spontaneous symmetry breaking. This yields an additional term in the Lagrangian for the axion field φ

$$\mathcal{L}_{\text{axion}} = C_{\text{axion}} \frac{\varphi}{f_{PQ}} \frac{g^2}{32\pi^2} F^{a\mu\nu} \tilde{F}^a_{\mu\nu} \tag{3.120}$$

where C_{axion} is a model depend constant. This term together with $\mathcal{L}_{CP}$ form a potential that is minimized if

$$\langle \varphi \rangle = -\frac{\bar{\theta} f_{PQ}}{C_{\text{axion}}}. \tag{3.121}$$

With this value for $\langle \varphi \rangle$ the $\bar{\theta}$ term gets cancelled. In this theory there are no restrictions on f_{PQ} and therefore on the mass of the axion. Since there has been no detection of axions yet their interaction with normal matter can be assumed to be small. This makes the axion a candidate for a dark matter particle. Under some assumptions it is possible to narrow down the axion mass. For example if one assumes that the axions were created after the inflation period in a so called *misalignment* mechanism, and one assumes some number for today's

axion density it is possible to determine the axion mass from the equation of state and the topological charge susceptibility.

The misalignment mechanism is described in detail in [166] and a summary is given in [7]. First we shift the angle $\bar{\theta}$ taking

$$\theta_a = \bar{\theta} + C_{\text{axion}} \frac{\langle \varphi \rangle}{f_{PQ}} \tag{3.122}$$

where θ_a is called the axion angle. Then the mechanism involves solving the equation of motion for θ_a which is given as

$$\frac{\mathrm{d}^2\theta_a}{\mathrm{d}t^2} + 3H(T)\frac{\mathrm{d}\theta_a}{\mathrm{d}t} + m_a^2(T)\sin\theta_a = 0 \tag{3.123}$$

where m_a is the axion mass and H is the Hubble parameter. The evolution of the axion can be split in three stages [166]:

1. While the Compton wavelength is larger then the Hubble scale, the axion is nearly massless.

2. At a scale of $m_a \approx 3H$ the axion starts to roll down towards the minimum at $\theta_a = 0$ where it starts oscillating.

3. Axions become indistinguishable from pressureless matter and $\frac{n_a}{s}$ is conserved.

A numerical solution from [166] that shows these three phases. It can be seen in figure 3.16.

If one assumes that θ_a changes slowly in space one can get from the Friemann equations [7]:

$$H^2 = \frac{8\pi}{3M_{Pl}^2}\rho \tag{3.124}$$

$$\frac{\mathrm{d}\rho}{\mathrm{d}t} = -H(\rho + p) = -3HsT \tag{3.125}$$

where M_{Pl} is the Plank mass, ρ is the energy density, p is the pressure and s is the entropy density. Since at the temperatures where the axion production takes place, the axion contribution to ρ and s is negligible, the equation of state of the standard model can be used. In [7] the effective degrees of freedom g_ρ and g_s have been calculated. They can be related to ρ and s as

$$\rho = \frac{\pi^2}{30} g_\rho T^4 \tag{3.126}$$

$$s = \frac{2\pi^2}{45} g_s T^3. \tag{3.127}$$

The combination of those equations yields

$$\frac{\mathrm{d}t}{\mathrm{d}T} = -M_{Pl}\sqrt{\frac{45}{64\pi^3}}\frac{1}{T^3 g_s \sqrt{g_\rho}}\left(T\frac{\mathrm{d}g_\rho}{\mathrm{d}T} + 4g_\rho\right). \tag{3.128}$$

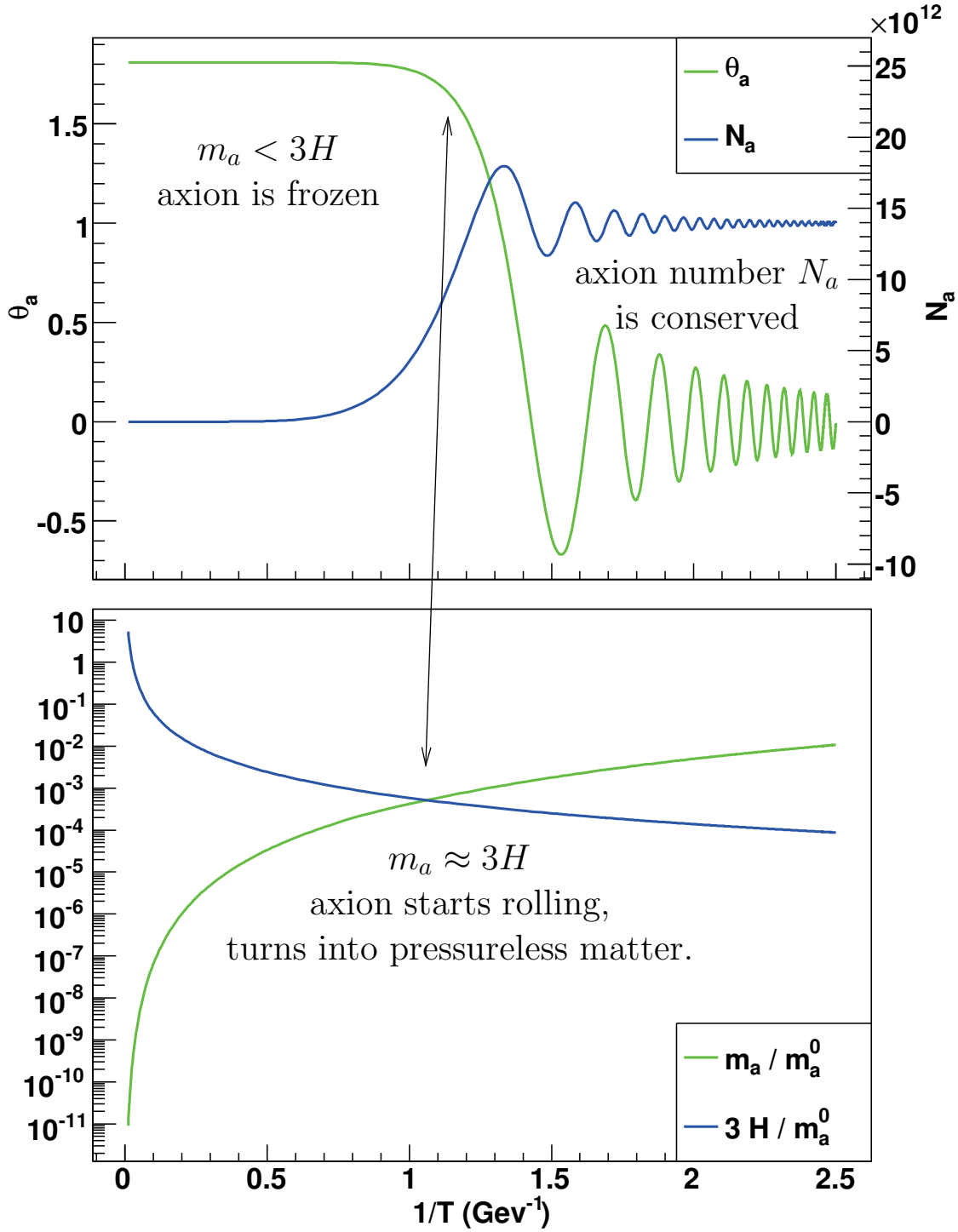

Figure 3.16: *A numerical solution for the axion dynamics from [166]. For $m_a < 3H$ the axion mass remains small. Then at $m_a \approx 3H$ it increase and the axion angle starts oscillating around zero. Finally θ_a and the axion density reach a nearly constant value.*

Together with the equation of motion this results in the equation

$$\frac{\mathrm{d}^2\theta_a}{\mathrm{d}T^2} + \left[3H(T)\frac{\mathrm{d}t}{\mathrm{d}T} - \frac{\mathrm{d}^2t}{\mathrm{d}T^2}\Big/\frac{\mathrm{d}t}{\mathrm{d}T}\right]\frac{\mathrm{d}\theta_a}{\mathrm{d}T} + \frac{\chi(T)}{f_A^2}\left(\frac{\mathrm{d}t}{\mathrm{d}T}\right)^2 \sin\theta = 0. \tag{3.129}$$

This equation then has to be integrated over the three stages of the dynamics described above. In the last stage where the oscillation already slows down on can extract the ratio $\frac{n_a}{s}$ by averaging the expression

$$\frac{n_a}{s}(T) = \frac{45}{2\pi^2}\frac{f_A^2}{m_A g_s T^3}\left[\frac{1}{2}\left(\frac{\mathrm{d}\theta_a}{\mathrm{d}T}\Big/\frac{\mathrm{d}t}{\mathrm{d}T}\right)^2 + \frac{\chi(T)}{f_A^2}(1-\cos\theta)\right] \tag{3.130}$$

for the temperature range $0.8T_s$ – $0.2T_s$ [7]. Here T_s is the temperature where the first sign change in θ_a happens. From the conservation of the ratio $\frac{n_a}{s}$ one can calculate

$$n_{a;\mathrm{today}} = \frac{n_a(T)}{s(T)} s_{\mathrm{today}} \tag{3.131}$$

$$\rho_{a;\mathrm{today}} = m_A n_{a;\mathrm{today}} \tag{3.132}$$

The entropy density in the Universe can be calculated from the temperature T_γ of cosmic microwave background. If one then assumes that a certain percentage of the dark matter is composed of axions, one can estimate the axion mass from the equation of state and the topological susceptibility. A calculation of the topological susceptibility is presented in section 5.

4 The QCD phase diagram from imagnary μ_B

To analyse the quark gluon plasma that is created in heavy ion collision experiments at the LHC or RHIC a theoretical understanding of the quark gluon plasma in QCD is needed. In the region of the deconfinement transition lattice QCD is a good tool to study QCD since this area can not be accessed perturbatively. At the moment direct simulations that are continuum extrapolated and at physical quark masses are restricted to vanishing or imaginary chemical potential (see section 3.2.5). On the other hand the collisions especially at RHIC take place away from the axis of zero μ_B [173]. Therefore information in that region are needed. Even though it is not possible to do direct lattice simulations, it is possible to extrapolate observables from zero or imaginary chemical potential. This method is called analytical continuation.

In this chapter we will present results that are gained from simulations at zero and imaginary μ_B. The analysed quantities are then ploted against the μ_B^2 axes and the function is analytical continued to the realm of finite chemical potential. An illustration of this is shown in figure 3.5. An other possibility is to determine the Taylor coefficients of the function that discribes a quantities from the derivatives of the partition sum at zero chemical potential. The Taylor coefficients can then be used to extrapolate to finite chemical potential.

The results that are presented in this section have been published in [5, 6, 174, 175].

4.1 Matching experimental conditions

Since our analysis is supposed to serve as input for the investigation of the quark gluon plasma that is created in heavy ion collisions it is important to match the experimental conditions as closely as possible. This means mainly two things. First of all if we introduce a baryon chemical potential μ_B in our simulation. This will also introduce some baryons with strange content and therefore a nonvanishing strange number n_S. In the experiments however the gold or lead ions used in the collision have no net strange content. Therefore we have to introduce a strangeness chemical potential μ_S that compensates for the strange content through μ_B. Since tuning parameters in the simulation is expensive and time consuming it is very helpful if one can predict the correct value for μ_S in advance. Therefore I will describe a method [5, 175] to reach the strangeness neutral point for the simulation by solving the differential equation $\langle n_S \rangle = 0 \Leftrightarrow 0 = \frac{\partial \log Z}{\partial\ \mu_S}$.

The second point is that the ratio between the charge and the baryon number for gold or lead is $\frac{\langle n_Q \rangle}{\langle n_B \rangle} \approx 0.4$. In principle it is possible to introduce isospin asymmetry in lattice calculation. However again this would increase the tuning effort and make our calculations more expensive, since then the up and down quarks require separate pseudo-fermion fields in the RHMC algorithm. Therefore here we will use the easier way of doing the simulations for the isospin

symmetric case and then later extrapolate from $\frac{\langle n_Q \rangle}{\langle n_B \rangle} = 0.5$ to the physical ratio $\frac{\langle n_Q \rangle}{\langle n_B \rangle} = 0.4$. The necessary calculations for this extrapolations are also described here.

4.1.1 Notation

The various derivatives of the free energy are here named as

$$\chi_{q_1 q_2 \dots q_n} = -\frac{1}{T^4} \frac{\partial^n}{\partial(\mu_{q_1}/T)\partial(\mu_{q_2}/T)\dots\partial(\mu_{q_n}/T)} \frac{T}{V} \log Z \tag{4.1}$$

where $q_1 \dots q_n$ are generic flavours. It is important to note that even if the u and the d quark are degenerate $\chi_{ud} \neq \chi_{uu}$. This is because even though the u and the d quark are simulated with degenerate masses, they are still independent particles. But because of the degeneracy $\chi_{dd} = \chi_{uu}$. The influence of the charm quark is small compared to the influence of the lighter quarks as it can be seen in figure 4.1. Therefore it will be neglected in this calculation. This leads to four independent derivatives of second order in the basis of $\{u, d, s\}$: χ_{uu}, χ_{ud}, χ_{us} and χ_{ss}. It is also possible to use the basis of $\{B, Q, S\}$. To change between them one can use the relations

$$\mu_u = \frac{1}{3}\mu_B + \frac{2}{3}\mu_Q \tag{4.2}$$

$$\mu_d = \frac{1}{3}\mu_B - \frac{1}{3}\mu_Q \tag{4.3}$$

$$\mu_s = \frac{1}{3}\mu_B - \frac{1}{3}\mu_Q - \mu_S. \tag{4.4}$$

If one changes to the basis of $\{B, Q, S\}$ there are six different derivatives of second order: χ_{BB}, χ_{BS}, χ_{BQ}, χ_{QS}, χ_{QQ} and χ_{QS} which are not independent.

4.1.2 Solving the differential equation

We assume we know the value for $\mu_S(\mu_B)$ so that $\langle n_s \rangle = 0$ for $\mu_S(\mu_B^0)$ and $\mu_S(\mu_B^0 - \Delta\mu_B)$ with all the derivatives. Now we want to know the value for $\mu_S(\mu_B^0 + \Delta\mu_B)$. This we can get by doing a step with the Runge-Kutta-algorithm of second order as

$$\mu_s(\mu_B^0 + \Delta\mu_B) = \mu_S(\mu_B^0 - \Delta\mu_B) + 2\Delta\mu_B \frac{\mathrm{d}\mu_s}{\mathrm{d}\mu_B}(\mu_B^0). \tag{4.5}$$

Due to the nature of numerical simulations for the simulations with μ_B^0 and $\mu_B^0 - \Delta\mu_B$, μ_S is not precisely tuned. To repeat the simulation would be very expensive therefore we need to find a way to correct μ_S and $\frac{\mathrm{d}\mu_s}{\mathrm{d}\mu_B}$ so that they are at the strangeness neutral point. This is fairly easy for μ_S. We want to solve the differential equation

$$\langle n_S \rangle = 0 \Leftrightarrow \frac{\partial \log Z}{\partial \mu_S} = 0. \tag{4.6}$$

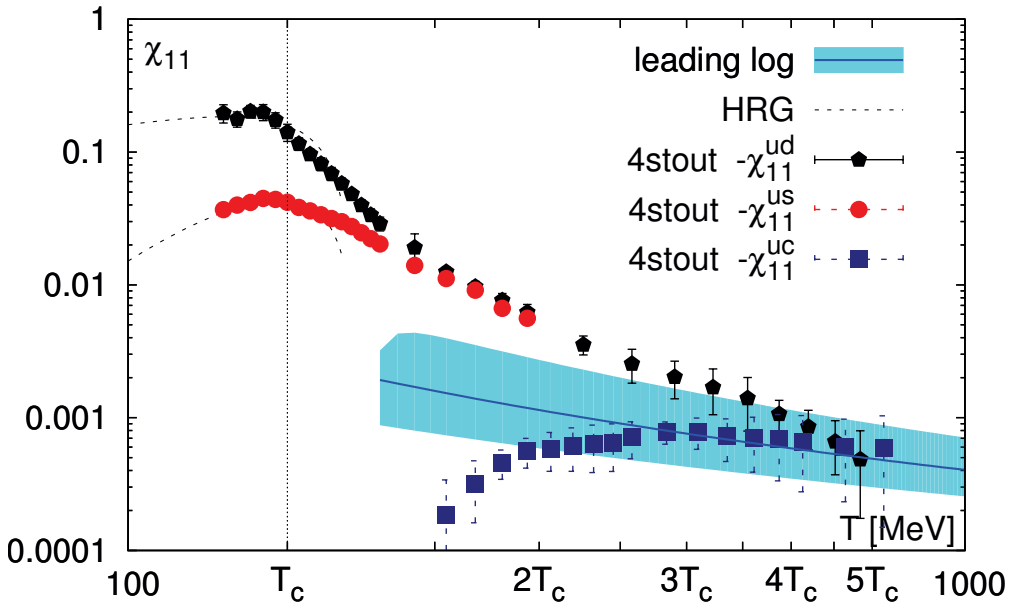

Figure 4.1: *The light, strange and charm contributions to the disconnected diagrams below and above T_c with a comparison between calculation in the hadron resonance gas model, lattice calculation and perturbative calculations for different quark correlators [165]. The results for perturbative calculations are from [176]*

Assuming we know the correct value of μ_S for one μ_B so that $\langle n_S \rangle = 0$ and now want to know it for another value of μ_B. We assume that the correct value of μ_S is $\tilde{\mu}_S = \mu_S + \Delta\mu_S$. We then can write

$$\langle n_S \rangle = \frac{\partial \log Z}{\partial \tilde{\mu}_S} \tag{4.7}$$

$$= \frac{\partial \log Z}{\partial \mu_S} + \frac{\partial^2 \log Z}{\partial \mu_S^2} \Delta\mu_S \tag{4.8}$$

$$= 0. \tag{4.9}$$

This yields

$$\Delta\mu_S = -\frac{\chi_S}{\chi_{SS}}. \tag{4.10}$$

An example of the resulting values of μ_S for several μ_B can be found in figure 4.2.

At this point one should not confuse the role of $\Delta\mu_B$ and $\Delta\mu_S$. While $\Delta\mu_B$ is the step size in the Runge-Kutta-algorithm that can be chosen freely, as long as it is not too large, $\Delta\mu_S$ is the deviation from the strangeness neutral point, that is calculated by a Taylor expansion.

The correction of the derivative of μ_S with respect to μ_B is a little bit more complicated. First we need to determine the derivative $\frac{\mathrm{d}\tilde{\mu_s}}{\mathrm{d}\mu_B} = \frac{\partial\tilde{\mu_s}}{\partial\mu_B}$. Therefor we look at the second order derivative of the partition function

$$\frac{\mathrm{d}}{\mathrm{d}\mu_B}\left(\frac{\partial \ln Z}{\partial\tilde{\mu_S}}\right) = \frac{\partial^2 \ln Z}{\partial\tilde{\mu_S}\partial\mu_B} + \frac{\partial^2 \ln Z}{\partial\tilde{\mu_S}^2}\frac{\mathrm{d}\tilde{\mu_s}}{\mathrm{d}\mu_B} \tag{4.11}$$

$$= \tilde{\chi}_{BS} + \tilde{\chi}_{SS}\frac{\mathrm{d}\tilde{\mu_s}}{\mathrm{d}\mu_B} \tag{4.12}$$

$$= 0 \tag{4.13}$$

This yields

$$\frac{\mathrm{d}\tilde{\mu_s}}{\mathrm{d}\mu_B} = -\frac{\tilde{\chi}_{SB}}{\tilde{\chi}_{SS}}|_{\langle n_s\rangle=0} \tag{4.14}$$

$$= -\frac{\chi_{SB}}{\chi_{SS}} - \frac{\chi_{SSB}\chi_{SS} - \chi_{SSS}\chi_{SB}}{(\chi_{SS})^2}\Delta\mu_S + \mathcal{O}(\Delta\mu_S^2) \tag{4.15}$$

$$= -\frac{\chi_{SB}}{\chi_{SS}} - \Delta\mu_S\left(\frac{\chi_{SSB}}{\chi_{SS}} - \frac{\chi_{SSS}\chi_{SB}}{(\chi_{SS})^2}\right) + \mathcal{O}(\Delta\mu_S^2) \tag{4.16}$$

With the value for $\Delta\mu_S$ from equation 4.10 we get the correct value of the derivative as well.

4.1.3 Extrapolating to $\langle n_S\rangle = 0$ and $0.4\langle n_B\rangle = \langle n_Q\rangle$

As already mentioned the experiments fulfil the constrains $\langle n_S\rangle = 0$ and $0.4\langle n_B\rangle = \langle n_Q\rangle$. As described above we tune our simulation parameters to the strangness neutral point. Because of the nature of numerical simulations we will never reach it perfectly and need to extrapolate, as can be seen in figure 4.3. In addition our simulations are at $0.5\langle n_B\rangle = \langle n_Q\rangle$, the isospin symmetric point. But in heavy ion collision experiments $0.4\langle n_B\rangle = \langle n_Q\rangle$ is realized. Simulations away from the isospin symmetric point would be complicated and result in more tuning efforts. Since the difference is only small it is possible and easier to extrapolate the data to $0.4\langle n_B\rangle = \langle n_Q\rangle$ via another Taylor expansion. The aim is to calculate $\frac{\mathrm{d}P/T^4}{\mathrm{d}\mu_B}$ at $\langle n_S\rangle = 0$ and $0.4\langle n_B\rangle = \langle n_Q\rangle$. It is

$$\frac{\mathrm{d}P/T^4}{\mathrm{d}\mu_B} = \frac{T}{V}\frac{\mathrm{d}}{\mathrm{d}\mu_B}\ln Z \tag{4.17}$$

$$= \frac{T}{V}\left(\frac{\partial \ln Z}{\partial\mu_B} + \frac{\partial \ln Z}{\partial\mu_S}\frac{\mathrm{d}\mu_S}{\mathrm{d}\mu_B} + \frac{\partial \ln Z}{\partial\mu_Q}\frac{\mathrm{d}\mu_Q}{\mathrm{d}\mu_B}\right) \tag{4.18}$$

$$= \chi_B + \chi_S\frac{\mathrm{d}\mu_S}{\mathrm{d}\mu_B} + \chi_Q\frac{\mathrm{d}\mu_Q}{\mathrm{d}\mu_B} \tag{4.19}$$

To extrapolate this expression, we will extrapolate the single terms

$$\chi_B \longrightarrow \chi_B + \chi_{BQ}\Delta\mu_Q + \chi_{BS}\Delta\mu_S \tag{4.20}$$

$$\chi_S \longrightarrow 0 \tag{4.21}$$

$$\chi_Q \longrightarrow 0.4\chi_B \tag{4.22}$$

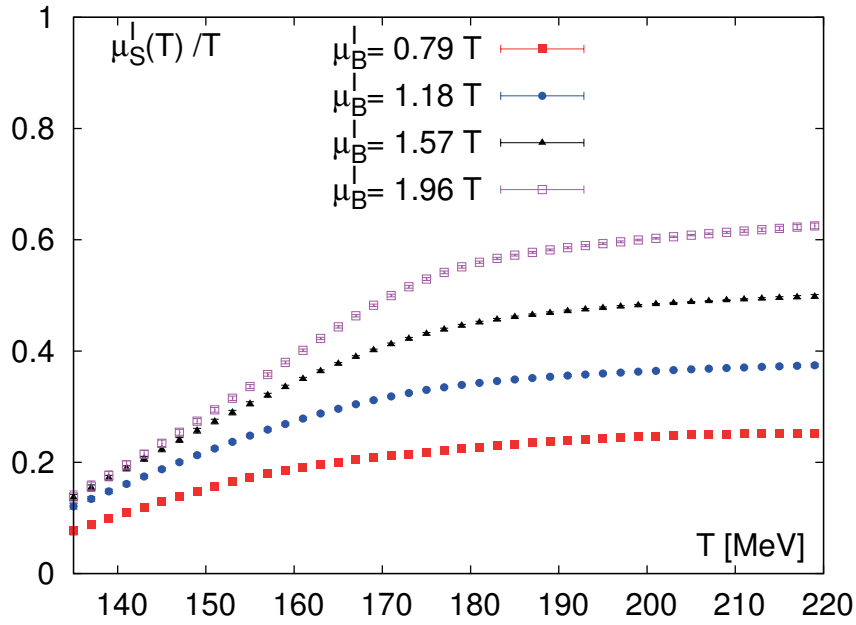

Figure 4.2: *The correct value of μ_S that is gained from the solving of the differential equation $\langle n_S \rangle = 0$ for several values of T and μ_B [5]*

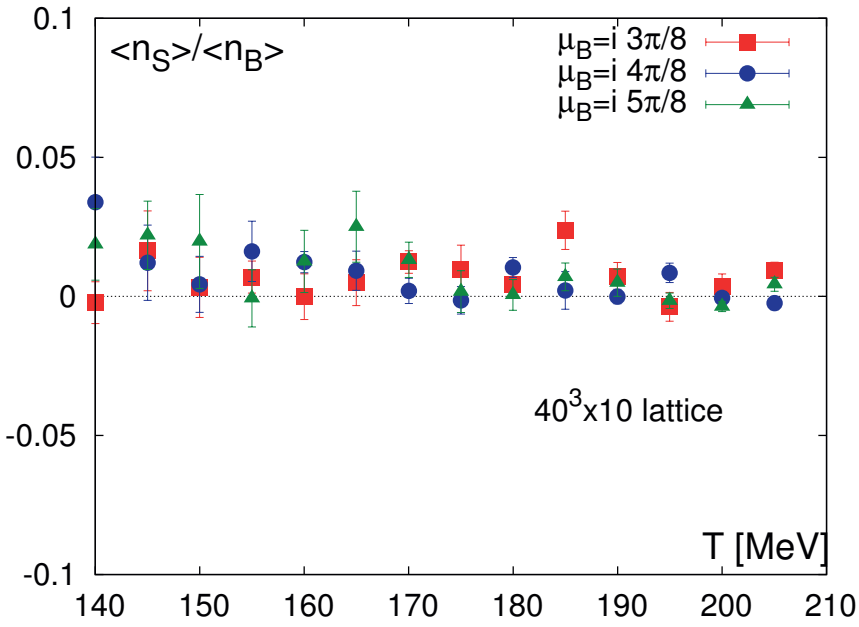

Figure 4.3: *The deviation from zero of strangeness after the simulation [177].*

The extrapolated value of $\frac{\widetilde{\mathrm{d}P/T^4}}{\mathrm{d}\mu_B}$ then is given as

$$\frac{\widetilde{\mathrm{d}P/T^4}}{\mathrm{d}\mu_B} = \chi_B + \chi_{BQ}\Delta\mu_Q + \chi_{BS}\Delta\mu_S + 0.4\chi_B\left(\frac{\mathrm{d}\mu_Q}{\mathrm{d}\mu_B} + \Delta\mu_Q\frac{\partial}{\partial\mu_Q}\left(\frac{\mathrm{d}\mu_Q}{\mathrm{d}\mu_B}\right)\right) \tag{4.23}$$

$$+ \chi_{QS}\Delta\mu_S\frac{\mathrm{d}\mu_Q}{\mathrm{d}\mu_B} + \chi_Q\Delta\mu_S\frac{\partial}{\partial\mu_S}\left(\frac{\mathrm{d}\mu_Q}{\mathrm{d}\mu_B}\right) \tag{4.24}$$

$\frac{\mathrm{d}\mu_Q}{\mathrm{d}\mu_B}$, $\frac{\mathrm{d}\mu_S}{\mathrm{d}\mu_B}$, $\Delta\mu_Q$ and $\Delta\mu_S$ can be determined from the equations (4.20) to (4.22). For the derivatives we derive the conditions with respect to μ_B yielding

$$0 = \chi_S \tag{4.25}$$

$$= \chi_{BS} + \chi_{SS}\frac{\mathrm{d}\mu_S}{\mathrm{d}\mu_B} + \chi_{QS}\frac{\mathrm{d}\mu_Q}{\mathrm{d}\mu_B} \tag{4.26}$$

and

$$0.4\chi_B = \chi_Q \tag{4.27}$$

$$\Rightarrow \chi_{BB} + \chi_{BS}\frac{\mathrm{d}\mu_S}{\mathrm{d}\mu_B} + \chi_{BQ}\frac{\mathrm{d}\mu_Q}{\mathrm{d}\mu_B} = \chi_{BQ} + \chi_{QS}\frac{\mathrm{d}\mu_S}{\mathrm{d}\mu_B} + \chi_{QQ}\frac{\mathrm{d}\mu_Q}{\mathrm{d}\mu_B}. \tag{4.28}$$

Solving for $\frac{\mathrm{d}\mu_Q}{\mathrm{d}\mu_B}$ and $\frac{\mathrm{d}\mu_S}{\mathrm{d}\mu_B}$, μ_Q leads to

$$\frac{\mathrm{d}\mu_Q}{\mathrm{d}\mu_B} = \frac{\left(0.4\chi_{BS} - \chi_{QS}\right)\chi_{BS} - \left(0.4\chi_{BB} - \chi_{BQ}\right)\chi_{SS}}{\left(0.4\chi_{BQ} - \chi_{QQ}\right)\chi_{SS} - \left(0.4\chi_{BS} - \chi_{QS}\right)\chi_{QS}} \tag{4.29}$$

$$\frac{\mathrm{d}\mu_S}{\mathrm{d}\mu_B} = -\frac{\chi_{QS}\frac{\mathrm{d}\mu_Q}{\mathrm{d}\mu_B} + \chi_{BS}}{\chi_{SS}}. \tag{4.30}$$

To get the extrapolated values of the derivatives it is easiest to replace each χ_{XY} by the extrapolated values $\chi_{XY}^{(e)} = \chi_{XY} + \chi_{XYS}\Delta\mu_S + \chi_{XYQ}\Delta\mu_Q$. On the other hand we can solve the conditions

$$0 = \chi_S + \Delta\mu_Q\chi_{QS} + \Delta\mu_S\chi_{SS} \tag{4.31}$$

$$0.4\chi_B + \Delta\mu_Q\chi_{BQ} + \Delta\mu_S\chi_{BS} = \chi_Q + \Delta\mu_Q\chi_{QQ} + \Delta\mu_S\chi_{QS} \tag{4.32}$$

for $\Delta\mu_Q$ and $\Delta\mu_S$ yielding

$$\Delta\mu_S = \frac{\left(0.4\chi_B - \chi_Q\right)\chi_{QS} + \left(\chi_{QQ} - 0.4\chi_{BQ}\right)\chi_S}{\left(\chi_{QS} - 0.4\chi_{BS}\right)\chi_{QS} - \left(\chi_{QQ} - 0.4\chi_{BQ}\right)\chi_{SS}} \tag{4.33}$$

$$\Delta\mu_Q = -\frac{\chi_S + \Delta\mu_S\chi_{SS}}{\chi_{QS}}. \tag{4.34}$$

Both strategies only differ in higher orders, and the numerical difference is about one order of magnitude smaller than the statistical error of the quantities.

An example of the difference between the direct simulation and the data after the extrapolation can be seen in figure 4.4. The blue data are at the strangeness neutral point. The values from

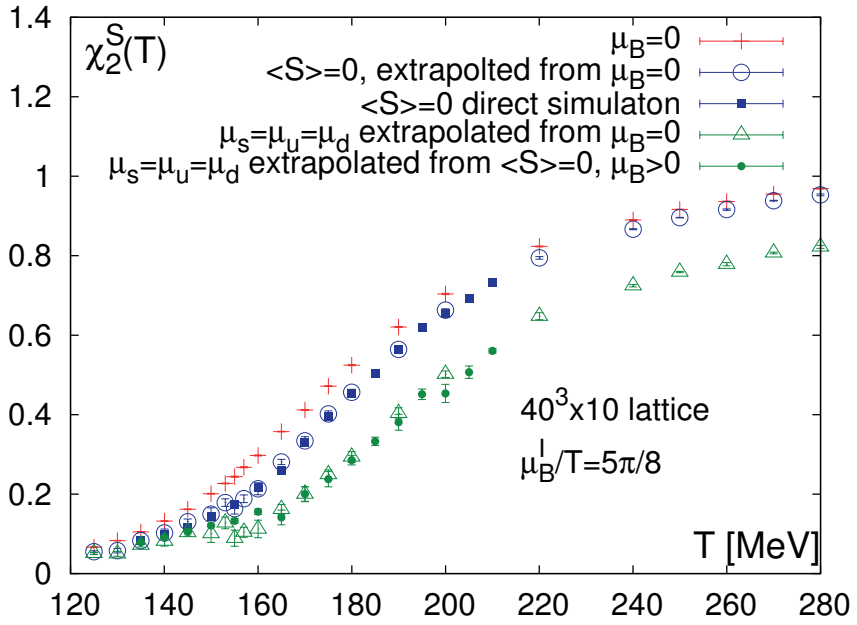

Figure 4.4: *An example of how different choices of simulation points influence the strange susceptibility [5]. The red data set shows χ_{SS} at zero chemical potential. The blue data is at the strangness neutral point. The values from extrapolation to $\frac{\mu_B}{T} = \mathrm{i}\frac{5}{8}\pi$ from $\mu_B = 0$ agree nicely. The green data is not at the strangeness neutral point but at $\mu_s = \mu_u = \mu_d$. Since we did no actual simulations with this setting both data sets shown here are extrapolated, though from different starting points.*

extrapolation to $\frac{\mu_B}{T} = \mathrm{i}\frac{5}{8}$ from $\mu_B = 0$ agree nicely. The green data is not at the strangeness neutral point but at $\mu_s = \mu_u = \mu_d$. Since we did no actual simulations with this setting both data sets shown here are extrapolated, though from different starting points. Also these two data sets agree nicely. However they differ significantly from the simulations at the strangeness neutral point.

4.2 The data

In this section we will describe which simulations were used for the analysis described below. However not all the data were used in each project, as the data were generated in a simulation effort over several years. Also in the analysis of the transition temperature (see section 4.3) higher values of μ_B change the shape of the fit to the observables, which does not allow for a combined fit as it was done here.

For the simulations we used a tree level Symanzik improved gauge action. The dynamical fermions were four times stout smeared staggered fermions [178]. The smearing parameter was $\rho = 0.125$. The simulations were performed with 2+1+1 flavours. The up and the down quark have degenerate masses that were together with the strange quark mass tuned in a way that the pion and the kaon mass divided by the pion decay constant are set to their physical value for every lattice spacing. The charm mass was set in a way that $\frac{m_c}{m_s} = 11.85$ as described

in [179]. The lattice spacing ranges between $a = 0.063$ fm and $a = 0.2$ fm. For every lattice spacing $Lm_\pi > 4$ is fulfilled in the zero temperature runs.

For the finite temperature and density simulations μ_B has to be smaller then $\mathrm{i}\pi T$ due to the Roberge-Weiss transition (see for example [180, 181, 182]). Our values for μ_B were chosen as

$$\mu_B^{(j)} = \mathrm{i}T\frac{j}{8}\pi \tag{4.35}$$

for $j \in \{0, 1, 2, 3, 4, 5, 6, 6.5, 7\}$. The value for μ_S is tuned in a way that the simulation is at the strangeness neutral point as described in section 4.1. For each value of μ_B we have simulations for sixteen temperatures between 135 MeV and 210 MeV. For the simulations with $j = 3$ to $j = 7$ and for $j = 0$ we have data on lattices with sizes $32^3 \times 8$, $40^3 \times 10$, $48^3 \times 12$ and $64^3 \times 16$. For $j = 1$ and $j = 2$ we only have data for $N_t = 8, 10$ and 12 lattices. This simulations were later not used in the analysis since they do not differ a lot from the $j = 0$ simulations. However they were needed to tune to the strangeness neutral point. For each set of parameters we generated between 10000 and 20000 Hybrid Monte Carlo updates for the finite density configurations and 5 to 10 times more statistics for the $\mu_B = 0$ runs. For $N_t = 8, 10$ and 12 every 5th configuration was analysed. For $N_t = 16$ we analysed every 10th configuration. The higher statistics for $\mu_B = 0$ allows us to check which interpolating functions for each observables ensure a good fit.

4.3 The transition temperature

The most interesting region in the QCD phase diagram in the μ_B-T-plane is the transition region where hadronic matter is deconfined and becomes quark gluon plasma. On the lattice we can calculate the temperature where this deconfinement transition takes place. Since we already know that at $\mu_B = 0$ the transition is an analytic crossover, the temperature can vary for different observables. For this analysis we use the data described in section 4.2 from the runs with $\mu_B^{(j)} = \mathrm{i}T\frac{j\pi}{8}$ with $j \in \{0, 3, 4, 5, 6\}$. We work with three different observables $\chi_{\bar{\psi}\psi}$, $\langle\bar{\psi}\psi\rangle$ and χ_{SS} that are introduced in section 4.3.1. The first two observables have to be renormalized. To obtain an analytical formula for the shape of the observable $\mathbf{o}$ at every $\mu_B^{(j)}$ we make a fit $\mathbf{o}(T)$ in the temperature direction. To respect the correlation that is introduced in the renormalizaition procedure this will be a combined fit for all $\mu_B^{(j)}$ at a fixed value for N_t. From the analytical form we can determine the transition temperature that we define either as the location of the maximum of a peak or as the location of the inflection point of a sigmoid function. The next step is to identify the dependence on $\hat{\mu}_B^2 = \frac{\mu_B^2}{T^2}$ of the transition temperature. We do this with a linear fit which can describe the data of $\mu_B^{(0)}$, $\mu_B^{(3)}$, $\mu_B^{(4)}$ and $\mu_B^{(5)}$. If also $\mu_B^{(6)}$ is included in the analysis we need to use a second order fit. From this fit we can determine the curvature κ of the temperature $T_c(\mu_B)$ at $\mu_B = 0$ for which there are several other analysises to compare with, which will be done in section 4.3.7. We can of course also determine the transition temperature itself. Finally we calculate continuum extrapolated results. This can either be done in a continuum extrapolation of the results of the fit $T_c(\mu_B)$ or as a combined fit for the μ_B and N_t dependence.

For χ_{SS} we also use several data sets, extrapolated to different settings that we can analyse for comparison. We also attempt to gain the curvature κ by the Taylor coefficient method for our data at $\mu_B^{(0)}$.

4.3.1 The observables

In this analysis we will use three different observables: $\chi_{\bar{\psi}\psi}$, $\langle\bar{\psi}\psi\rangle$ and χ_{SS}. Of this three $\chi_{\bar{\psi}\psi}$ and $\langle\bar{\psi}\psi\rangle$ have to be renormalized by subtraction of the zero temperature data. $\chi_{\bar{\psi}\psi}$ has a the form of a peak, while $\langle\bar{\psi}\psi\rangle$ and χ_{SS} take the form of a sigmoid function. In the following we will describe how we gain an analytical description of the function $\mathbf{o}(T)$ from which we can extract the crossover temperature.

4.3.1.1 Analysing $\chi_{\bar{\psi}\psi}$

The main observable is the chiral susceptibility $\chi_{\bar{\psi}\psi}$ which is defined as [12, 13]

$$\chi_{\bar{\psi}\psi} = \frac{T}{V}\frac{\partial^2 \ln Z}{\partial m_q^2}. \tag{4.36}$$

It has to be renormalized by substracting the zero temperature data. Therefore we write for the renormalized chiral susceptibility $\chi^r_{\bar{\psi}\psi}$

$$\chi^r_{\bar{\psi}\psi} = \left(\chi_{\bar{\psi}\psi}(T,\beta) - \chi_{\bar{\psi}\psi}(0,\beta)\right)\frac{m_l^2}{a^2 m_\pi^4}. \tag{4.37}$$

For the renormalizaition we need to fit the zero temperature simulations. For this we us two different ansatzes. First the polynomial ansatz

$$\chi_{\bar{\psi}\psi}(0,\beta) = \sum_{k=0}^{6} A_k \beta^k \tag{4.38}$$

and second an ansatz containing negative powers of β

$$\chi_{\bar{\psi}\psi}(0,\beta) = \sum_{k=-2}^{2} A_k \beta^k. \tag{4.39}$$

With the zero temperature data fitted we can calculate $\chi^r_{\bar{\psi}\psi}$. It shows the form of a peak. For fitting the data points we use again two different ansatzes:

$$\chi^r_{\bar{\psi}\psi}(T) = \begin{cases} C + A^2(\hat{\mu}_B)\left(1 + W^2(\hat{\mu}_B)(T - T_c(\hat{\mu}_B))^2\right)^{\alpha/2} & \text{for } T \le T_c \\ C + A^2(\hat{\mu}_B)\left(1 + b^2 W^2(\hat{\mu}_B)(T - T_c(\hat{\mu}_B))^2\right)^{\alpha/2} & \text{for } T > T_c \end{cases} \tag{4.40}$$

and

$$\chi^r_{\bar{\psi}\psi}(T) = C + \frac{A(\hat{\mu}_B)}{1 + W^2(\hat{\mu}_B)(T - T_c(\hat{\mu}_B))^2 + a_3 W^3(\hat{\mu}_B)(T - T_c(\hat{\mu}_B))^3} \tag{4.41}$$

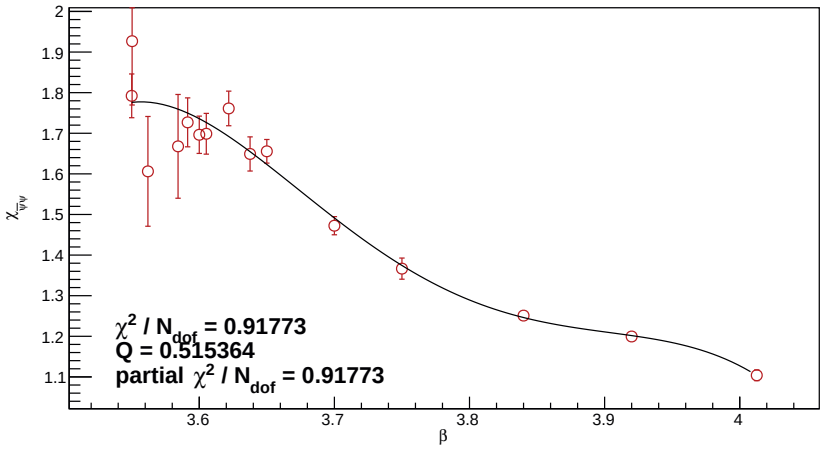

Figure 4.5: *The fit to the zero temperature values* $\chi_{\bar{\psi}\psi}(0, \beta)$.

where all fitting parameters depend on N_t. The fit of (4.40) or (4.41) to the data for each value of $\mu_B^{(j)}$ and the fit of (4.38) or (4.39) are performed simultaneously to account for the correlation of the renormalized $\chi^r_{\bar{\psi}\psi}$ with the zero temperature fit. The result for the zero temperature fit is shown in figure 4.5 and an example for the finite temperature fits is shown in figure 4.6. Since the fit functions only work well for the range of the peak in all finite temperature fits we have only used data points with $\chi_{\bar{\psi}\psi}(T, \beta) > c$ to remove the tails of the peak. We choose $c \in \{0.03, 0.04, 0.05\}$. This observable is best suited to determine the transition temperature, because T_c can be easily defined and read of as the maximum of the peak. The other observables show the form of a sigmoid function, where the transition temperature would be the point of inflection. Since this is more difficult to fit it leads to larger errors on T_c, but the distance between the curves and the relative change in T_c can still be determined fairly well. For the figure 4.6 the data are rescaled and shifted in a way that all data points lie on the curve of $\mu_B^{(0)}$.

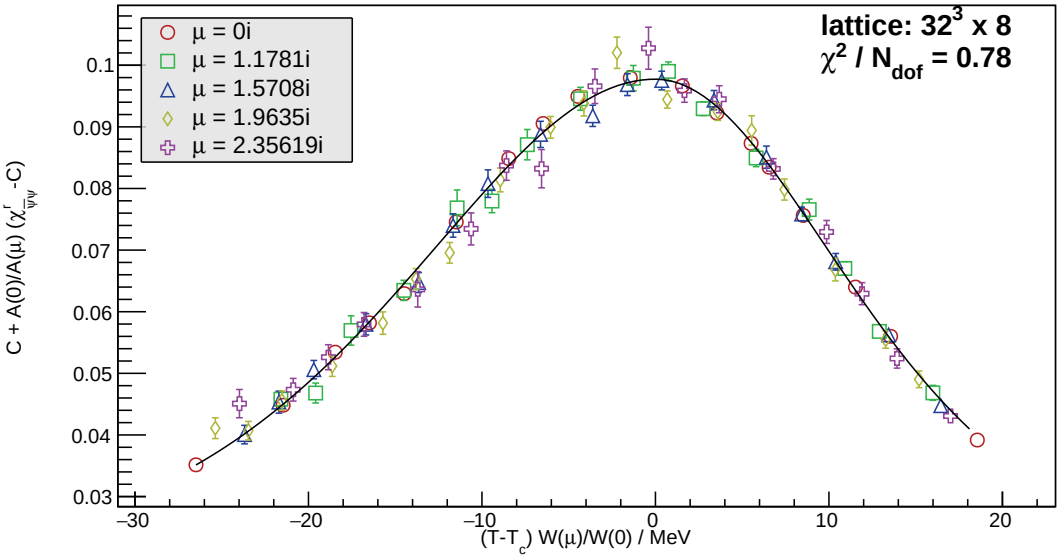

(a) $32^3 \times 8$

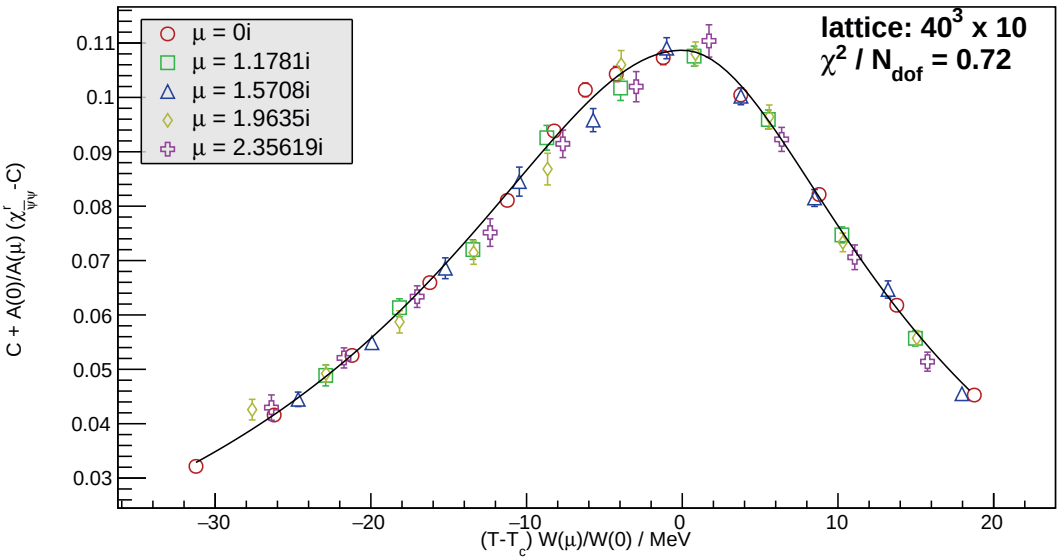

(b) $40^3 \times 10$

Figure 4.6: *The fits to the finite temperature values* $\chi^r_{\bar{\psi}\psi}(T)$ *using eqn. (4.40).*

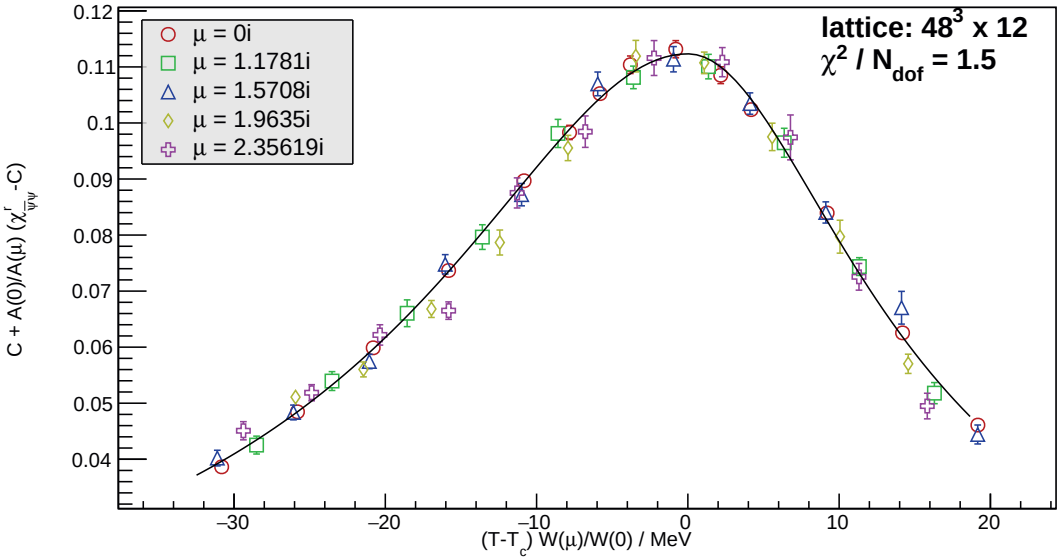

(c) $48^3 \times 12$

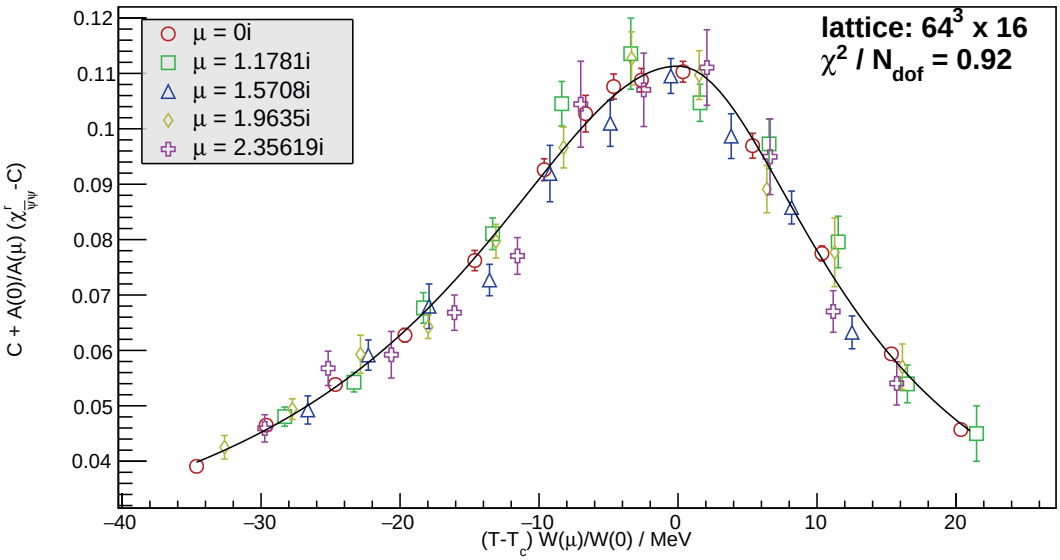

(d) $64^3 \times 16$

Figure 4.6: *The fits to the finite temperature values* $\chi^r_{\bar{\psi}\psi}(T)$ *using eqn. (4.40).*

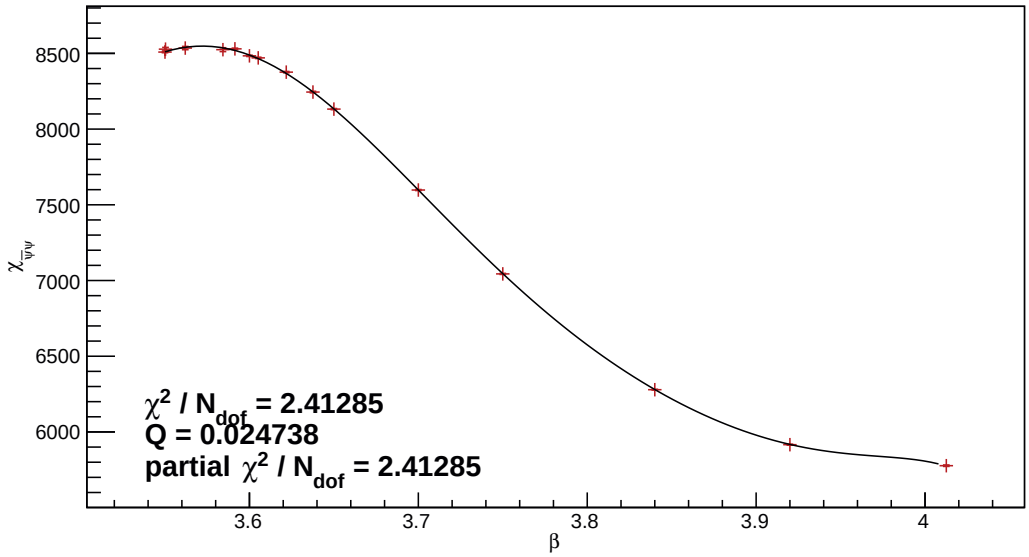

Figure 4.7: *The fit to the zero temperature values* $\bar{\psi}\psi(0,\beta)$.

4.3.1.2 Analysing $\bar{\psi}\psi$

The next observable is the chiral condensate $\bar{\psi}\psi$. Like the susceptibility it has to be renormalized by substracting the zero temperature values and is defined as [13]

$$\bar{\psi}\psi^r = -\left(\langle\bar{\psi}\psi\rangle(T,\beta) - \langle\bar{\psi}\psi\rangle(0,\beta)\right)\frac{m_l}{a^3 m_\pi^4}. \tag{4.42}$$

For fitting the zero temperature data we use the polynomial ansatz

$$\chi_{\bar{\psi}\psi}(0,\beta) = \sum_{k=0}^{K} A_k \beta^k \tag{4.43}$$

with $K \in \{6,7\}$.

$\bar{\psi}\psi^r$ shows a sigmoid like behaviour. For fitting it we use the two different ansatzes:

$$\bar{\psi}\psi^r(\mu,T) = A(\mu)\left(1 + B\tanh\left[C\left(T - T_c(\mu)\right)\right] + D\left(T - T_c(\mu)\right)\right) \tag{4.44}$$

and

$$\bar{\psi}\psi^r(\mu,T) = A(\mu)\left(1 + B\arctan\left[C\left(T - T_c(\mu)\right)\right] + D\left(T - T_c(\mu)\right)\right) \tag{4.45}$$

where again all fit parameters depend on N_t.

The fit (4.44) or (4.45) for each value of μ and the fit (4.43) to the zero temperature data are performed in the same manner as for $\chi^r_{\bar{\psi}\psi}$. The result for the zero temperature fit is shown in figure 4.7 and an example for the finite temperature fits is shown in figure 4.8. A fit window is chosen in a way that $a < \bar{\psi}\psi^r < b$ with $a \in \{0.25, 0.3\}$ and $b \in \{0.7, 0.75\}$.

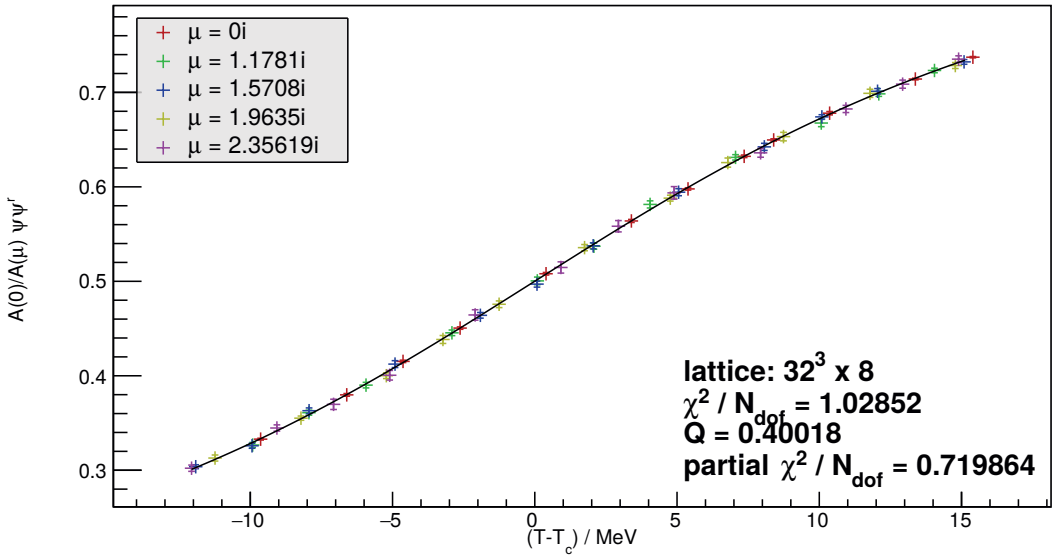

(a) $32^3 \times 8$

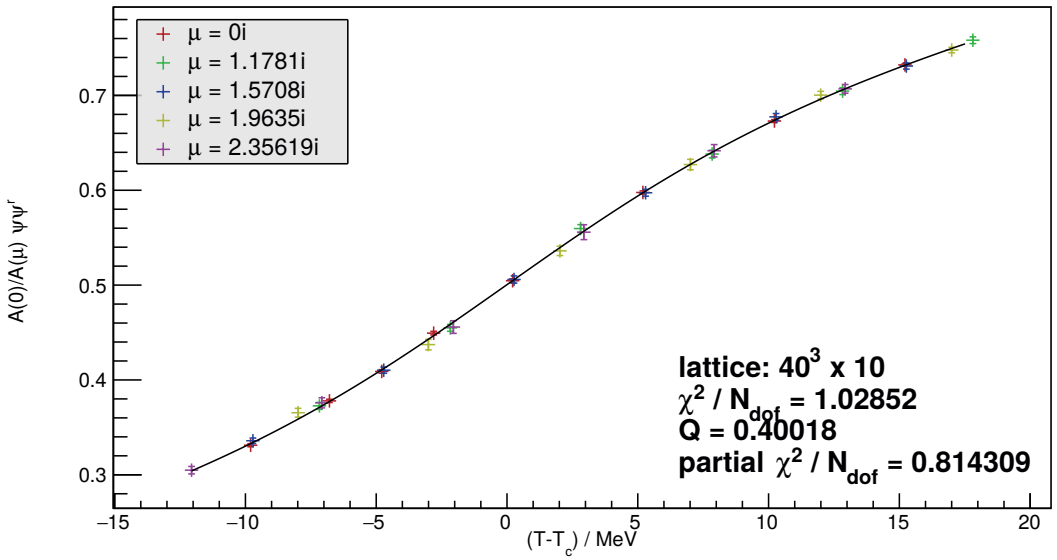

(b) $40^3 \times 10$

Figure 4.8: *The fits to the finite temperature values $\bar{\psi}\psi^r(T)$ using eqn. (4.45) shifted by the respective T_c and rescaled.*

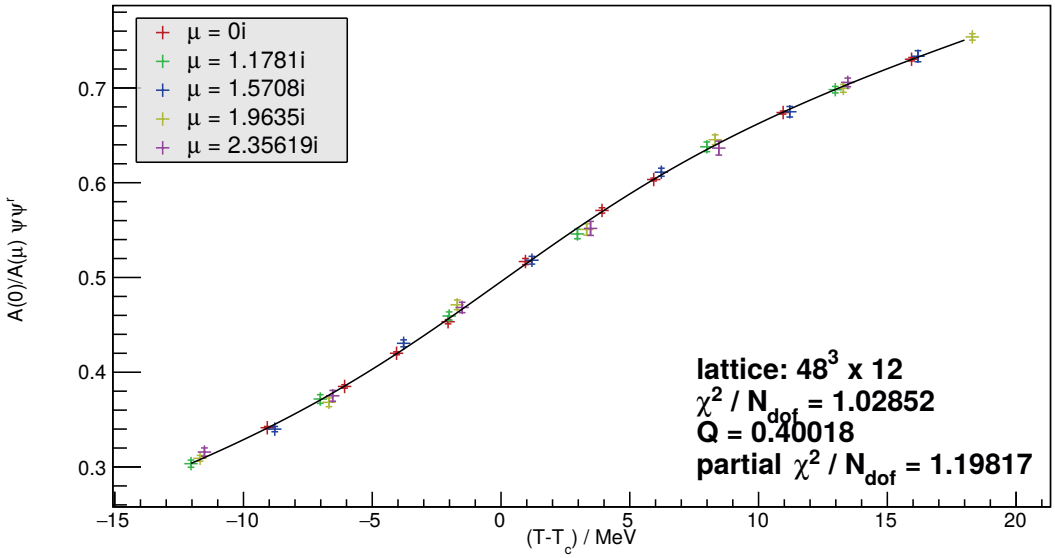

(c) $48^3 \times 12$

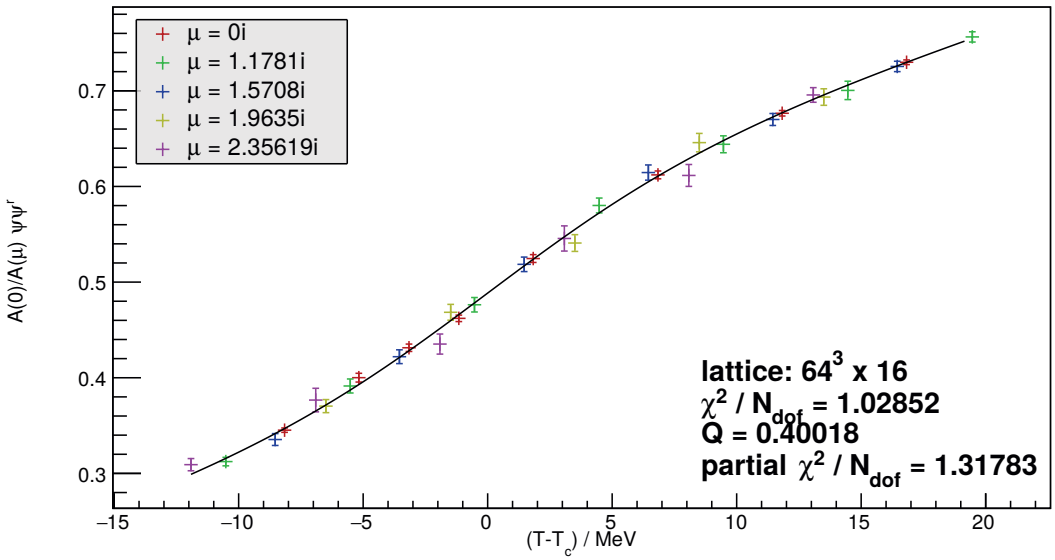

(d) $64^3 \times 16$

Figure 4.8: *The fits to the finite temperature values $\bar{\psi}\psi^r(T)$ using eqn. (4.45) shifted by the respective T_c and rescaled.*

4.3.1.3 Analysing χ_{SS}

The strange susceptibility is defined as

$$\chi_{SS} = \frac{\partial^2 \log Z}{\partial \mu_S^2}. \tag{4.46}$$

The calculation of the different versions of χ_{SS} that are described below was done as described in section 4.1. For this analysis the data was supplied with ten Jack-Knife samples and the resulting errors. Since this analysis relies on the Bootstrap method and needs more then ten samples to calculate the correlation matrices for the extrapolation fits later in the analysis, we assumed that the Jack-Knife error is correct and that Bootstrap samples for the independent ensembles have a Gaussian distribution. Then the values for the Bootstrap samples are chosen as random values from a one dimensional Gaussian distribution where the mean value is the central value for χ_{SS} and the width is the jack knife error. An introduction to the Jack-Knife and the Bootstrap method can be found for example in [27].

A great advantage of the strange susceptibility is that it does not need to to be renormalized. Therefor the finite temperature fits for χ_{SS} can be performed independently for every N_t. χ_{SS} shows a similar behaviour as $\bar{\psi}\psi$ and is therefore fitted with the same ansatzes as shown in equation (4.44) and (4.45). The fit window is chosen in a way that $a < \chi_{SS} < c(N_t)b$ with $a \in \{0.15, 0.2, 0.25, 0.3\}$ and $b \in \{0.6, 0.65, 0.7, 0.75\}$. $c(N_t)$ is the treelevel correction given as

$$c(N_t) = \begin{cases} 1.28037 & \text{for } N_t = 8 \\ 1.15739 & \text{for } N_t = 10 \\ 1.09721 & \text{for } N_t = 12 \\ 1.0659 & \text{for } N_t = 16 \end{cases}. \tag{4.47}$$

We analysed several different calculation of the strange susceptibility:

- χ_{SS}: The chiral susceptibility simulated at the strangeness neutral point where $\langle n_S = 0 \rangle$ and $\langle n_Q \rangle = 0.5 \langle n_B \rangle$.
- χ_{SS}^{E}: The chiral susceptibility simulated at the strangeness neutral point with a small extrapolation in $\langle n_S \rangle$, so that with better prezision $\langle n_S \rangle = 0$ and $\langle n_Q \rangle = 0.4 \langle n_B \rangle$.
- χ_{SS}^{extra}: The same as χ_{SS}, but only simulated at $\mu = 0$ and than extrapolated via a Taylor expansion to imaginary μ.
- $\chi_{SS}^{E,\text{extra}}$: The same as χ_{SS}^{E}, but only simulated at $\mu = 0$ and than extrapolated via a Taylor expansion to imaginary μ.
- $\chi_{SS}^{l,\text{extra}}$: The chiral susceptibility extrapolated from $\mu_s = 0$ for simulations with $\mu_S = 0$.
- $\chi_{SS}^{b,\text{extra}}$: The chiral susceptibility extrapolated from $\mu_s = 0$ for simulations with $\mu_u = \mu_d = \mu_s$.

The fits for $\chi_{SS}^{E,\text{extra}}$ are shown in figure 4.9.

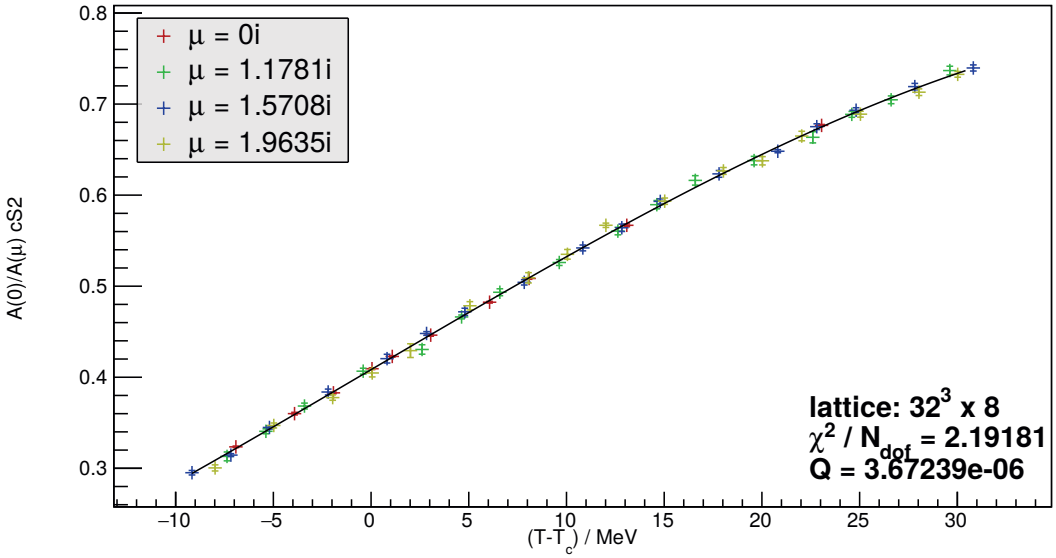

(a) $32^3 \times 8$

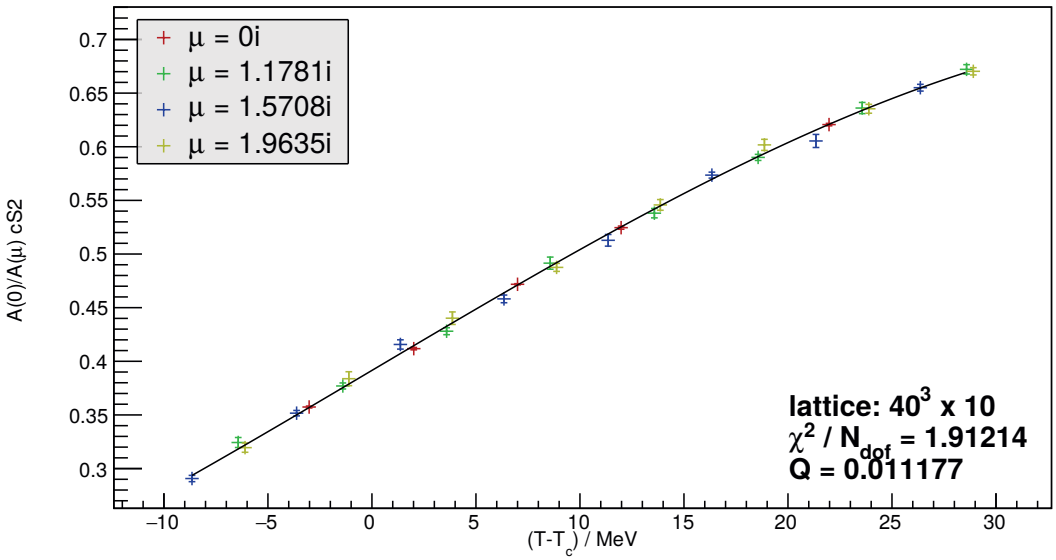

(b) $40^3 \times 10$

Figure 4.9: *The fits to the finite temperature values χ_{SS} using eqn. (4.44). The data were shifted by the respective T_c and rescaled.*

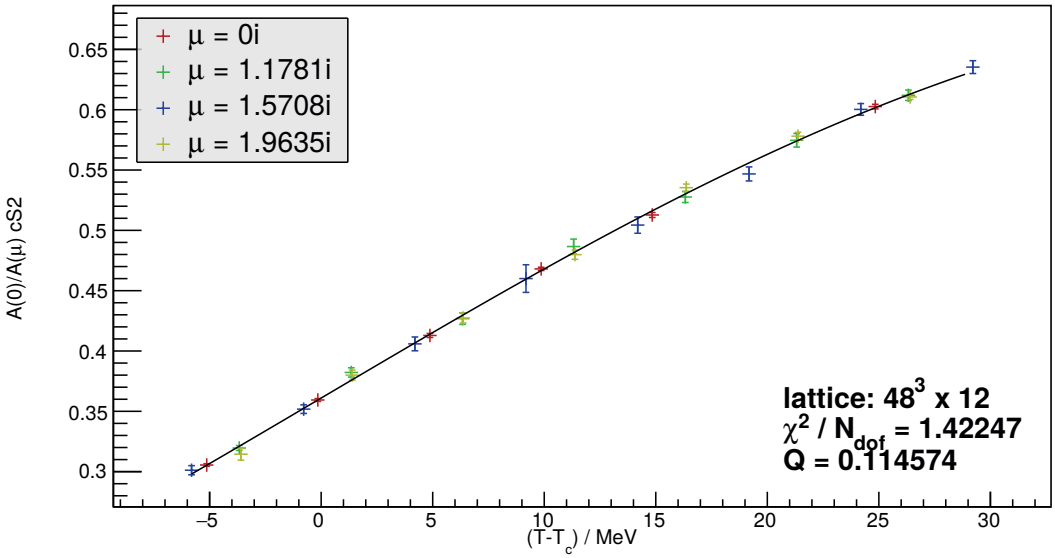

(c) $48^3 \times 12$

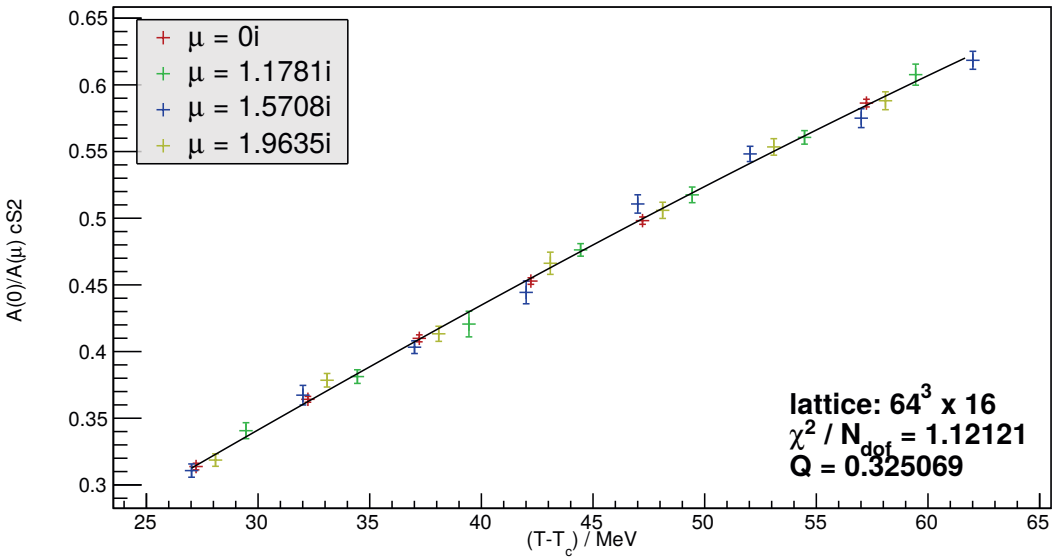

(d) $64^3 \times 16$

Figure 4.9: *The fits to the finite temperature values χ_{SS} using eqn. (4.44). The data were shifted by the respective T_c and rescaled.*

4.3.2 Curvature Fit

The curvature κ is defined via the equation

$$\frac{T_c(\mu_B)}{T_c(0)} = 1 - \kappa \left(\frac{\mu_B}{T_c}\right)^2 - \frac{1}{2}\lambda \left(\frac{\mu_B}{T_c}\right)^4 + \mathcal{O}(\mu_B^6). \tag{4.48}$$

We take the fitted T_c values for each lattices size from the fit described in the previous section. We then compute $T_c(\mu_B)/T_c(0)$ so that correlations of $T_c(\mu_B)$ and $T_c(0)$ cancel in the error estimation of the data points. Afterwards we fit the data to equation (4.48) for each lattice size separately. Note that the data point at $\mu_B = 0$ is not shown, as it is per definition exactly $(0, 1)$. Each fit takes into account the full correlation matrix between the data points.

To be able to fit the data with a linear ansatz we do not take into account the data for the largest value of μ. Exemplary results are shown in figure 4.10.

To fit the last value of μ we have to introduce an $\mathcal{O}(\mu_B^4)$ contribution in equation (4.48). We have several possibilties how to add this second order term. We will call

$$\frac{T_c(\mu_B)}{T_c(0)} = C_i\left(\frac{\mu_B^2}{T_c^2}\right). \tag{4.49}$$

We then use

$$C_1(x) = 1 + ax + bx^2 \tag{4.50}$$

$$C_2(x) = \frac{1+ax}{1+bx} \tag{4.51}$$

$$C_3(x) = \frac{1}{1+ax+bx^2}. \tag{4.52}$$

We then can extract κ and λ as

$$\kappa = \begin{cases} -a & \text{for } C_1 \\ b-a & \text{for } C_2 \\ a & \text{for } C_3 \end{cases} \tag{4.53}$$

$$\lambda = \begin{cases} -\frac{1}{2}b & \text{for } C_1 \\ ab - b^2 & \text{for } C_2 \\ b - a^2 & \text{for } C_3 \end{cases} \tag{4.54}$$

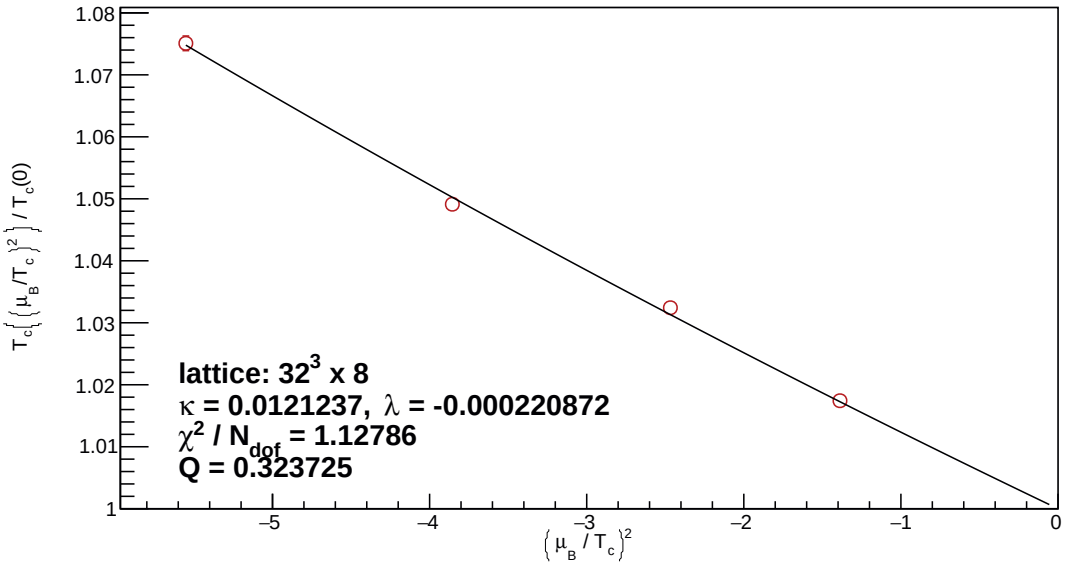

(a) $32^3 \times 8$

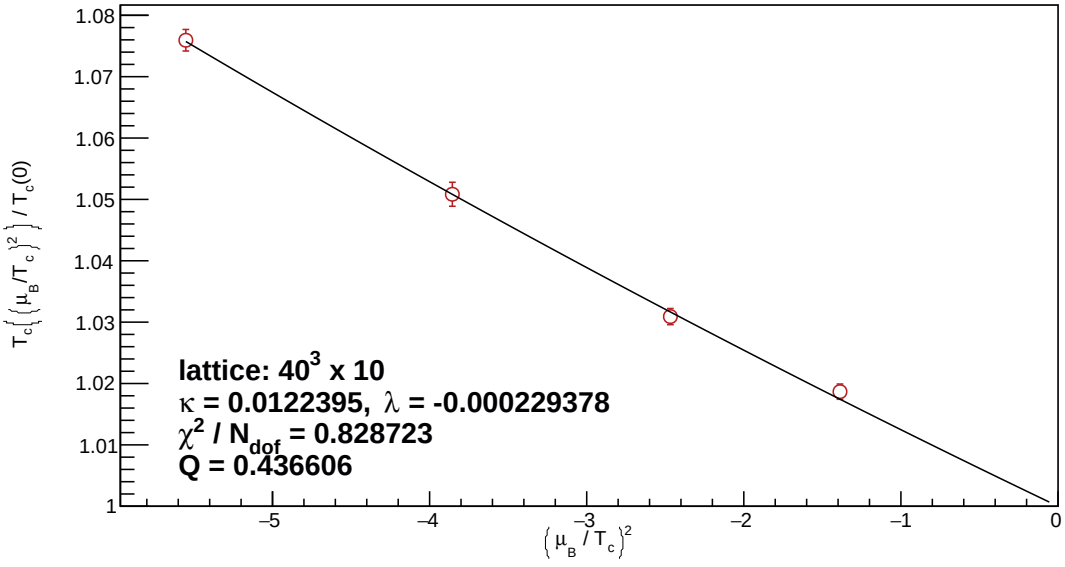

(b) $40^3 \times 10$

Figure 4.10: *The fits to extract κ via eqn. (4.52).*

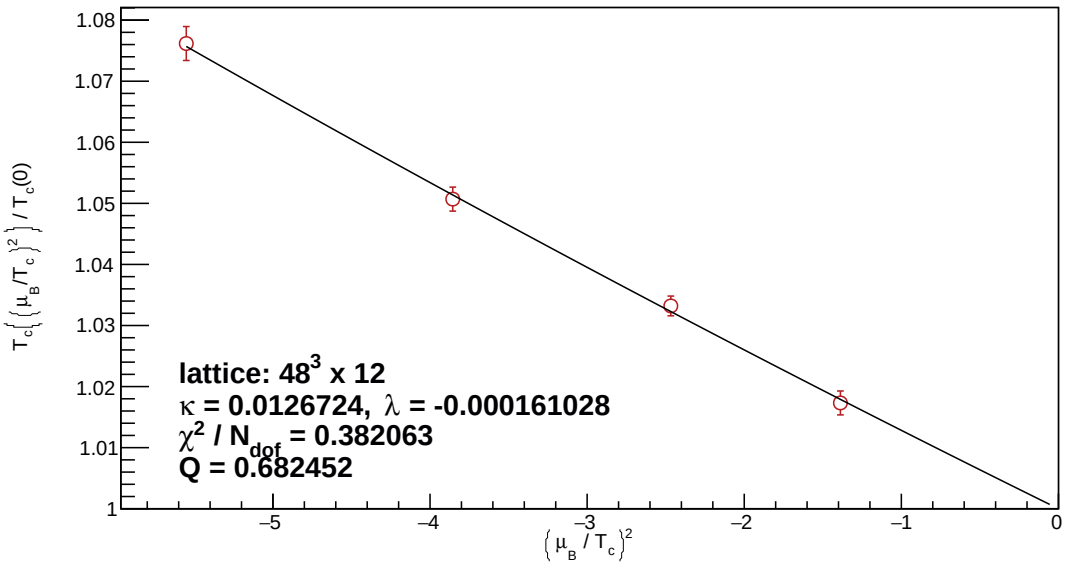

(c) $48^3 \times 12$

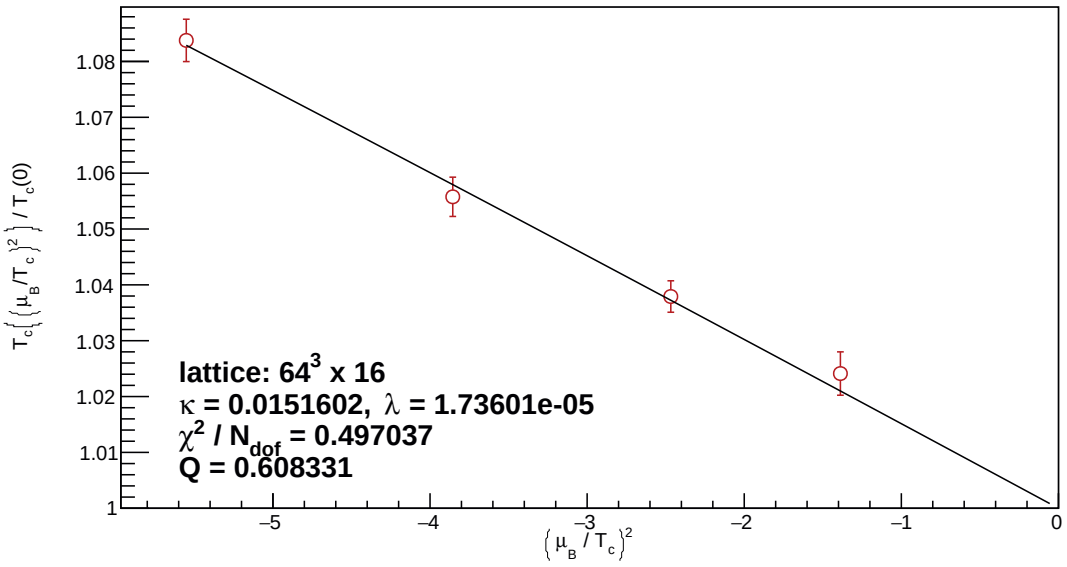

(d) $64^3 \times 16$

Figure 4.10: *The fits to extract κ via eqn. (4.52).*

4.3.3 Continuum extrapolation

In the scaling region the continuum extrapolation can be parameterized as

$$\kappa = \kappa^{\text{cont}} + A\left(\frac{1}{N_t}\right)^2. \tag{4.55}$$

We use the result from the fit described in the previous section and perform a correlated fit. The results for the continuum fit for κ extracted from $\bar{\psi}\psi$ can be seen in figure 4.11. During the analysis it turned out that even though it looks like the data points from $N_t = 8, 10, 12$ lie on a straight line (figure 4.11a) and therefore are in the scaling regime, this assumption turns out to be wrong when the data point of $N_t = 16$ is added in figure 4.11b. As a consequence in all further analysises we only use data from $Nt = 10, 12, 16$. The resulting continuum extrapolation can be seen in figure 4.11c.

4.3.4 Combined continuum extrapolation and curvature fit

Instead of performing the fit of the curvature and the continuum extrapolation seperatly it is possible to combine the fits. If we do that we fit the data for a first order curvature fit with the function:

$$\frac{T_c(\mu_B)}{T_c(0)} = 1 - \left(\kappa_c + c_1\frac{1}{N_t^2}\right)\left(\frac{\mu_B}{T_c}\right)^2. \tag{4.56}$$

For the second order curvature fit we use the fit functions

$$C_1(x) = 1 + \left(a + c_1\frac{1}{N_t^2}\right)x + \left(b + c_2\frac{1}{N_t^2}\right)x^2 \tag{4.57}$$

$$C_2(x) = \frac{1 + \left(a + c_1\frac{1}{N_t^2}\right)x}{1 + \left(b + c_2\frac{1}{N_t^2}\right)x} \tag{4.58}$$

$$C_3(x) = \frac{1}{1 + \left(a + c_1\frac{1}{N_t^2}\right)x + \left(b + c_2\frac{1}{N_t^2}\right)x^2}. \tag{4.59}$$

The combined fit describes the data with less parameters then the separate fits. For the first order fit in μ_B there are two parameters in the combined fit, while for the separate fit there is one parameter for every N_t and an additional two for the continuum slope resulting in a total number of five parameters. For the second order fit there are two parameters in every μ_B fit, giving a total number of eight parameters compared to three in the combined fit. Also this gives us another method for the analysis that we can use to estimate the systematic error.

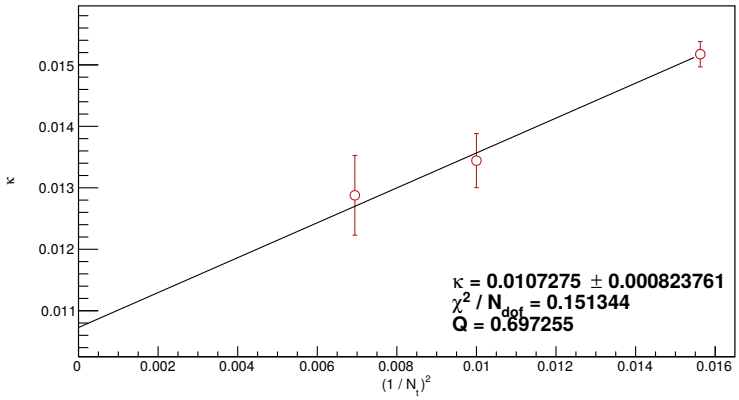

(a) *Continuum extrapolation with* $Nt = 8, 10, 12$

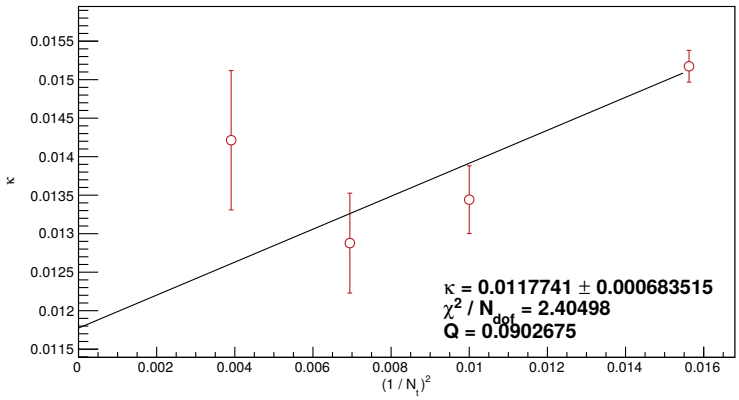

(b) *Continuum extrapolation with* $Nt = 8, 10, 12, 16$

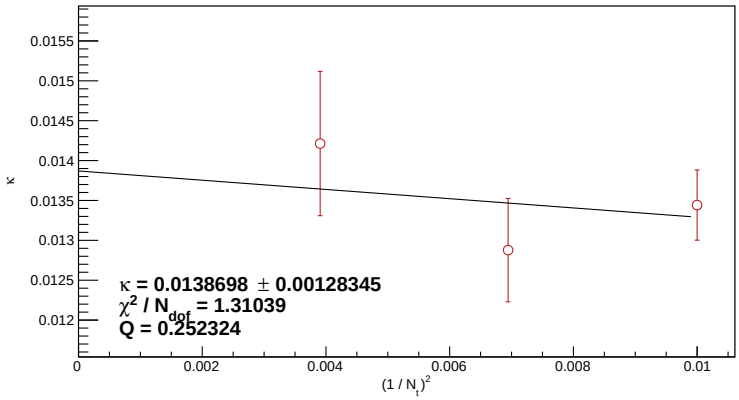

(c) *Continuum extrapolation with* $Nt = 10, 12, 16$

Figure 4.11: *The continuum extrapolations of the curvature parameter* κ.

Table 4.1: *Results for the curvature of the transition line in the QCD phase diagram.*

observable	κ
$\chi_{\bar{\psi}\psi}$	$0.0158 \pm 0.00067 + 0.00013 - 0.00023$
$\bar{\psi}\psi$	$0.0138 \pm 0.0006 + 0.0005 - 0.0004$
c2S	$0.0149 \pm 0.0006 + 0.0006 - 0.001$
c2SE	$0.0149 \pm 0.0006 + 0.0005 - 0.0008$

4.3.5 Results

To determine the systematical error we repeat our analysis with different parameters and look at the histogram. As mean value we use the median. The systematical error is determined in a way that 68% of the results of the different analyses fall within the error band. This so called *histogram method* was introduced in [16]. The statistical error is the bootstrap error of the median of every bootstrap sample. The resulting histograms can be seen in figure 4.12 to 4.14.

In the analysis for $\chi_{\bar{\psi}\psi}$ we have two methods of scale setting, two fits for $T > 0$, two fits for the zero temperature data, three different fit windows and either a combined or a separated fit for the μ_B and N_t dependence. This gives a total of $2 \cdot 2 \cdot 2 \cdot 3 \cdot 2 = 48$ analyses. For the chiral condensate we have four fit windows and otherwise the same analyses, given a total of $2^5 = 64$ analyses. For χ_{SS} there are no zero temperature fits and otherwise the same analyses, adding up to a total number of 32.

The resulting values are given in 4.1. From the table and even easier from the histograms in figure 4.12 it can be seen that the values for all three observables lay quite close together even if it is not nessesarry that they give the same temperature, since the transition is a crossover. Since they are so close together, they can be joint into a single quantity, giving an overall value for the curvature of

$$\kappa = 0.0149 \pm 0.0021. \tag{4.60}$$

From figure 4.12 it can also be seen that between the strange susceptibility at $\langle n_Q \rangle = 0.5 \langle n_B \rangle$ (χ_{SS}) and at $\langle n_Q \rangle = 0.4 \langle n_B \rangle$ (χ^E_{SS}) there is no difference in the mean value. Any effect coming from the isospin asymmetry vanishes within our error. Therefore it is not necessary to do this extrapolation for the other two observables.

Figure 4.13 shows the results for the different analyses where the data was obtained by Taylor expansion from the $\mu_B = 0$ data. Since we have significantly less statistics than for the other analyses, the errors are quite large and we can not make a definite statement about the differences between the observables. Therefore in figure 4.14 we show the results from our analysis on an $N_t = 10$ lattice, without continuum extrapolation. Of course this excludes the analyses from the combined fit. Now in figure 4.14 we can see that the data from the analysis with Taylor expansion and the actual simulations are in agreement within the errors, even if the data from the Taylor expansion tends a bit to the lower end (lower two histograms). Also we can see that the data where μ_s is set to zero and the result for data that has been tuned to the strangeness neutral point agree quite well. If instead of μ_s, μ_S is set to zero the result however differs significantly (upper two histograms).

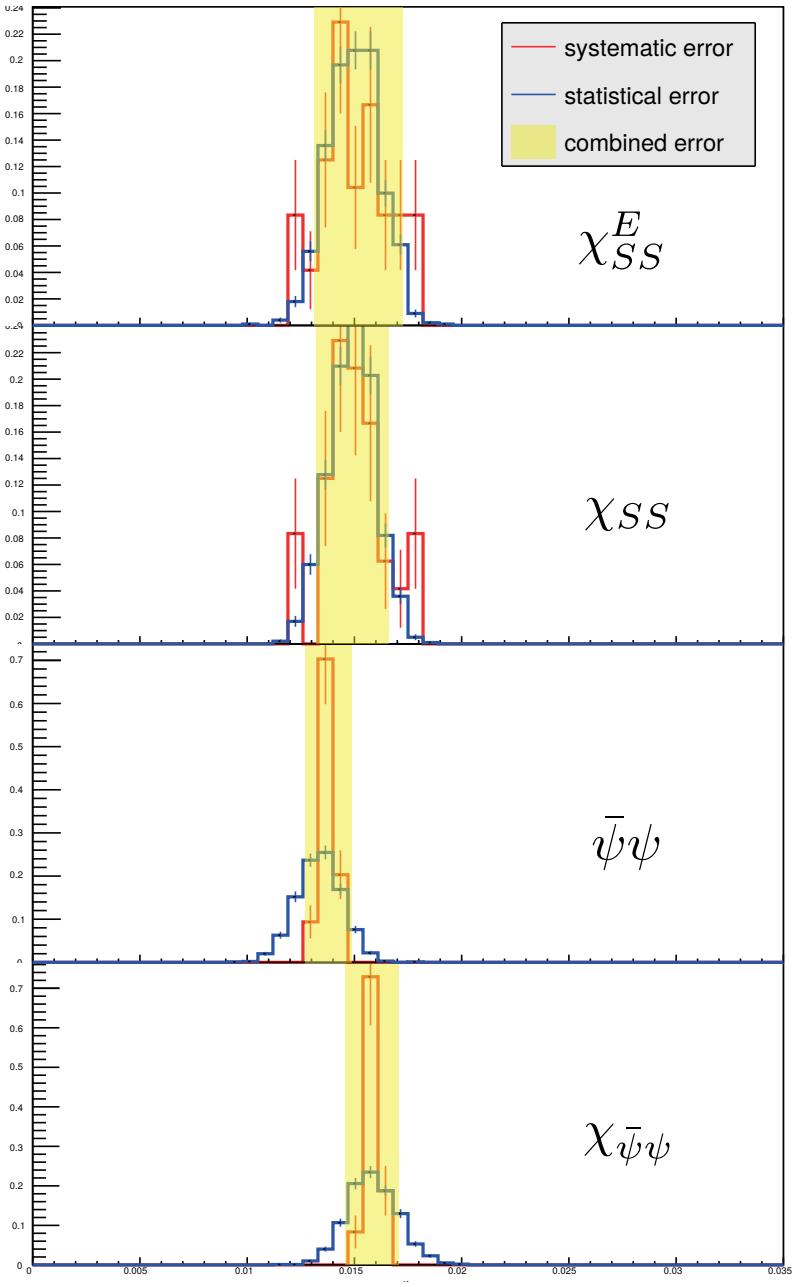

Figure 4.12: *The resulting histograms for κ from the different observables.*

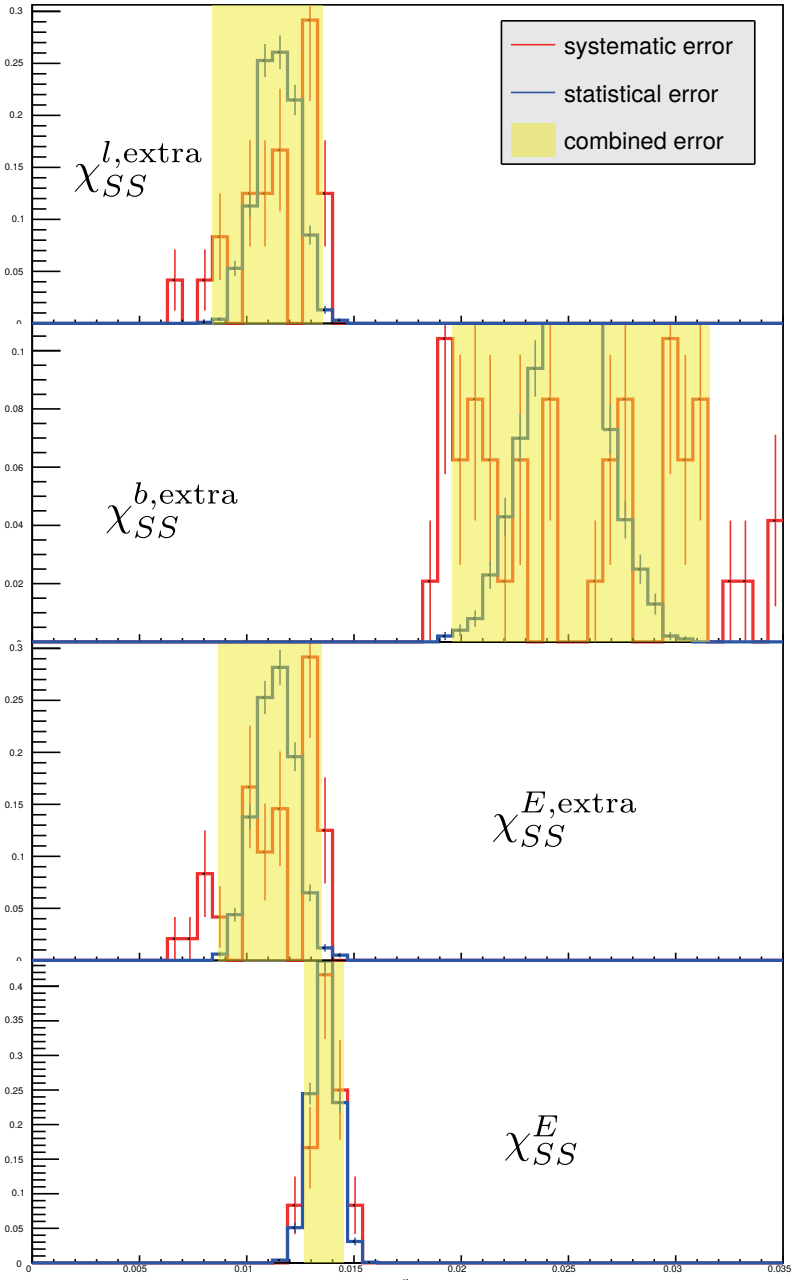

Figure 4.13: *The resulting histograms for κ from the different settings of χ_{SS}.*

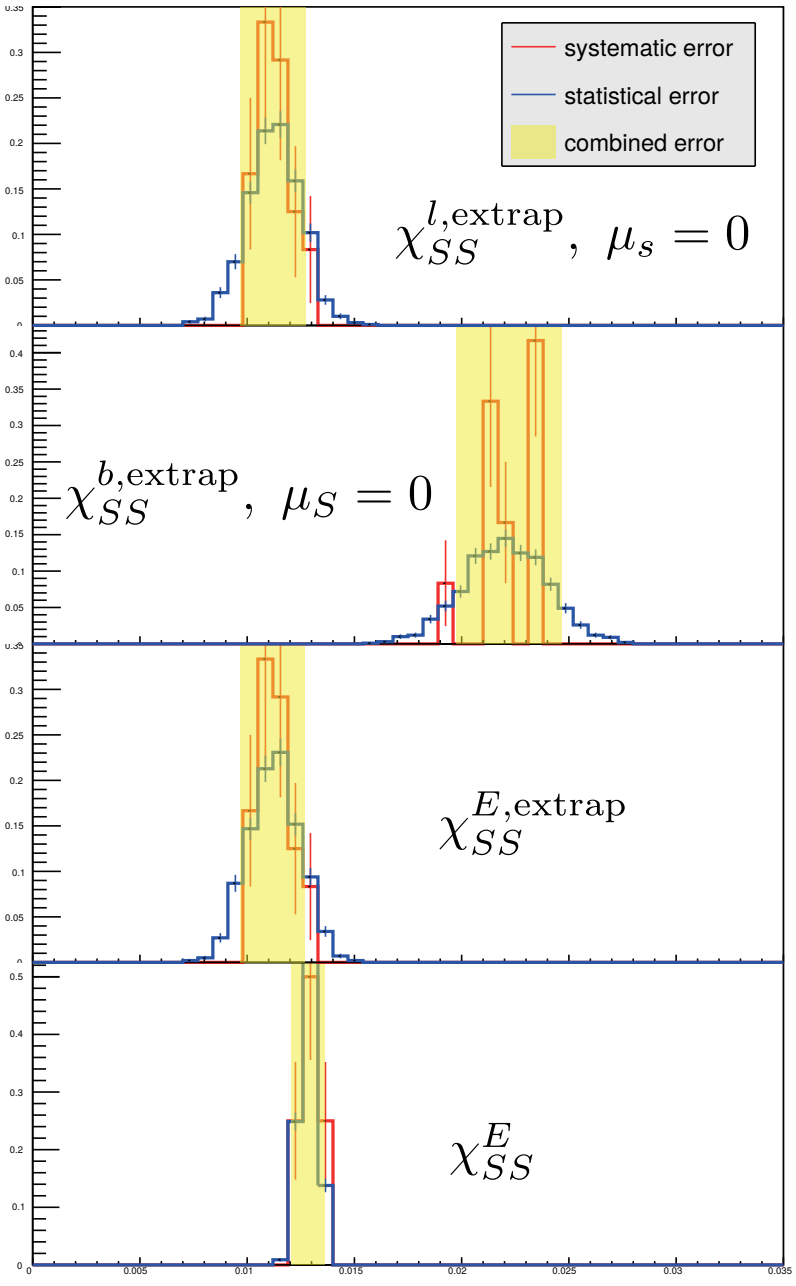

Figure 4.14: *The resulting histograms for κ from the different settings of χ_{SS} on the $N_t = 10$ lattice.*

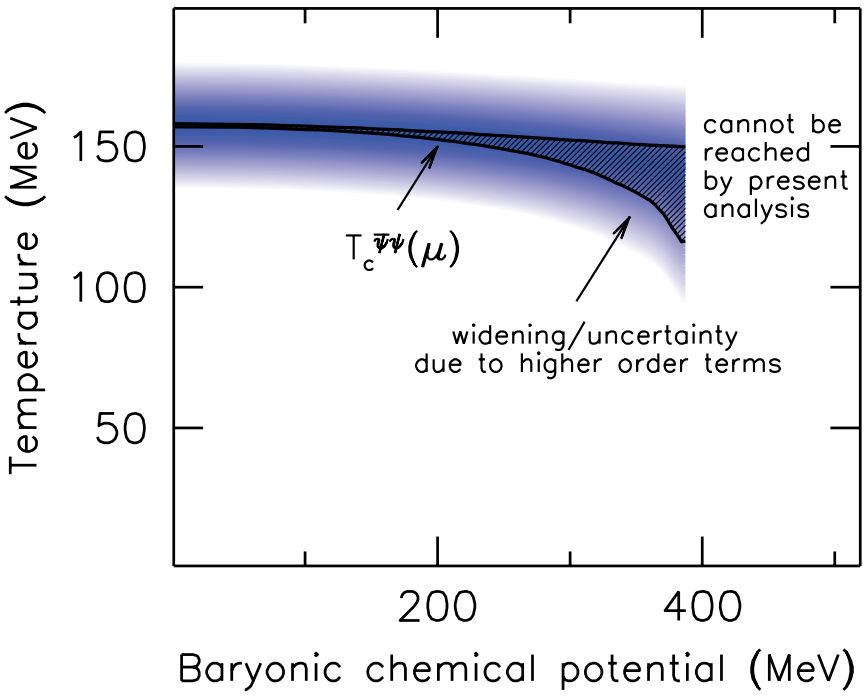

Figure 4.15: *The extrapolation of T_c from $\bar{\psi}\psi$*

4.3.6 Extrapolating T_c

To determine the critical temperature we will use the functions for the curve fit which were described in section 4.3.2 and 4.3.4. We take the continuum extrapolated parameters a and b (or only a for first order fits) and solve the equation

$$\frac{T_c(\mu_B)}{T_c(0)} = C_i \left(\frac{\mu_B^2}{T_c^2}\right) \tag{4.61}$$

numercially for $T_c(\mu_B)$. The value of $T_c(0)$ we obtain from the fits of $\bar{\psi}\psi$ (see section 4.3.1.2) which we extrapolate in the same manner as described in section 4.3.2 for κ and λ. This will be done for approximately 100 values of μ_B^2. For each of this points we calculate the histogram as described in section 4.3.5. We calculate the combined error for each point by adding systematic and statistical error quadratically. The result for $\bar{\psi}\psi$ can be seen in figure 4.15. In that figure the dark line shows the result and the error that comes from the analysis of $\bar{\psi}\psi$. The light blue shade behind the curve shows an approximation for the spread from the different observables. The widening of the curve comes from the higher order terms and the

statistical errors. It gives us an estimate of how far we can extrapolate, always assuming that we do not encounter the critical endpoint. Beyond a baryon chemical potential of about 400 MeV the error grows extremely large.

On should note that the extrapolation in the region of finite chemical baryon potential by the method of analytical continuation only works as long as there is no critical endpoint. As described in section 3.3 one expects a critical endpoint somewhere on the transition line. Since this endpoint is a non-analyticity we cannot detect it by analytical continuation independent of the error on our transition line. It has to be calculated or measured by different methods and our extrapolation is only valid up to that point. Since the critical endpoint has not been found yet, we show our curve up to a point where the error increase drastically.

4.3.7 Other results

At first we want to discuss how well we agree with other determinations for the curvature κ. In figure 4.16 there is an overview over the available continuum extrapolated lattice results. The first two data points by Bellwied et al. [5] are the ones obtained from the analyses described above. The next point bei Cea et al. [183, 184] is from an analysis with the HISQ gauge action and staggered fermions on lattices with $N_t = 6, 8, 10$ and 12 by means of analytical continuation from imaginary chemical potential. The next group of points by Bonati et al. [185, 186, 187] are the results of another analysis with simulations at imaginary chemical potential. The simulations were done with a Symanizik improved gauge action and staggered fermions on $N_t = 6, 8, 10$ and 12 lattices. All this points that were obtained from a similar analysis agree within the error bars.

The red points on the other hand are obtained from the Taylor expansion method. This means that instead of using simulations at imaginary chemical potential one calculated derivatives of the observables with respect to μ_B at $\mu_B = 0$. For example the pressure can be written as [188]

$$\frac{P}{T^4} = \sum_{i,j,k=0}^{\infty} \frac{1}{i!j!k!} \chi_{ijk}^{BQS} \left(\frac{\mu_B}{T}\right)^i \left(\frac{\mu_Q}{T}\right)^j \left(\frac{\mu_S}{T}\right)^k \tag{4.62}$$

with with $X = B, Q, S$ and

$$\chi_n^X = \frac{\partial^n \left(\frac{P}{T^4}\right)}{\partial \left(\frac{\mu_X}{T}\right)^n}. \tag{4.63}$$

The χ_n^X can be calculated on $\mu_B = 0$ simulations. This gives the Taylor coefficients that can be used to analytical continue the observable to positive μ_B^2 as well. The point of Kaczmarek et al. [102] was calculated from simulations with the p4-action on $N_t = 4$ and 8 lattices. Also an extrapolation in the quark masses had to be performed. The points by Endrődi et al. [189] are obtained from simulations with the Symanzik improved gauge action and staggered fermions on $N_t = 6, 8$, and 10 lattices.

The values for κ from the Taylor expansion method and from the simulations at imaginary chemical Potential do not agree within error. However in both of the analyses from the Taylor expansion method only statistical uncertainties are provided. Therefore the errorbars should be increased by the systematic errors. Also the lattices are smaller than the ones used in the

newer analysises by the imaginary μ_B simulations. However the *Quark confinement and the hadron spectrum* conference 2016 preliminary results for the equation of state from the Taylor expansion method were presented [188]. Therefore we can hope for up to date results on the curvature soon.

Besides other lattice results, we can try to compare to data from other sources. In figure 4.17 we plot our data from figure 4.15 together with the freeze-out points from experiments [190, 191, 192, 193, 194] and a calculation done by the Dyson-Schwinger equation [195, 196] that also gives an estimate for the critical endpoint. Since it is assumed that the chemical freeze-out that can be measured by experiments is lower than the deconfinement transition it is a little surprising that some points are above our curve. However the experimental values seem to depend on the exact method of analysis. Also all the points still lie in the area that is approximately spanned by the observables in our analysis. The same is true for the curve calculated by the Dyson-Schwinger equation.

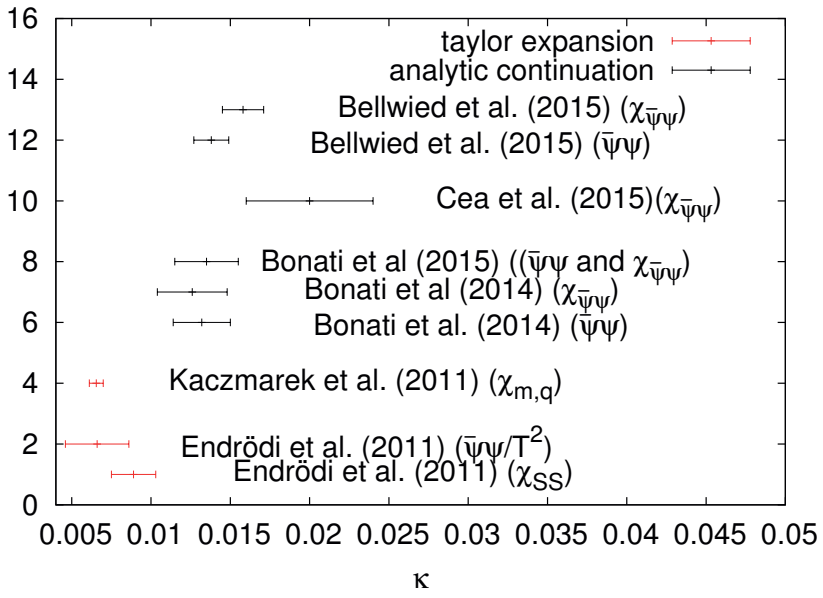

Figure 4.16: *Different values for the curvature κ.*

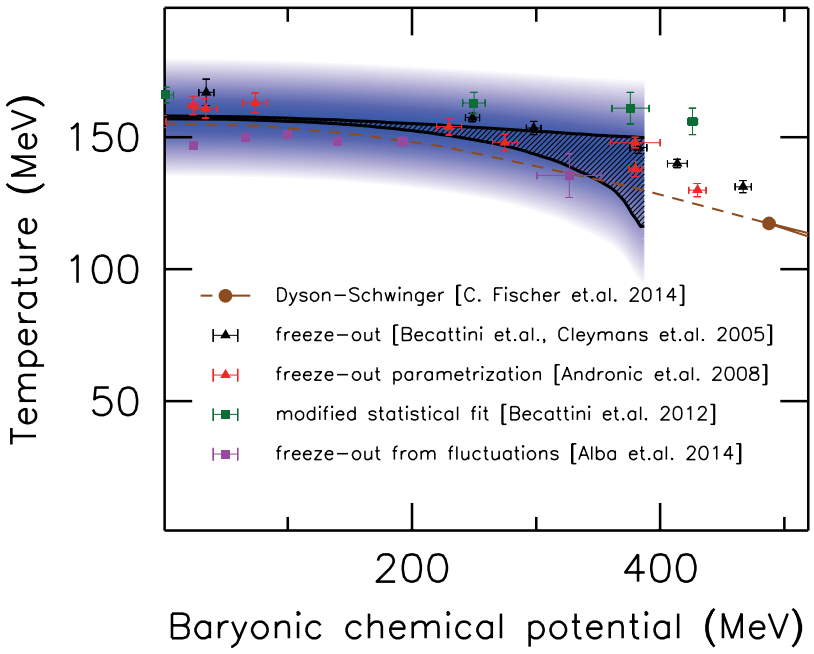

Figure 4.17: *The extrapolation of T_c in comparison to the phenomenological modelling of experimental data for the freeze out points and a calculation by the Dyson-Schwinger equation.*

4.4 The equation of state

In this section we are going to analyse the equation of state at finite density from simulations at imaginary baryon chemical potential. We will use the simulations for $\mu_B^{(0)}$ to $\mu_B^{(7)}$ on lattices with $N_t = 10, 12$ and 16, at temperatures in each dataset between 135 MeV and 210 MeV.

4.4.1 Data at high temperatures

As described in section 4.2 our simulations range up to a temperature of 210 MeV. However for the equation of state we would like to have an analysis that reaches up to approximately 300 MeV where the system is clearly in a state of quark gluon plasma. Since we have simulations in that temperature range for $\mu_B = 0$ we could use the Taylor expansion method in that area. However, we would like to do the same analysis at all temperatures. Therefore instead of using the Taylor expansion method to determine the equation of state directly, we construct some *extrapolated data* we then analyse. The derivative of the pressure is given as:

$$\frac{1}{\hat{\mu}_B}\frac{\mathrm{d}}{\mathrm{d}\hat{\mu}_B}\left(\frac{P}{T^4}\right) = \frac{\mathrm{d}^2\hat{P}}{\mathrm{d}T^2}\hat{\mu}_B^2 + \frac{\mathrm{d}^4\hat{P}}{\mathrm{d}T^4}\hat{\mu}_B^4, \tag{4.64}$$

assuming that higher order terms can be neglected at this high temperatures. This means we are analysing a dataset

$$\left.\frac{\mathrm{d}\hat{P}}{\mathrm{d}\hat{\mu}_B}\right|_{\hat{\mu}_B} = \begin{cases} \left.\frac{\mathrm{d}\hat{P}}{\mathrm{d}\hat{\mu}_B}\right|_{\text{simulated at } \hat{\mu}_B} & \text{for } T < T_{\text{conn}} \\ \left.\frac{\mathrm{d}\hat{P}}{\mathrm{d}\hat{\mu}_B}\right|_{\text{extrapolated to } \hat{\mu}_B} & \text{for } T \geq T_{\text{conn}} \end{cases}. \tag{4.65}$$

To check whether it is save to neglect higher order contributions we will use two different *connection points* T_{conn} from which on we will use the extrapolated data: One at 200 MeV and one at 220 MeV. The difference in this two analysises will then add to our systematic error.

To calculate the high temperature data one has formulate the total derivatives of the pressure in terms of partial derivatives of the partition sum. We use here the notation that has been introduced in section 4.1.1. The first first derivative of the pressure is given as

$$\frac{\mathrm{d}\hat{P}}{\mathrm{d}\hat{\mu}_B} = \chi_B + \chi_S\frac{\mathrm{d}\hat{\mu}_S}{\mathrm{d}\hat{\mu}_B} + \chi_Q\frac{\mathrm{d}\hat{\mu}_Q}{\mathrm{d}\hat{\mu}_B}. \tag{4.66}$$

Now we can derive this a second time yielding

$$\begin{aligned}\frac{\mathrm{d}^2\hat{P}}{\mathrm{d}\hat{\mu}_B^2} = \chi_{BB} + 2\chi_{BS}\frac{\mathrm{d}\hat{\mu}_S}{\mathrm{d}\hat{\mu}_B} + 2\chi_{BQ}\frac{\mathrm{d}\hat{\mu}_S}{\mathrm{d}\hat{\mu}_Q} + \chi_{SS}\left(\frac{\mathrm{d}\hat{\mu}_S}{\mathrm{d}\hat{\mu}_B}\right)^2 \\ + \chi_{QQ}\left(\frac{\mathrm{d}\hat{\mu}_Q}{\mathrm{d}\hat{\mu}_B}\right)^2 + 2\chi_{QS}\frac{\mathrm{d}\hat{\mu}_S}{\mathrm{d}\hat{\mu}_B}\frac{\mathrm{d}\hat{\mu}_Q}{\mathrm{d}\hat{\mu}_B} + \chi_S\frac{\mathrm{d}^2\hat{\mu}_S}{\mathrm{d}\hat{\mu}_B^2} + \chi_Q\frac{\mathrm{d}^2\hat{\mu}_Q}{\mathrm{d}\hat{\mu}_B^2}.\end{aligned} \tag{4.67}$$

Note that at $\mu_B = 0$ where we actually need the derivatives, all odd number of derivatives vanish. However they are still needed to calculate the next order derivative and therefore written down here. Therefore we can now derive the third order derivative as

$$\begin{aligned}\frac{\mathrm{d}^3\hat{P}}{\mathrm{d}\hat{\mu}_B^3} &= \chi_{BBB} + 3\frac{\mathrm{d}\hat{\mu}_S}{\mathrm{d}\hat{\mu}_B}\chi_{BBS} + 3\frac{\mathrm{d}\hat{\mu}_Q}{\mathrm{d}\hat{\mu}_B}\chi_{BBQ} \\ &+ 3\left(\frac{\mathrm{d}\hat{\mu}_S}{\mathrm{d}\hat{\mu}_B}\right)^2(\chi_{BSS}+\chi_{BS}) + 3\left(\frac{\mathrm{d}\hat{\mu}_Q}{\mathrm{d}\hat{\mu}_B}\right)^2(\chi_{BQQ}+\chi_{BQ}) \\ &+ 6\frac{\mathrm{d}\hat{\mu}_S}{\mathrm{d}\hat{\mu}_B}\frac{\mathrm{d}\hat{\mu}_Q}{\mathrm{d}\hat{\mu}_B}\chi_{BQS} + \left(\frac{\mathrm{d}\hat{\mu}_S}{\mathrm{d}\hat{\mu}_B}\right)^3\chi_{SSS} + \left(\frac{\mathrm{d}\hat{\mu}_Q}{\mathrm{d}\hat{\mu}_B}\right)^3\chi_{QQQ} \\ &+ 3\frac{\mathrm{d}\hat{\mu}_Q}{\mathrm{d}\hat{\mu}_B}\left(\frac{\mathrm{d}\hat{\mu}_S}{\mathrm{d}\hat{\mu}_B}\right)^2\chi_{QSS} + 3\frac{\mathrm{d}\hat{\mu}_S}{\mathrm{d}\hat{\mu}_B}\left(\frac{\mathrm{d}\hat{\mu}_Q}{\mathrm{d}\hat{\mu}_B}\right)^2\chi_{QQS} \\ &+ 3\frac{\mathrm{d}\hat{\mu}_S}{\mathrm{d}\hat{\mu}_B}\frac{\mathrm{d}^2\hat{\mu}_S}{\mathrm{d}\hat{\mu}_B^2}\chi_{SS} + 3\frac{\mathrm{d}\hat{\mu}_Q}{\mathrm{d}\hat{\mu}_B}\frac{\mathrm{d}^2\hat{\mu}_Q}{\mathrm{d}\hat{\mu}_B^2}\chi_{QQ} + 3\frac{\mathrm{d}\hat{\mu}_S}{\mathrm{d}\hat{\mu}_B}\frac{\mathrm{d}^2\hat{\mu}_Q}{\mathrm{d}\hat{\mu}_B^2}\chi_{QS} + 3\frac{\mathrm{d}\hat{\mu}_Q}{\mathrm{d}\hat{\mu}_B}\frac{\mathrm{d}^2\hat{\mu}_S}{\mathrm{d}\hat{\mu}_B^2}\chi_{QS} \\ &+ 3\chi_{BQ}\frac{\mathrm{d}^2\hat{\mu}_Q}{\mathrm{d}\hat{\mu}_B^2} + 3\chi_{BS}\frac{\mathrm{d}^2\hat{\mu}_S}{\mathrm{d}\hat{\mu}_B^2} + \chi_S\frac{\mathrm{d}^3\hat{\mu}_S}{\mathrm{d}\hat{\mu}_B^3} + \chi_Q\frac{\mathrm{d}^3\hat{\mu}_Q}{\mathrm{d}\hat{\mu}_B^3}. \end{aligned} \tag{4.68}$$

Finally we can derive the fourth derivative. Here we can actually omit all odd number of derivatives as no further derivatives are needed. This yields

$$\begin{aligned}
\left.\frac{\mathrm{d}^4\hat{P}}{\mathrm{d}\hat{\mu}_B^4}\right|_{\mu_B=0} &= \chi_{BBBB} + \chi_{BBBS}\frac{\mathrm{d}\hat{\mu}_S}{\mathrm{d}\hat{\mu}_B} + \chi_{BBBQ}\frac{\mathrm{d}\hat{\mu}_Q}{\mathrm{d}\hat{\mu}_B} \\
&+ 3\frac{\mathrm{d}\hat{\mu}_S}{\mathrm{d}\hat{\mu}_B}\left(\chi_{BBBS} + \chi_{BBSS}\frac{\mathrm{d}\hat{\mu}_S}{\mathrm{d}\hat{\mu}_B} + \chi_{BBQS}\frac{\mathrm{d}\hat{\mu}_Q}{\mathrm{d}\hat{\mu}_B}\right) \\
&+ 3\frac{\mathrm{d}\hat{\mu}_Q}{\mathrm{d}\hat{\mu}_B}\left(\chi_{BBBQ} + \chi_{BBQS}\frac{\mathrm{d}\hat{\mu}_S}{\mathrm{d}\hat{\mu}_B} + \chi_{BBQQ}\frac{\mathrm{d}\hat{\mu}_Q}{\mathrm{d}\hat{\mu}_B}\right) \\
&+ 3\left(2\frac{\mathrm{d}\hat{\mu}_S}{\mathrm{d}\hat{\mu}_B}\frac{\mathrm{d}^2\hat{\mu}_S}{\mathrm{d}\hat{\mu}_B^2}\chi_{BS} + \left(\frac{\mathrm{d}\hat{\mu}_S}{\mathrm{d}\hat{\mu}_B}\right)^2\left(\chi_{BBSS} + \chi_{BSSS}\frac{\mathrm{d}\hat{\mu}_S}{\mathrm{d}\hat{\mu}_B} + \chi_{BQSS}\frac{\mathrm{d}\hat{\mu}_Q}{\mathrm{d}\hat{\mu}_B}\right)\right) \\
&+ 3\left(2\frac{\mathrm{d}\hat{\mu}_Q}{\mathrm{d}\hat{\mu}_B}\frac{\mathrm{d}^2\hat{\mu}_Q}{\mathrm{d}\hat{\mu}_B^2}\chi_{BQ} + \left(\frac{\mathrm{d}\hat{\mu}_Q}{\mathrm{d}\hat{\mu}_B}\right)^2\left(\chi_{BBQQ} + \chi_{BQQS}\frac{\mathrm{d}\hat{\mu}_S}{\mathrm{d}\hat{\mu}_B} + \chi_{BQQQ}\frac{\mathrm{d}\hat{\mu}_Q}{\mathrm{d}\hat{\mu}_B}\right)\right) \\
&+ 6\frac{\mathrm{d}\hat{\mu}_Q}{\mathrm{d}\hat{\mu}_B}\frac{\mathrm{d}\hat{\mu}_S}{\mathrm{d}\hat{\mu}_B}\left(\chi_{BBQS} + \chi_{BQSS}\frac{\mathrm{d}\hat{\mu}_S}{\mathrm{d}\hat{\mu}_B} + \chi_{BQQS}\frac{\mathrm{d}\hat{\mu}_Q}{\mathrm{d}\hat{\mu}_B}\right) \\
&+ \left(\frac{\mathrm{d}\hat{\mu}_S}{\mathrm{d}\hat{\mu}_B}\right)^3\left(\chi_{BSSS} + \chi_{SSSS}\frac{\mathrm{d}\hat{\mu}_S}{\mathrm{d}\hat{\mu}_B} + \chi_{QSSS}\frac{\mathrm{d}\hat{\mu}_Q}{\mathrm{d}\hat{\mu}_B}\right) \\
&+ \left(\frac{\mathrm{d}\hat{\mu}_Q}{\mathrm{d}\hat{\mu}_B}\right)^3\left(\chi_{BQQQ} + \chi_{QQQS}\frac{\mathrm{d}\hat{\mu}_S}{\mathrm{d}\hat{\mu}_B} + \chi_{QQQQ}\frac{\mathrm{d}\hat{\mu}_Q}{\mathrm{d}\hat{\mu}_B}\right) \\
&+ 3\frac{\mathrm{d}\hat{\mu}_Q}{\mathrm{d}\hat{\mu}_B}\left(\frac{\mathrm{d}\hat{\mu}_S}{\mathrm{d}\hat{\mu}_B}\right)^2\left(\chi_{BQSS} + \chi_{QSSS}\frac{\mathrm{d}\hat{\mu}_S}{\mathrm{d}\hat{\mu}_B} + \chi_{QQSS}\frac{\mathrm{d}\hat{\mu}_Q}{\mathrm{d}\hat{\mu}_B}\right) \\
&+ 3\frac{\mathrm{d}\hat{\mu}_S}{\mathrm{d}\hat{\mu}_B}\left(\frac{\mathrm{d}\hat{\mu}_Q}{\mathrm{d}\hat{\mu}_B}\right)^2\left(\chi_{BQQS} + \chi_{QQSS}\frac{\mathrm{d}\hat{\mu}_S}{\mathrm{d}\hat{\mu}_B} + \chi_{QQQS}\frac{\mathrm{d}\hat{\mu}_Q}{\mathrm{d}\hat{\mu}_B}\right) \\
&+ 3\left(\left(\frac{\mathrm{d}^2\hat{\mu}_S}{\mathrm{d}\hat{\mu}_B^2}\right)^2 + \frac{\mathrm{d}\hat{\mu}_S}{\mathrm{d}\hat{\mu}_B}\frac{\mathrm{d}^3\hat{\mu}_S}{\mathrm{d}\hat{\mu}_B^3}\right)\chi_{SS} + 3\left(\left(\frac{\mathrm{d}^2\hat{\mu}_Q}{\mathrm{d}\hat{\mu}_B^2}\right)^2 + \frac{\mathrm{d}\hat{\mu}_Q}{\mathrm{d}\hat{\mu}_B}\frac{\mathrm{d}^3\hat{\mu}_Q}{\mathrm{d}\hat{\mu}_B^3}\right)\chi_{QQ} \\
&+ 3\left(2\frac{\mathrm{d}^2\hat{\mu}_S}{\mathrm{d}\hat{\mu}_B^2}\frac{\mathrm{d}^2\hat{\mu}_Q}{\mathrm{d}\hat{\mu}_B^2} + \frac{\mathrm{d}\hat{\mu}_S}{\mathrm{d}\hat{\mu}_B}\frac{\mathrm{d}^3\hat{\mu}_Q}{\mathrm{d}\hat{\mu}_B^3} + \frac{\mathrm{d}\hat{\mu}_Q}{\mathrm{d}\hat{\mu}_B}\frac{\mathrm{d}^3\hat{\mu}_S}{\mathrm{d}\hat{\mu}_B^3}\right)\chi_{QS} \\
&+ \frac{\mathrm{d}^3\hat{\mu}_S}{\mathrm{d}\hat{\mu}_B^3}\left(\chi_{BS} + \chi_{SS}\frac{\mathrm{d}\hat{\mu}_S}{\mathrm{d}\hat{\mu}_B} + \chi_{QS}\frac{\mathrm{d}\hat{\mu}_Q}{\mathrm{d}\hat{\mu}_B}\right) \\
&+ \frac{\mathrm{d}^3\hat{\mu}_Q}{\mathrm{d}\hat{\mu}_B^3}\left(\chi_{BQ} + \chi_{QS}\frac{\mathrm{d}\hat{\mu}_S}{\mathrm{d}\hat{\mu}_B} + \chi_{QQ}\frac{\mathrm{d}\hat{\mu}_Q}{\mathrm{d}\hat{\mu}_B}\right). \qquad (4.69)
\end{aligned}$$

Now these whole quantities have to be extrapolated to $\langle n_S\rangle = 0$ and $0.4\langle n_B\rangle = \langle n_Q\rangle$. However it is significantly simpler to extrapolate all the derivatives, analogously to what has been done in section 4.1.3

4.4.2 Observables

For the equation of state the pressure P, the particle number n, the trace anomaly I, the energy density ϵ and the entropy S will be determined. All this quantities can be derived

from the logarithm of the partition sum $\ln Z$. When calculating the derivatives one has to pay attention to the fact that in the simulations (see section 4.2) $\hat{\mu}_B = \frac{\mu_B}{T}$ is held constant while we frequently need derivatives where μ_B itself is constant. We can get the right derivatives by using the formula for a function $f(x, y)$ from [197]:

$$\left.\frac{\partial f}{\partial x}\right|_{z(x,y)} = \left.\frac{\partial f}{\partial x}\right|_{y} + \left.\frac{\partial f}{\partial y}\right|_{x} \left.\frac{\partial y}{\partial x}\right|_{z(x,y)}, \tag{4.70}$$

$$\left.\frac{\partial f}{\partial z}\right|_{y} = \left.\frac{\partial f}{\partial x}\right|_{y} \left.\frac{\partial x}{\partial z}\right|_{y}. \tag{4.71}$$

So for a function depending on T, $\hat{\mu}_B$, $\hat{\mu}_S$ and $\hat{\mu}_Q$:

$$\begin{aligned}\left.\frac{\partial f}{\partial T}\right|_{\mu_B,\mu_S,\mu_Q} &= \left.\frac{\partial f}{\partial T}\right|_{\hat{\mu}_B,\hat{\mu}_S,\hat{\mu}_Q} + \left.\frac{\partial f}{\partial \hat{\mu}_B}\right|_{T,\hat{\mu}_S,\hat{\mu}_Q} \left.\frac{\partial \hat{\mu}_B}{\partial T}\right|_{\mu_B,\mu_S,\mu_Q} \\ &+ \left.\frac{\partial f}{\partial \hat{\mu}_S}\right|_{T,\hat{\mu}_B,\hat{\mu}_Q} \left.\frac{\partial \hat{\mu}_S}{\partial T}\right|_{\mu_S,\mu_B,\mu_Q} + \left.\frac{\partial f}{\partial \hat{\mu}_Q}\right|_{T,\hat{\mu}_B,\hat{\mu}_S} \left.\frac{\partial \hat{\mu}_Q}{\partial T}\right|_{\mu_Q,\mu_B,\mu_S} \qquad (4.72) \\ &= \left.\frac{\partial f}{\partial T}\right|_{\hat{\mu}_B,\hat{\mu}_S,\hat{\mu}_Q} - \frac{\mu_B}{T^2} \left.\frac{\partial f}{\partial \hat{\mu}_B}\right|_{T,\hat{\mu}_S,\hat{\mu}_Q} \\ &- \frac{\mu_S}{T^2} \left.\frac{\partial f}{\partial \hat{\mu}_S}\right|_{T,\hat{\mu}_B,\hat{\mu}_Q} - \frac{\mu_Q}{T^2} \left.\frac{\partial f}{\partial \hat{\mu}_Q}\right|_{T,\hat{\mu}_B,\hat{\mu}_S}. \qquad (4.73)\end{aligned}$$

For a derivative with respect to μ_i while keeping the temperature and the remaining two chemical potentials μ_x and μ_y constant, we get

$$\left.\frac{\partial f}{\partial \mu_i}\right|_{\mu_x,\mu_y,T} = \left.\frac{\partial f}{\partial \mu_i}\right|_{\hat{\mu}_x,\hat{\mu}_y,T} + \left.\frac{\partial f}{\partial \hat{\mu}_x}\right|_{\mu_i,\mu_y,T} \left.\frac{\partial \hat{\mu}_x}{\partial \mu_i}\right|_{\mu_x,\mu_y,T} + \left.\frac{\partial f}{\partial \hat{\mu}_y}\right|_{\mu_i,\mu_x,T} \left.\frac{\partial \hat{\mu}_y}{\partial \mu_i}\right|_{\mu_x,\mu_y,T}. \tag{4.74}$$

Since $\left.\frac{\partial \hat{\mu}_x}{\partial \mu_i}\right|_{\mu_x,\mu_y,T} = 0$ and $\left.\frac{\partial \hat{\mu}_y}{\partial \mu_i}\right|_{\mu_x,\mu_y,T} = 0$, we get

$$\left.\frac{\partial f}{\partial \mu_i}\right|_{\mu_x,\mu_y,T} = \left.\frac{\partial f}{\partial \mu_i}\right|_{\hat{\mu}_x,\hat{\mu}_y,T} \tag{4.75}$$

$$= \left.\frac{\partial f}{\partial \hat{\mu}_i}\right|_{\hat{\mu}_x,\hat{\mu}_y,T} \left.\frac{\partial \mu_i}{\partial \hat{\mu}_i}\right|_{\hat{\mu}_x,\hat{\mu}_y,T} \tag{4.76}$$

$$= T \left.\frac{\partial f}{\partial \hat{\mu}_i}\right|_{\hat{\mu}_x,\hat{\mu}_y,T}. \tag{4.77}$$

This tells us that partial derivatives with respect to μ_i can be easily replaced by derivatives with respect $\hat{\mu}_i$. One just gets the expected factor of T that keeps the dimensions correct. When doing derivatives with respect to T one has to be a bit more careful. However due to the nature of the temperature scans we will only be able to perform total derivatives with respect to T.

The first observable we look at is the pressure P which is given as

$$\frac{P}{T^4} = \frac{1}{T^3 V} \ln Z. \tag{4.78}$$

As described in section 4.1.1 we can only determine derivatives of the partition sum. Therefore we only have data for $\frac{1}{\hat{\mu}_B}\frac{\mathrm{d}}{\mathrm{d}\hat{\mu}_B}\left(\frac{P}{T^4}\right)$. We know [198] that

$$T\frac{\partial}{\partial \mu_i}\left(\frac{P}{T^4}\right) = \frac{n_i}{T^3}. \tag{4.79}$$

Therefore we get:

$$\hat{n}_i = \frac{n_i}{T^3} = \frac{\partial}{\partial \hat{\mu}_i}\left(\frac{P}{T^4}\right). \tag{4.80}$$

So the total derivative of $\frac{P}{T^4}$ can be rewritten as

$$\frac{\mathrm{d}}{\mathrm{d}\hat{\mu}_B}\left(\frac{P}{T^4}\right) = \hat{n}_B + \underbrace{\hat{n}_S}_{0}\chi_{BS} + \underbrace{\hat{n}_Q}_{0.4\hat{n}_B}\chi_{BQ}. \tag{4.81}$$

Having data for the total derivative of the pressure with respect to $\hat{\mu}_B$ allows us to later integrate our function that describes the $\hat{\mu}_B$ dependence of the data to obtain the pressure.

Besides the pressure we also like to investigate the entropy and the trace anomaly. The entropy is defined as

$$S = \left.\frac{\partial P}{\partial T}\right|_{\mu_i}. \tag{4.82}$$

We now need to rewrite it in terms of the total derivative with respect to T. This is given as

$$\frac{\mathrm{d}\hat{P}}{\mathrm{d}T} = \left.\frac{\partial \hat{P}}{\partial T}\right|_{\mu_i} + \frac{\mathrm{d}\mu_B}{\mathrm{d}T}\frac{\hat{n}_B}{T} + \frac{\mathrm{d}\mu_Q}{\mathrm{d}T}\frac{\hat{n}_Q}{T}. \tag{4.83}$$

The total derivatives of the chemical potentials can be written as

$$\frac{\mathrm{d}\mu_B}{\mathrm{d}T} = \frac{\mathrm{d}(\hat{\mu}_B T)}{\mathrm{d}T} = \hat{\mu}_B, \tag{4.84}$$

$$\frac{\mathrm{d}\mu_Q}{\mathrm{d}T} = \frac{\mathrm{d}(\hat{\mu}_Q T)}{\mathrm{d}T} = \hat{\mu}_Q + T\frac{\mathrm{d}\hat{\mu}_Q}{\mathrm{d}T}. \tag{4.85}$$

Leaving the entropy as

$$\hat{S} = \frac{S}{T^3} \tag{4.86}$$

$$= 4\hat{P} + T\frac{\mathrm{d}\hat{P}}{\mathrm{d}T} - \hat{\mu}_B\hat{n}_B - \hat{\mu}_Q\hat{n}_Q - \hat{\mu}_Q T\frac{\mathrm{d}\hat{\mu}_Q}{\mathrm{d}T} \tag{4.87}$$

$$= 4\hat{P} + T\frac{\mathrm{d}\hat{P}}{\mathrm{d}T} - \hat{n}_B\left(\hat{\mu}_B + 0.4\hat{\mu}_Q\right) - 0.4\hat{\mu}_B T\frac{\mathrm{d}\hat{\mu}_Q}{\mathrm{d}T}. \tag{4.88}$$

This leaves us with the extra three terms marked in green, that can not be determined by the pressure. That means besides the data for the pressure we also always analyse the data for $\hat{n}_B$ and $\hat{\mu}_Q$, to determine their dependence on T and on μ_B.

Similarly we get for the energy density

$$\epsilon = \frac{T^2}{V} \left.\frac{\partial \ln Z}{\partial T}\right|_{\mu_i} + \sum_i \mu_i n_i \tag{4.89}$$

$$= T^2 \left.\frac{\partial}{\partial T}\left(T^3 \frac{P}{T^4}\right)\right|_{\mu_i} + \sum_i \mu_i n_i \tag{4.90}$$

$$= T^5 \left.\frac{\partial}{\partial T}\left(\frac{P}{T^4}\right)\right|_{\mu_i} + 3P + \sum_i \mu_i n_i. \tag{4.91}$$

Now we can again replace the partial with the total derivative. However this time some of the extra terms cancel conveniently with the sum over $\mu_i n_i$, yielding:

$$\hat{\epsilon} = \frac{\epsilon}{T^4} \tag{4.92}$$

$$= T\frac{\mathrm{d}\hat{P}}{\mathrm{d}T} + 3\hat{P} - 0.4\hat{\mu}_B T \frac{\mathrm{d}\hat{\mu}_Q}{\mathrm{d}T}. \tag{4.93}$$

Finally the trace anomaly can be calculated from the pressure and the energy density as

$$\hat{I} = \hat{\epsilon} - 3\hat{P} \tag{4.94}$$

$$= T\frac{\mathrm{d}\hat{P}}{\mathrm{d}T} - 0.4\hat{\mu}_B T \frac{\mathrm{d}\hat{\mu}_Q}{\mathrm{d}T}. \tag{4.95}$$

The computation of $\frac{\mathrm{d}\hat{\mu}_Q}{\mathrm{d}T}$ can also serve another purpose beside the computation of the extra terms for the equation of states. Some phenomenological considerations that can be done with $\frac{\mathrm{d}\hat{\mu}_Q}{\mathrm{d}T}$ are presented in [8].

4.4.3 Temperature fit

As in the analysis for the transition temperature (see section 4.3) the first step is to interpolate the data for $\frac{\mathrm{d}\hat{P}}{\mathrm{d}\hat{\mu}_B}$, as well as the data for $\hat{n}_B$ and $\hat{\mu}_Q$ in the temperature direction. Even though the data shows a sigmoid like form similar as the chiral condensate or the strangeness

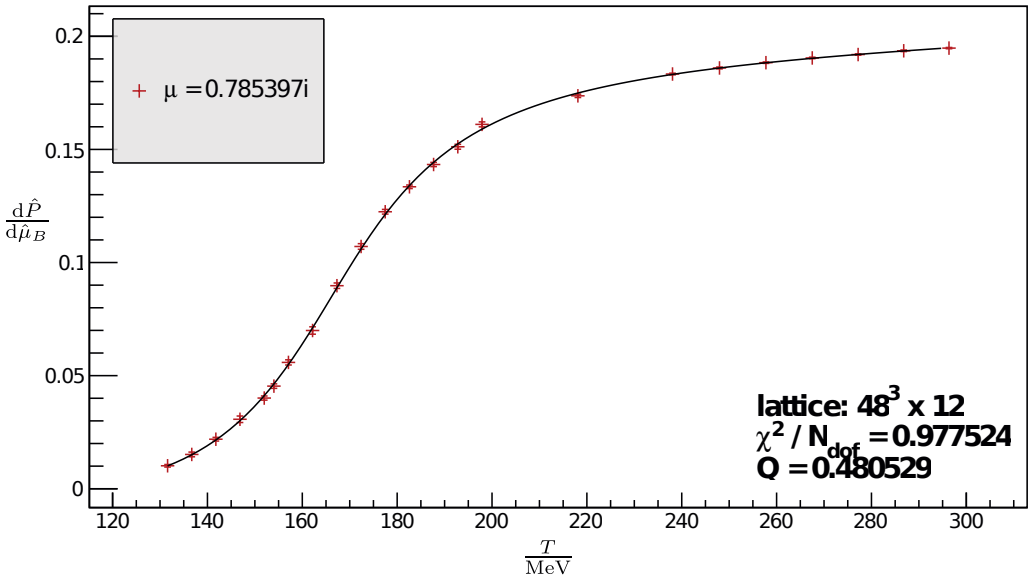

Figure 4.18: *An example for a fit in the T direction.*

susceptibility in section 4.3.1 the tangent hyperbolicus does not provide a good fit. We use the same four fitting functions in all cases in the analysis for the equation of state:

$$A_1(T) = a + b(T-f) + \frac{c}{T-f} + d\arctan(e(T-f)) \tag{4.96}$$

$$A_2(T) = a + b(T-f) + \frac{c}{T-f} + \frac{d}{(1+|e(T-f)|^g)^{1/g}}, \tag{4.97}$$

$$A_3(T) = a + b(T-f) + c(T-f)^2 + d\arctan(e(T-f)) \tag{4.98}$$

$$A_4(T) = a + b(T-f) + c(T-f)^2 + \frac{d}{(1+|e(T-f)|^g)^{1/g}}. \tag{4.99}$$

Where a, b, c, d, e, f and g are the fitting parameters. We do independent fits for every μ_B and every lattice size. An example for a single fit can be seen in figure 4.18. This interpolating fits allow us to align the different temperatures from the different lattice spacings. Second it allows for taking the derivatives with respect to T, that are needed as described in section 4.4.2. Again this fits are only meant as an interpolation and should not be extrapolated beyond the scope of the data as the limits for $T \longrightarrow 0$ or $T \longrightarrow \infty$ clearly give not the correct values.

From here on we have to decide in which direction we do the analytical continuation in the μ_B^2-T-plane. We decide to analyse each observable at a constant temperature as visualized in figure 3.5. Therefore we continue our analysis for every temperature (and every observable) separately from here on. Since the interpolating fit in the T direction also introduces a correlation between different temperatures, this allows us to avoid correlated fits in the further analysis.

4.4.4 μ_B- and continuum fit

The next step in the analysis is to fit the data in the $\hat{\mu}_B^2$ direction. For this we use three different fit functions:

$$B_1(\hat{\mu}) = a + b\hat{\mu}^2 + c\hat{\mu}^4, \tag{4.100}$$

$$B_2(\hat{\mu}) = \frac{a + b\hat{\mu}^2}{1 + c\hat{\mu}^2}, \tag{4.101}$$

$$B_3(\hat{\mu}) = a + b\hat{\mu}^2 + c\frac{\sin(\hat{\mu})}{\hat{\mu}}. \tag{4.102}$$

An example of such a fit is shown in figure 4.19a. If we expand this functions we can get the Taylor coefficients as

$$c_2 = \begin{cases} \frac{a}{2} & \text{for } B_1 \\ \frac{a}{2} & \text{for } B_2 \\ \frac{a}{2} & \text{for } B_3 \end{cases} \tag{4.103}$$

$$c_4 = \begin{cases} \frac{b}{4} & \text{for } B_1 \\ \frac{b-ac}{4} & \text{for } B_2 \\ \frac{b}{4} & \text{for } B_3 \end{cases} \tag{4.104}$$

$$c_6 = \begin{cases} \frac{c}{6} & \text{for } B_1 \\ \frac{c(ca-b)}{6} & \text{for } B_2 \\ \frac{c}{6\cdot 120} & \text{for } B_3 \end{cases} \tag{4.105}$$

$$c_8 = \begin{cases} 0 & \text{for } B_1 \\ \frac{c^2b-ac^3}{8} & \text{for } B_2 \\ \frac{c}{8\cdot 5040} & \text{for } B_3 \end{cases} . \tag{4.106}$$

They are normalized in a way that the pressure can be written as

$$\frac{P(\mu_B, T)}{T^4} = c_0(T) + c_2(T)\left(\frac{\mu_B}{T}\right)^2 + c_4(T)\left(\frac{\mu_B}{T}\right)^4 + c_6(T)\left(\frac{\mu_B}{T}\right)^6 + c_8(T)\left(\frac{\mu_B}{T}\right)^8 + \mathcal{O}(\mu_B^{10}). \tag{4.107}$$

The first two functions are chosen in a way that they allow a wide range for the c_8 coefficient. In B_1 $\frac{c_8}{c_6} = 0$ while in B_2 $\frac{c_4}{c_6} \approx \frac{c_6}{c_8}$. The function B_3 is chosen to resemble the expected behaviour expected for low and for high temperatures. For low temperatures the HRG (see section 3.3.1) predicts that the part of the free energy density that depends on μ_B is proportional to $\cosh\left(\frac{\mu_B}{T}\right)$. If now μ_B is chosen to be purely imaginary this yields $\sin(\hat{\mu})$ for the imaginary energy density. This can be realized by a and b becoming zero or almost zero. For high temperatures the pressure is expected to have the form [199]

$$\frac{P}{T^4} = \frac{8\pi^2}{45} + \frac{7\pi^2}{60}N_f + \frac{1}{2}\sum_f \left(\frac{\mu_f^2}{T^2} + \frac{\mu_f^4}{2\pi^2 T^4}\right), \tag{4.108}$$

which can be realized with non-zero a and b and vanishing c.

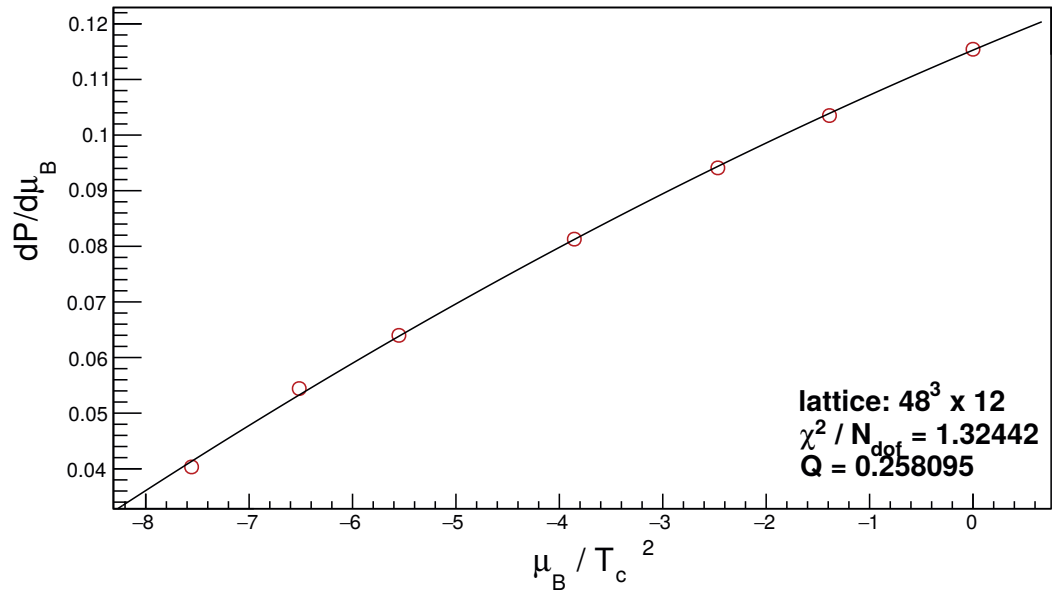

(a) *The fit in $\hat{\mu}_B^2$*

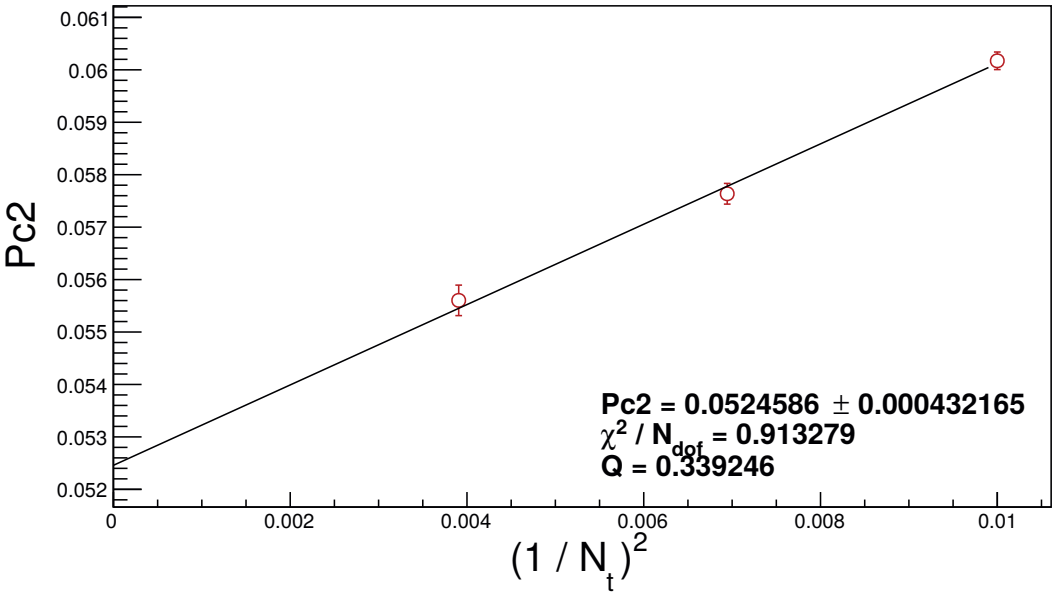

(b) *The continuum fit*

Figure 4.19: *An example for the fit in $\hat{\mu}_B^2$ and the continuum extrapolation.*

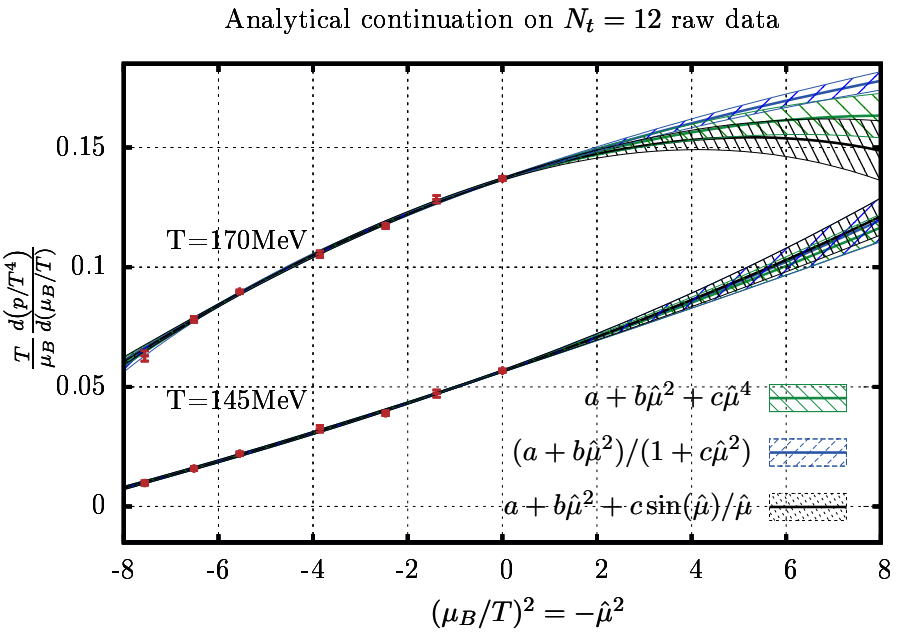

Figure 4.20: *The influence of the different fit functions on the systematical error. [6]*

The different fit functions allow us to estimate how far we can actually extrapolate. As it can be seen in figure 4.20 all three functions describe the data well in the range of $\mu_B^2 \leq 0$. Still they can differ significantly in the $\mu_B^2 \geq 0$ range, depending on the temperature. The plot in figure 4.20 is for the $N_t = 12$ lattice as this allows a comparison to the raw data.

The next step is the continuum extrapolation. Again as in the analysis for the temperature (see section 4.3.3) we use a linear fit though the data from $N_t = 10, 12$ and 16. An example plot for the c_2 coefficient of the pressure is shown in figure 4.19b.

Again as described in section 4.3.4 for the crossover temperature we use a combined fit for the μ_B direction and the continuum extrapolation. The fit functions we use for this have the form

$$B_1(\hat{\mu}) = a_1 + \frac{a_2}{N_t^2} + \left(b_1 + \frac{b_2}{N_t^2}\right)\hat{\mu}^2 + \left(c_1 + \frac{c_2}{N_t^2}\right)\hat{\mu}^4, \tag{4.109}$$

$$B_2(\hat{\mu}) = \frac{a_1 + \frac{a_2}{N_t^2} + \left(b_1 + \frac{b_2}{N_t^2}\right)\hat{\mu}^2}{1 + \left(c_1 + \frac{c_2}{N_t^2}\right)\hat{\mu}^2}, \tag{4.110}$$

$$B_3(\hat{\mu}) = a_1 + \frac{a_2}{N_t^2} + \left(b_1 + \frac{b_2}{N_t^2}\right)\hat{\mu}^2 + \left(c_1 + \frac{c_2}{N_t^2}\right)\frac{\sin(\hat{\mu})}{\hat{\mu}}. \tag{4.111}$$

Again the combined fit reduces the number of fit parameters significantly. A fit in the combined fitting approach has six fit parameters, while in the separate approach there are two fit parameters for every μ_B out of seven on three lattice sizes plus two fit parameter for the continuum extrapolation adding up to $2 \cdot 7 \cdot 3 + 2 = 44$ fit parameters.

The error is determined in the same way as described in section 4.3.5. The statistical error is determined via the bootstrap method with 1000 bootstrap samples. For the systematic error we use a histogram of all different analysises and take the central 68%. In this case we have the following options to chose from for different analysises:

- two methods of scale setting
- four fits in the T direction
- three fits in the μ_B direction
- combined and separate μ_B-fit and continuum extrapolation
- two different points T_{conn} from which we use the data extrapolated from $\mu_B = 0$ at high temperatures.

This adds up to a total of $2 \cdot 4 \cdot 3 \cdot 2 \cdot 2 = 96$ analysises.

4.4.5 Taylor coefficients

From the equations (4.103) to (4.105) we can determine the Taylor coefficients of the pressure as given in equation (4.107). The continuum extrapolated results, together with the expectations from the HRG model (see section 3.3.1) are shown in figure 4.21. The values for c_0 are taken from [149]. As expected the results of the HRG model agree with our calculation up to a temperature of approximately 150 MeV which is already close to the transition. For c_6 a sign change is expected from chiral models [200]. Even though we can not show that c_6 is lager then zero at any point as it is always compatible to zero below $T = 160$ MeV, it clearly drops below zero in the range between 160 MeV and 190 MeV.

For temperatures larger then 220 MeV we know that c_6 has to be exactly zero, as our extrapolations at this temperatures do not include a sixth order coefficient (see section 4.4.2). The error that our results have in this range gives us a feeling of how much of the uncertainties is introduced as a systematic by our analysis, even if the statistical precision of the data would be perfect.

From the Taylor coefficient we can calculate $\hat{n}_B$ to different orders. Using only the c_2 coefficient is a calculation up to $\mathcal{O}(\mu_B)$ as the pressure has to be integrated over μ_B compared to $\hat{n}_B$. For a temperature of 145 MeV only the c_2 and c_4 coefficient contribute to the result as shown in figure 4.22a. Extending the extrapolation to order $\mathcal{O}(\mu_B^5)$ we only increase the error compared to a third order calculation. This is not surprising as figure 4.21 shows that at $T = 145$ MeV c_6 is compatible with zero. However at a temperature where c_6 differs significantly from zero, for example 170 MeV, the additional order has a definite influence as can be seen in figure 4.22b.

Finally we can compare our results to other calculations. In [201] the coefficients c_2 to c_6 were presented on $N_t = 6$ and $N_t = 8$ lattices. They can be seen in figure 4.23. They were calculated with the HISQ action and staggered fermions in the same set-up as our calculation: at the strangeness neutral point and with $0.4\langle n_B \rangle = \langle n_Q \rangle$. However they were not calculated from simulations at imaginary chemical potential but with the Taylor expansion method. Therefore even if they are not continuum extrapolated yet, they are a good choice for a comparison.

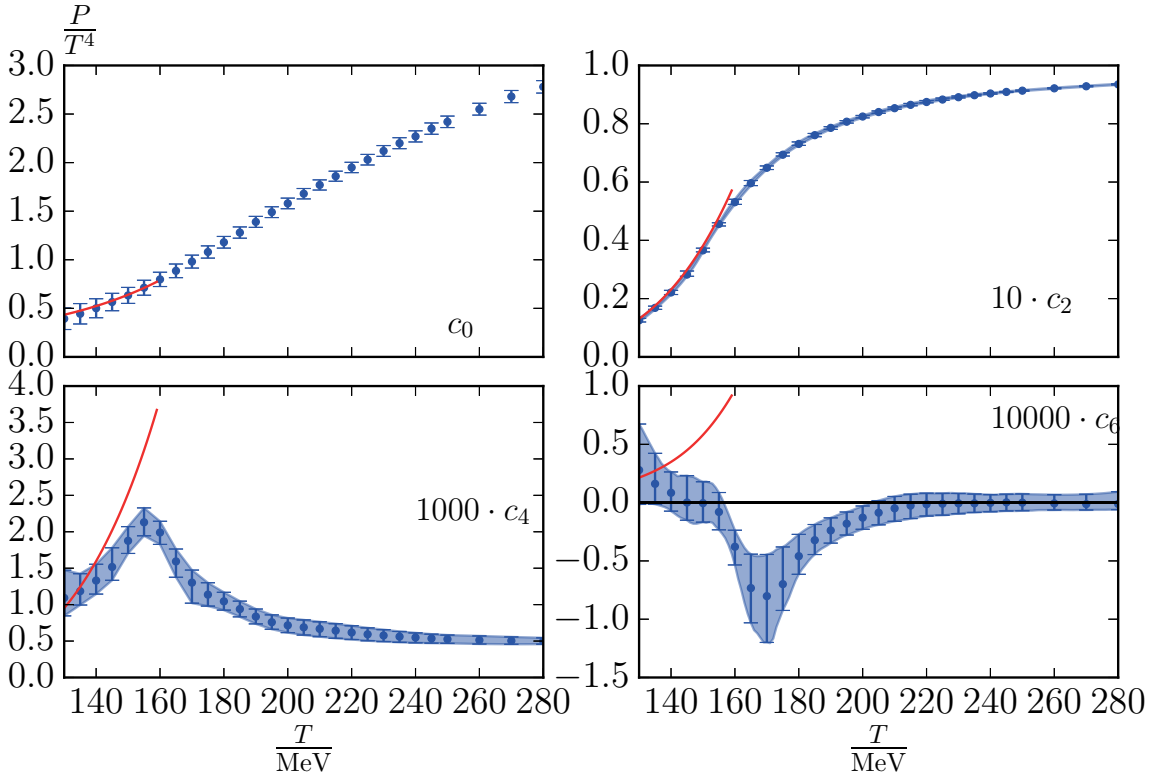

Figure 4.21: *The Taylor coefficients of the pressure. The values for c_0 are taken from [149]. The red line shows the expectations of the HRG model.*

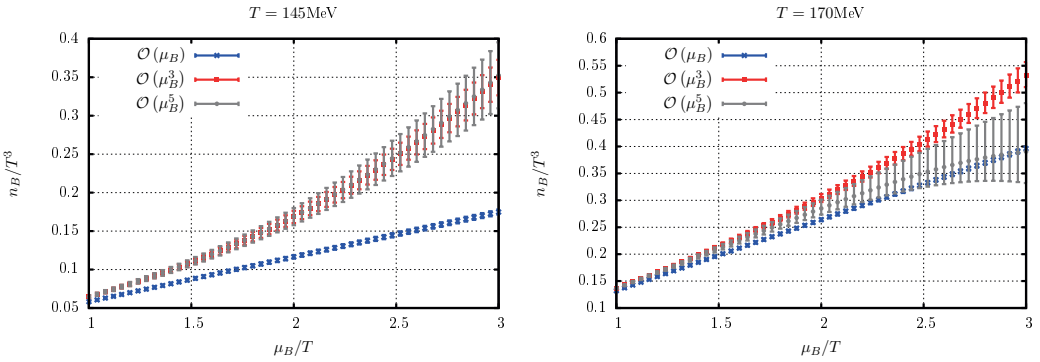

(a) $T = 145$ *MeV* **(b)** $T = 170$ *MeV*

Figure 4.22: *The contribution of the different order coefficients to the baryon number. [6]*

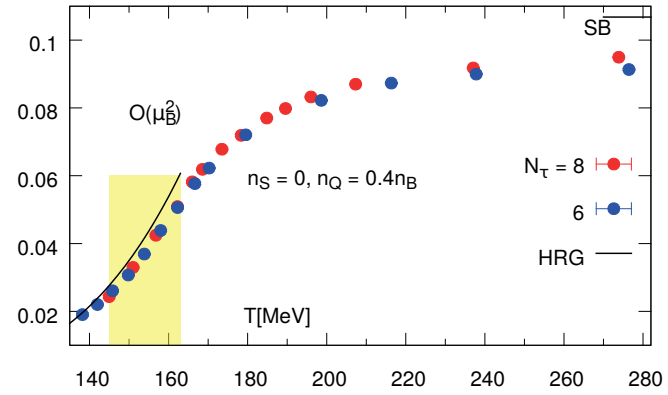

(a) c_2

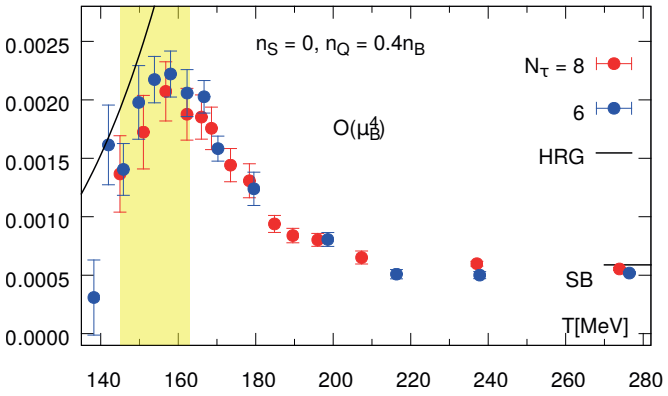

(b) c_4

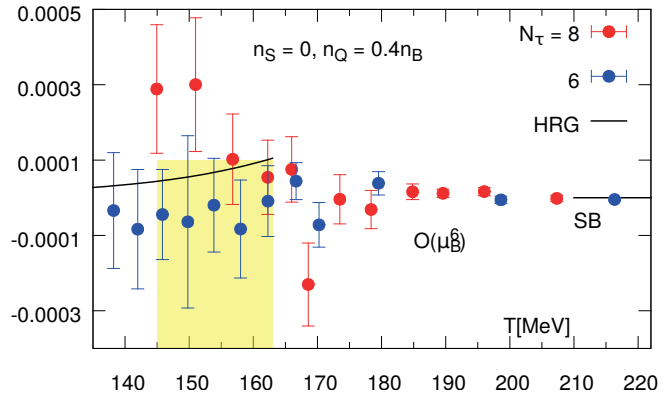

(c) c_6

Figure 4.23: *The Taylor coefficients of the pressure on lattices with $N_t = 6$ and $N_t = 10$ from [201].*

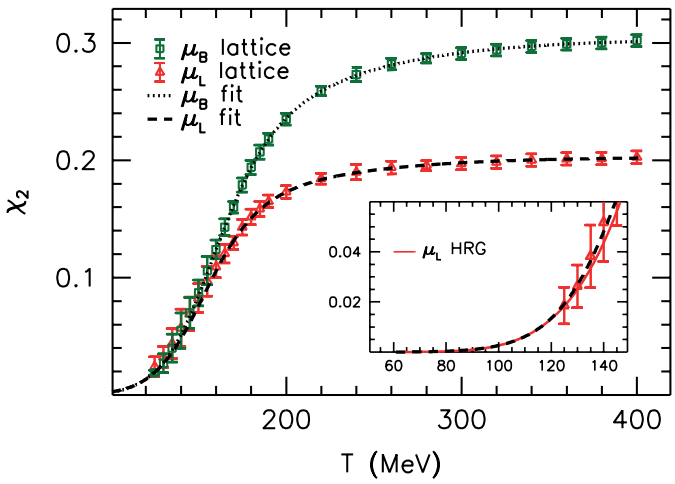

Figure 4.24: *Result for $\chi_2 = 2c_2$. [202] The red points are calculated at the strangeness neutral point, while the green points are calculated for $\mu_u = \mu_d = \mu_s$.*

c_2 starts a little below 0.02, grows in the transition region and reaches a value shortly below 0.1 at 280 MeV. This fits well to our results. As the values for $N_t = 6$ and $N_t = 8$ are very close together in figure 4.23a, we can assume that the result is already close to the continuum. Also the values for c_4 seem to be in good agreement. In both cases there is a peak slightly below 160 MeV reaching a value of approximately 0.005. Then for high temperatures c_4 drops down to a value of about 0.0005 as shown in figure 4.23b. For c_6 (see figure 4.23c) however the errors are too large and the results for $N_t = 6$ and $N_t = 8$ are too far apart to make a good comparison.

An other possibility for comparison is [202]. Here continuum extrapolated results for $\chi_2 = 2c_2$ are presented, which are calculated by the Taylor expansion method. The results at the strangeness neutral point are shown by the red points in figure 4.24. Here the temperature range that was analysed is larger. It goes up to 400 MeV, where χ_2 reaches a value of 0.2. This fits our results where at a temperature of 280 MeV c_2 is a little bit below 0.1.

4.4.6 Isentropic trajectories

In heavy ion collisions if one neglects dissipative effects, the quark gluon plasma created in the collision expands with a fixed baryon number and without generation of entropy. Therefore the ratio $\frac{S}{N_B}$ is constant. The medium cools down along isentropic trajectories (where $\frac{S}{N_B}$ is constant) in the T-μ_B-plane. In this section we are going to calculate these trajectories and match them to the freeze-out values for the temperature and the baryon chemical potential that are given in [203].

The baryon number density n_B we can calculate directly from the expansion of our fit functions given in equation (4.100) to (4.102). For the entropy however we have to integrate equation (4.100) to (4.102) over μ_B. To determine the integration constant we use the values from [149]

and determine the offset in a way that at $\mu_B = 0$ the entropy matches the result from [149]. Afterwards we have to solve the equation

$$\frac{S}{N_B} = \frac{s}{n_B} = c \tag{4.112}$$

for various values of the constant c until we match the points given in [203]. The result can be seen in figure 4.25. The black points are the values calculated in [203] while the solid lines are predictions of the HRG model that we use to continue our trajectories at lower temperatures. The energy given at each trajectory is the RHIC beam energy that corresponds to the trajectory. As it can be seen from the errors the trajectory with $\frac{S}{N_B} = 30$ corresponding to a beam energy of 14.5 GeV is at the end of how far we can extrapolate in μ_B.

Finally we want to know how large the influence, of the higher order coefficients we calculated, is. Therefore we extrapolate only with the polynomial fit function $B_1(\mu_B)$ (see equation (4.100)) and use a different number of coefficients in the extrapolation. The result is shown in figure 4.26. For high beam energies and small μ_B the first coefficient would have been enough and higher order coefficients do not change the result at all. However for lower beam energies and larger chemical potential c_4 becomes relevant. For the lowest beam energy of 14.5 GeV and $\frac{S}{N_B} = 30$ we were unable to solve the equation with the c_2 coefficient only. This is a quadratic equation that did not have a real solution at all temperatures. We also can see a difference in the result when including the c_6 coefficient at some temperatures. Even though at the moment the error is to large to distinguish the results for the whole temperature range.

4.4.7 The equation of state

Finally we can compute the equation of state along the trajectories introduced in section 4.4.6. Since the error on the trajectory with $\frac{S}{N_B} = 30$ is quite large, we focus on the trajectory next to it with $\frac{S}{N_B} = 51$ that corresponds to a beam energy of 19.6 GeV and the trajectory with the largest ratio of $\frac{S}{N_B} = 420$. In figure 4.27 we show the pressure and the trace anomaly calculated along these trajectories. Again to get this curve we have to integrate equation (4.100) to (4.102) over μ_B and in the same way we did for the entropy (section 4.4.6), we use the results from [149] to set the value at $\mu_B = 0$. It can be seen from the figure 4.27 that both the pressure and the trace anomaly are higher for larger μ_B, which corresponds to smaller $\frac{S}{N_B}$. However while the difference for the pressure is most noticeably for large temperatures, for the trace anomaly it mostly influences the middle temperature region.

Again for comparison to other results we can look at [202]. Here the equation of state was also computed along trajectories with constant $\frac{S}{N_B}$. Also in their plots we can make the observation that the increase in μ_B matters for the pressure mostly at high temperatures, it is most relevant for the trace anomaly in the region of its peak.

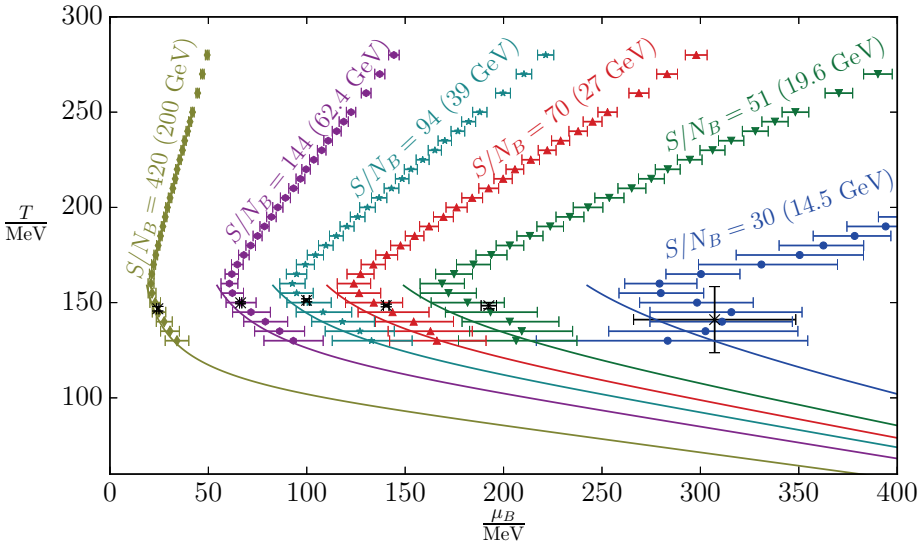

Figure 4.25: *The trajectories of constant $\frac{S}{N_B}$ matched to the beam energies of RHIC as determined in [203].*

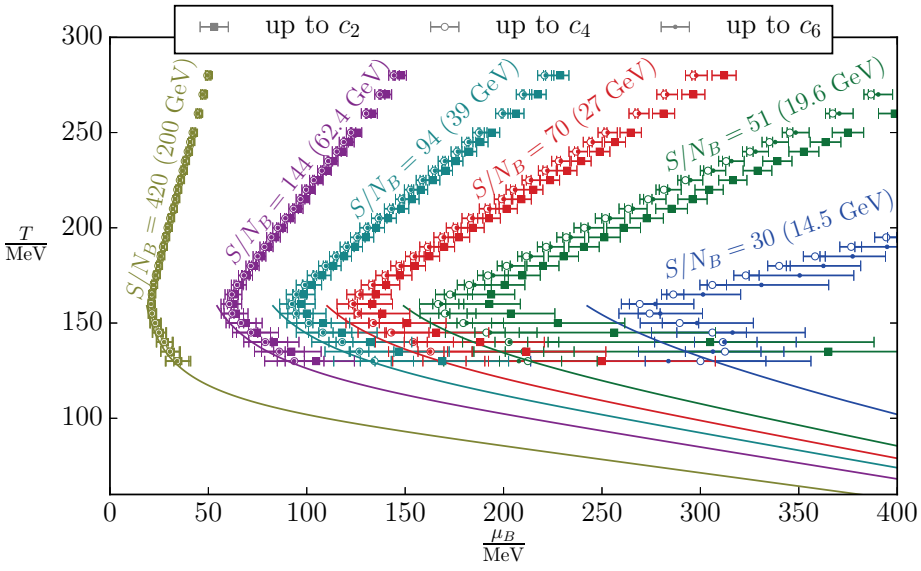

Figure 4.26: *The influence of the different orders to the trajectories of constant $\frac{S}{N_B}$.*

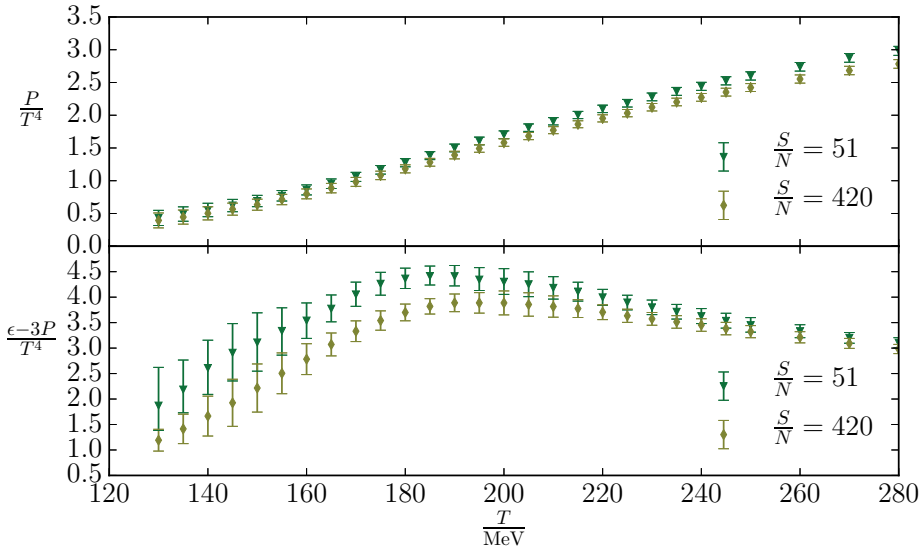

Figure 4.27: *The pressure and the trance anomaly along trajectories of constant* $\frac{S}{N}$.

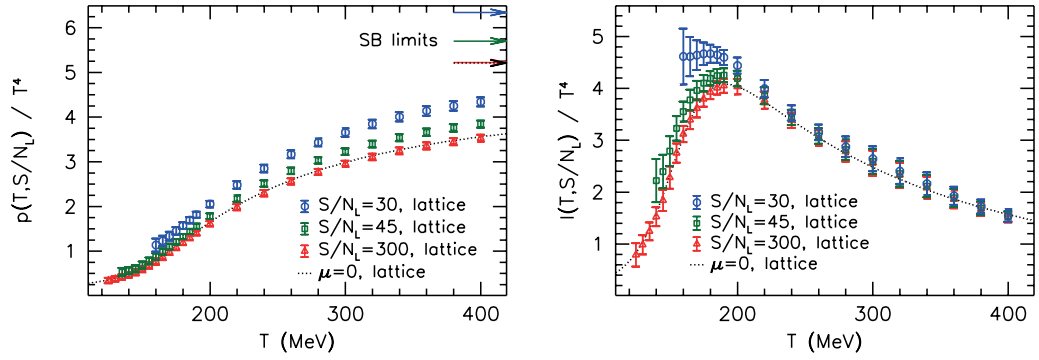

(a) *The pressure* **(b)** *The trace anomaly*

Figure 4.28: *The equation of state calculated along trajectories of constant* $\frac{S}{N_B}$ *in [202].*

5 Searching for Axions

As described in section 3.5 axions are interesting candidates for dark matter particles. To determine the mass of axions the topological susceptibility is one important ingredient. In this chapter we present in section 5.1 a calculation for the topological susceptibility that has been published in [7]. In section 5.2 we then discuss some properties of a possible experiment to search for axions in the mass range predicted in [7].

5.1 The topological susceptibility

As described in section 3.5 from the equation of state and the topological susceptibility the axion mass can be estimated. However the topological susceptibility is very hard to calculate on the lattice as discussed in the following section. Here we will introduce some new techniques that made it possible to calculate the topological susceptibility in [7].

On the lattice the topological charge can be defined in different ways. One is the so called fermionic definition. The topological charge q is defined as the difference of the left handed zero modes n_- and the right handed zero modes n_+ [27]. This definition is related via the *index theorem* [204, 205] to the definition [206]

$$q^{(f)} = \frac{a}{2} \operatorname{tr} (\gamma_5 D) = n_- - n_+. \tag{5.1}$$

Another definition for the topological charge is the so called gluonic definition

$$q^{(g)} = \frac{1}{16\pi^2} \sum_x F_{\mu\nu}(x) \tilde{F}^{\mu\nu}(x), \tag{5.2}$$

where F is a lattice definition of the field strength tensor, for example

$$F_{\mu\nu}(x) = \frac{1}{8} \left(G_{\mu\nu}(x) - G^{\dagger}_{\mu\nu}(x) \right) \tag{5.3}$$

where G is the clover leave term: The sum over four neighbouring plaquettes in a plane [42]. However as described in [42] $q^{(g)}$, as defined by the gluonic definition, is not necessarily an integer as its counterpart from the fermionic definition $q^{(f)}$. $q^{(g)}$ and $q^{(f)}$ have to be equivalent in the continuum limit.

The gradient flow is defined via the differential equation

$$\frac{\mathrm{d}}{\mathrm{d}\tau} A_\mu(\tau) = D_\nu F_{\nu\mu}(\tau) \tag{5.4}$$

where $A_\mu(0)$ is the continuum gauge field A_μ and D_ν is the covariant derivative. The appropriate lattice definition of this equation is the so called *Wilson flow* [207]. It has many interesting properties. One of these is that it brings a gauge configuration closer to a classical solution of the equation of motions, which is a local minimum of the action. Thus this also brings the gluonic definition of the topological charge closer to an integer value. For appropriate flow times the remaining non integer part vanishes in the continuum limit. For an integer definition on the lattice configurations one can determine the renormalisation factor Z from minimizing the expression

$$\sum_i \left(Zq_i - \text{round}\left(Zq_i\right)\right)^2, \tag{5.5}$$

where i runs over all configurations in the ensemble and *round* sets Zq_i to the closest integer value [42]. The renormalized charge can then be defined as

$$Q = \text{round}\left(Zq\right). \tag{5.6}$$

The topological susceptibility is then given as

$$\chi = \frac{\langle Q^2 \rangle}{V}. \tag{5.7}$$

One problem one encounters while computing the topological susceptibility on the lattice, is that for the topological susceptibility staggered quarks have very large cutoff effects. This can be reduced by a technique called *eigenvalue reweighting* that is introduced in section 5.1.1. Another difficulty is that it takes very long to sample different topological sectors. This can be circumvented by the *fixed sector integral method* that is introduced in section 5.1.2

5.1.1 Eigenvalue reweighting technique

In figure 5.1 it can be seen, that the continuum behaviour of the topological susceptibility with staggered fermions is problematic. For the brute force approach, that is shown by the green points, the continuum slope is very strong. To obtain the correct continuum limit very fine lattice are needed. For figure 5.1 lattices up to $N_t = 20$ were used.

The strong cutoff effects of the staggered fermions are related to the fact, that on the lattice the would be zero eigenmodes are not exactly zero in the staggered operator. In figure 5.2 it can be seen how the zero modes of the overlap operator split up and contribute two modes slightly above and two modes lightly below zero for the staggered operator.

A zero mode in the quark determinant contributes a factor $2m_f$ to the weight of configuration in the topological susceptibility for every dynamical flavour. Since for quark masses close to the physical ones m_f is very small, configurations with zero modes, corresponding to higher topological sectors, are strongly suppressed. However when the staggered operator is used, instead of a factor $2m_f$ one gets a factor $2m_f + \mathrm{i}\lambda_0$ where λ_0 is the would-be eigenmode of the staggered operator. Therefore the suppression is much milder, increasing the influence of higher topological sectors. This leads to large cutoff effects and a bad convergence in the continuum limit.

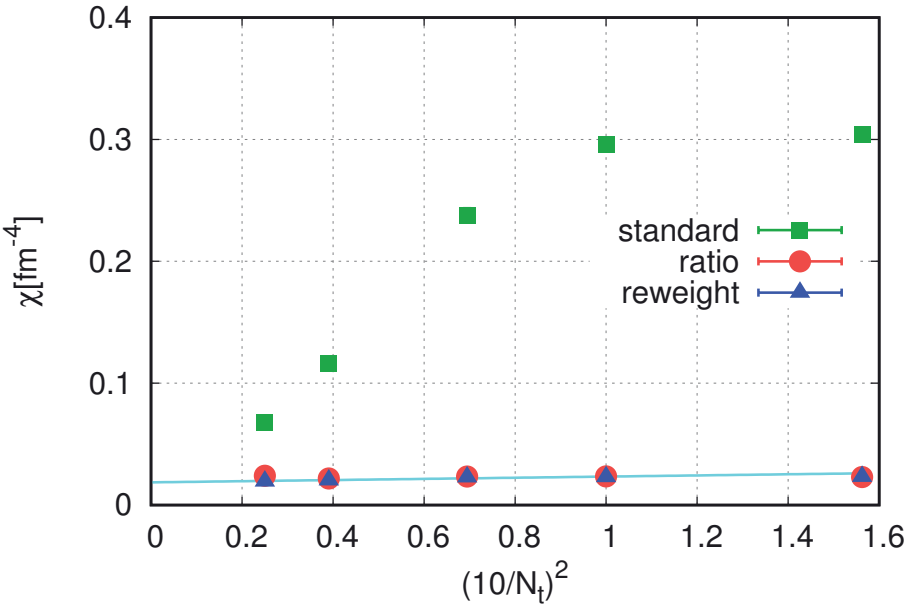

Figure 5.1: *The behaviour of the topological susceptibility in the continuum extrapolation for three different methods described in [7]. The plot shows $N_f = 2 + 1 + 1$ flavour simulations with staggered fermions at a temperature of $T = 150$ MeV.*

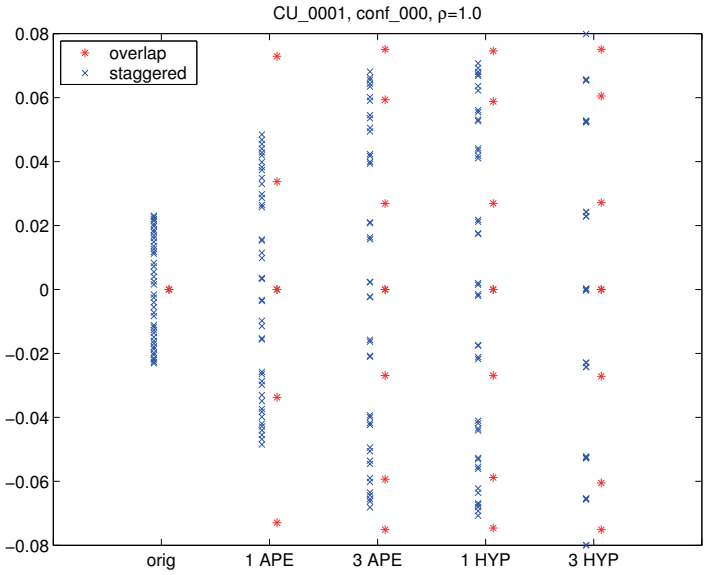

Figure 5.2: *Comparison of staggered and overlap operator eigenmodes, taken from [208].*

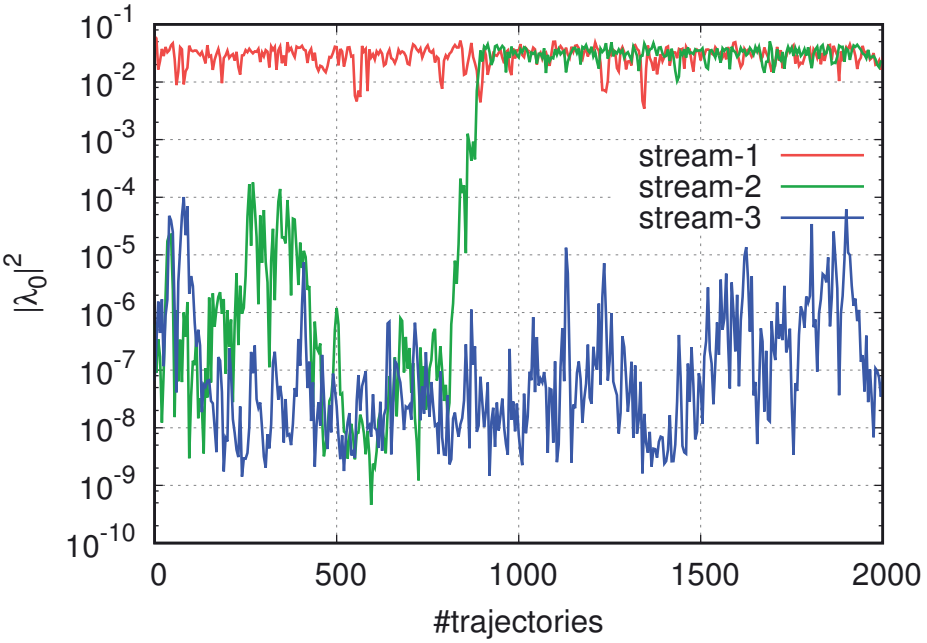

Figure 5.3: *The lowest eigenmode squared from $N_f = 3$ overlap simulations an a 6×24^3 lattice at $T = 300$ MeV from three diffrent streams. In stream 1 there is no instanton. In stream 3 there is an instanton-anti-instanton-pair and in stream 2 such a pair annihilates. [7]*

The idea of the Eigenvalue reweighting technique is to bring the weight closer to the continuum weight for each configuration. For a staggered operator that is used with rooting the weight for a configuration U is given as:

$$w(U) = \prod_f \prod_{n=1}^{2N_{\max}} \prod_{\sigma=\pm} \left(\frac{2m_f}{\sigma \mathrm{i}\lambda_n(U) + 2m_f} \right)^{\frac{n_f}{4}} . \tag{5.8}$$

Here f runs over all dynamical flavours in the simulation. The $\frac{n_f}{4}$ exponent is a result of the rooting procedure. $N_{\max}$ is number of zero modes. The factor two, together with the product over σ takes into account that a zero mode splits up to four would-be zero modes in the staggered operator. Of this four eigenmodes two lay above and two below zero [208].

For the definition of $N_{\max}$ there are two possible choices. The first one is to take the absolute value of the gluonic definition of the topological charge. The second one is to take the sum of the number of instantons n_I and the number of anti-instantons n_A. To determine $n_I + n_A$ we look at eigenvalues λ_i of the overlap operator where $|\lambda_i|^2 < 10^{-4}$. From figure 5.3 we can see, that if there is no instanton as in stream one, even the smallest eigenvalue will be larger. An instanton-anti-instanton pair will lead to $10^{-13} < |\lambda_i|^2 < 10^{-4}$ as in stream 3. If $|\lambda_i|^2 < 10^{-13}$ we assume the presences of a single instanton or anti-instanton. From this we can calculate $n_I + n_A = N_{\max}$. We then take the $2N_{\max}$ eigenvalues with the smallest magnitude.

In figure 5.4 we show the histograms for the topological charge before the renormalisation for the different reweighting techniques as well as without reweighting. It can be seen that the

weight of the configurations with higher topological charge decreases in figure 5.4b and figure 5.4c compared to figure 5.4a where no reweighting was used.

We now calculate the topological susceptibility on $32^3 \times 8$, $40^3 \times 10$, $48^3 \times 12$ and $64^3 \times 16$ lattices and determine the continuum limit for $T = 300$ MeV. The result is shown in figure 5.5. The two possible reweighting techniques converge to the same continuum value within the error, while the result without any reweighting gives a different value.

As the rooting procedure for the staggered operator this reweighting technique is a non local modification of the path integral. This topic is discussed in [7] where several numerical evidence for its correctness are presented. [7] also discusses another choice for "smallest" eigenvalue. Instead of choosing the eigenvalues with smallest magnitude one can also chose the eigenvalues with largest magnitude of chirality and the appropriate sign. This procedure gives a consistent result in the continuum limit as well.

5.1.2 Fixed sector integral method

The dilute instanton gas approximation (DIGA) [210, 211] can be used to estimate the topological susceptibility at high temperatures. It predicts a power law behaviour. In [209] the exponent of this power law has been calculated in quenched lattice simulations to be about -7. As it can be seen in figure 5.6, this means that the topological susceptibility decreases rapidly with increasing temperature and agrees well with the results from the DIGA. Thus for hight temperatures the weight of the $Q = 0$ sectors increases. This makes it harder to measure χ. Also with smaller lattice spacing the simulation stays longer in one topological sector as shown in [212]. Both points lead to the need for very long streams at hight temperatures and small lattice spacing. There are some methods that increase the tunnelling between different topological sectors [213, 214, 215]. However here we are using a different method that was developed simultaneously in [216] (for quenched QCD) and [7] (also for fermions). The idea of this method is to do simulations in fixed topological sectors and than calculate the weight for the different topological sectors. If Z_Q is the partition sum in the topological sector Q one can define

$$b_Q = \frac{\mathrm{d} \ln \left(\frac{Z_Q}{Z_0} \right)}{\mathrm{d} \ln T} = \frac{\mathrm{d}\beta}{\mathrm{d} \ln a} \left(\langle S_G \rangle_Q - \langle S_G \rangle_0 \right) \tag{5.9}$$

Where $\langle S_G \rangle_Q$ is the expectation value of the gauge action in the topological sector Q. b_Q is a renormalized quantity as the ultraviolet divergences are cancelled by the subtraction of the expectation values. The computation time necessary to determine b_Q does not depend on the temperature.

To obtain the ratio $\frac{Z_Q}{Z_0}$ one can integrate b_Q yielding

$$\frac{Z_Q}{Z_0}(T) = \exp \left(\int_{T_0}^{T} \mathrm{d} \ln T' b_Q(T') \right) \frac{Z_Q}{Z_0}(T_0). \tag{5.10}$$

The starting temperature T_0 can then be chosen low enough that the simulation is still feasible.

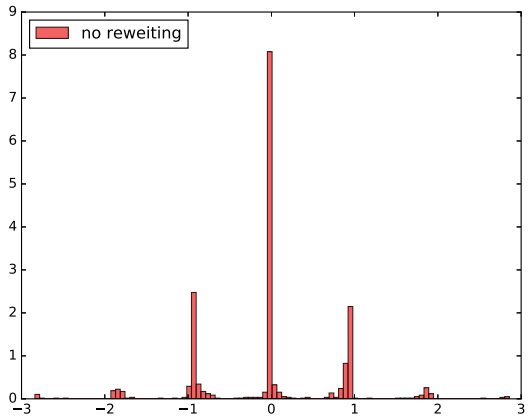

(a) *no reweighting*

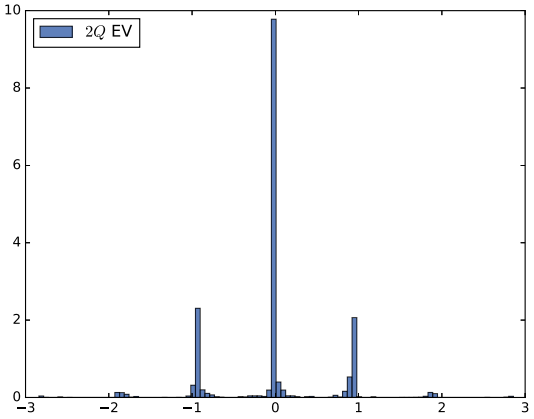

(b) $2N_{max} = 2Q$

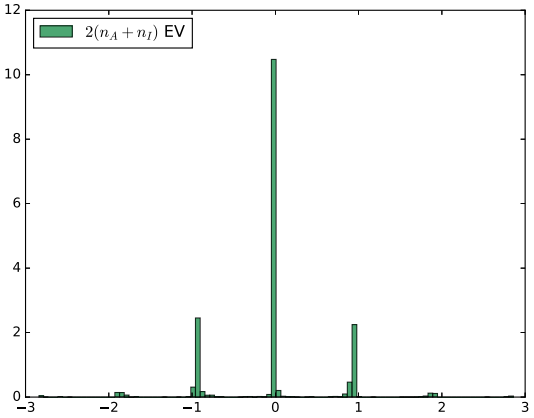

(c) $2N_{max} = 2(n_A + n_I)$

Figure 5.4: *The histogram for the topological charge depending on which reweighting technique is used.*

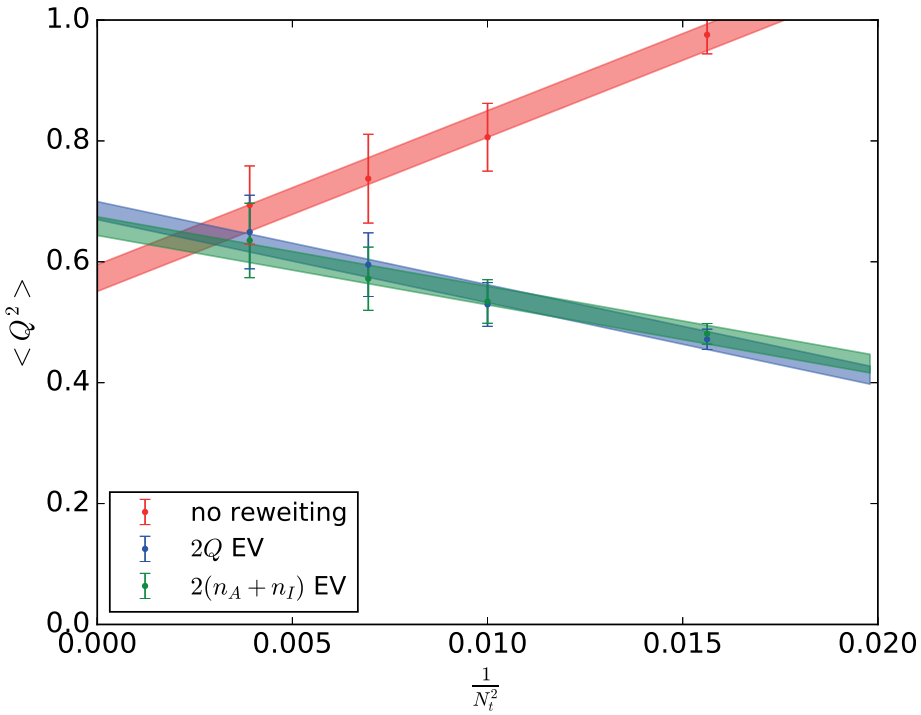

Figure 5.5: *The result of the continuum extrapolation of the topological susceptibility depending which reweighting technique is used.*

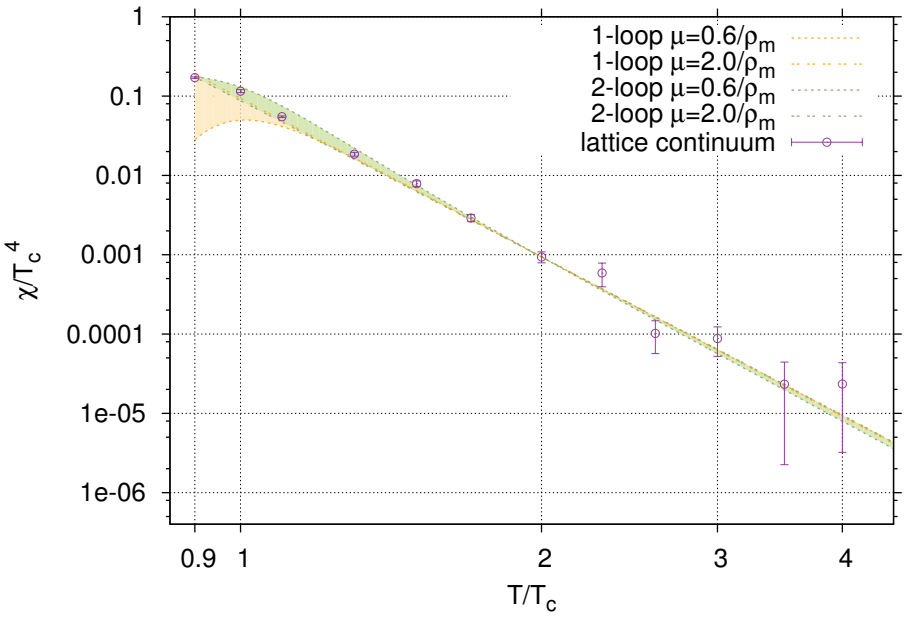

Figure 5.6: *Comparison of the quenched lattice results with the results in the DIGA. [209]*

If the temperature is high enough the only relevant sectors are $Q = 1$ and $Q = 0$. The topological susceptibility is then given as

$$\chi = \frac{2Z_1}{Z_0 N_s^2 N_t a^4} \tag{5.11}$$

and the rate of change of the susceptibility can be calculated as

$$b = \frac{\mathrm{d}\chi}{\mathrm{d}\ln T} = b_1 - 4 \tag{5.12}$$

where the -4 comes from the change of the physical volume with the temperature.

Several numerical test, as well as another trick to further decreases the computation time are discussed in [7]. However the next step is to generalize this method for fermions. For a system where the temperature is increased along a line of constant physics this is done with defining

$$b_Q = \frac{\mathrm{d}\ln\left(\frac{Z_Q}{Z_0}\right)}{\mathrm{d}\ln T} = \frac{\mathrm{d}\beta}{\mathrm{d}\ln a}\left(\langle S_G\rangle_Q - \langle S_G\rangle_0\right) + \sum_f \frac{\mathrm{d}\ln m_f}{\mathrm{d}\ln a} m_f \left(\langle\bar{\psi}\psi_f\rangle_Q - \langle\bar{\psi}\psi_f\rangle_0\right). \tag{5.13}$$

Here the problem arises that $\langle\bar{\psi}\psi_f\rangle$ has large cutoff effects for staggered fermions. This is related to the zero modes similar to the case of the topological susceptibility and can be cured by the same eigenvalue reweighting technique that is described in section 5.1.1.

The result achieved by this method for b from $N_f = 3 + 1$ staggered simulations can be seen in figure 5.7. The red band shows the continuum limit from $N_t = 4, 6, 8$ and 10 lattices. It includes both the systematic and the statistic error. The statistic error is obtained via the Jack-Knife method with twenty Jack-Knife-samples. The analysis was done on lattices with the lattice sizes $8^3 \times 4$, $12^3 \times 4$, $16^3 \times 4$, $24^3 \times 4$, $12^3 \times 6$, $16^3 \times 8$ and $20^3 \times 10$. The continuum extrapolation and the temperature fit uses a fit of the form

$$b(\tau) = b_{T0} + b_{T1}\tau + b_{T2}\tau^2 + b_{T3}\tau^3 + \frac{b_A}{N_t^2} + b_L\left(\frac{N_t}{N_s}\right)^3 \tag{5.14}$$

where

$$\tau = \frac{1000}{T}. \tag{5.15}$$

For the systematic error either b_{T3}, b_{T3} and b_{T2} or b_{T3} and b_{T2} and b_{T1} or no parameter at all was set to zero. This four fits were weighted among each other with the AIC information criteria. This gives a weight w of

$$w = e^{-\frac{1}{2}\left(\chi^2 + 2n\right)} \tag{5.16}$$

to each fit, where χ^2 is the sum of the squared difference between data and fit and n the number of parameters in the fit [217].

Then fits were performed either on lattices with $N_t = 4, 6, 8, 10$ or on lattices with $N_t = 6, 8, 10$ or only on lattices with $N_t = 8, 10$. As the AIC information criteria can only be used as long as one has always the same input data, these three groups of fits were combined with equal weights.

This gives us a total of twelve fits. The systematic error is calculated as their standard deviation. The result is the red band in 5.7.

5.1.3 Results

In this section we present the results for the topological susceptibility. In figure 5.8 we show the result for the continuum extrapolated topological susceptibility from $N_f = 3 + 1$ staggered simulations. It shows results from the direct approach up to 500 MeV, and results from the fixed sector integral method from 400 MeV. The two methods overlap nicely. It also shows the result from the dilute instanton gas approximation.

To calculate the topological susceptibility for physical quark masses, also simulations with $n_f = 2 + 1 + 1$ are needed. Figure 5.9 shows an overview over all simulations done in [7] to obtain the topological susceptibility. The final result is then shown in figure 5.10. The inset shows the region around the QCD deconfinement transition.

As described in section 3.5 the topological susceptibility can be used to estimate the mass of an axion, assuming axions are part of the dark matter. To do this estimate one needs the equation of state, which was also calculated in [7]. Finally some assumptions have to made on which amount of the dark matter was created in the misalignment mechanism described in section 3.5. If one assumes that between 1% and 50% of dark matter come from the misalignment mechanism this leads to an axion mass between 50 μeV and 1500 μeV.

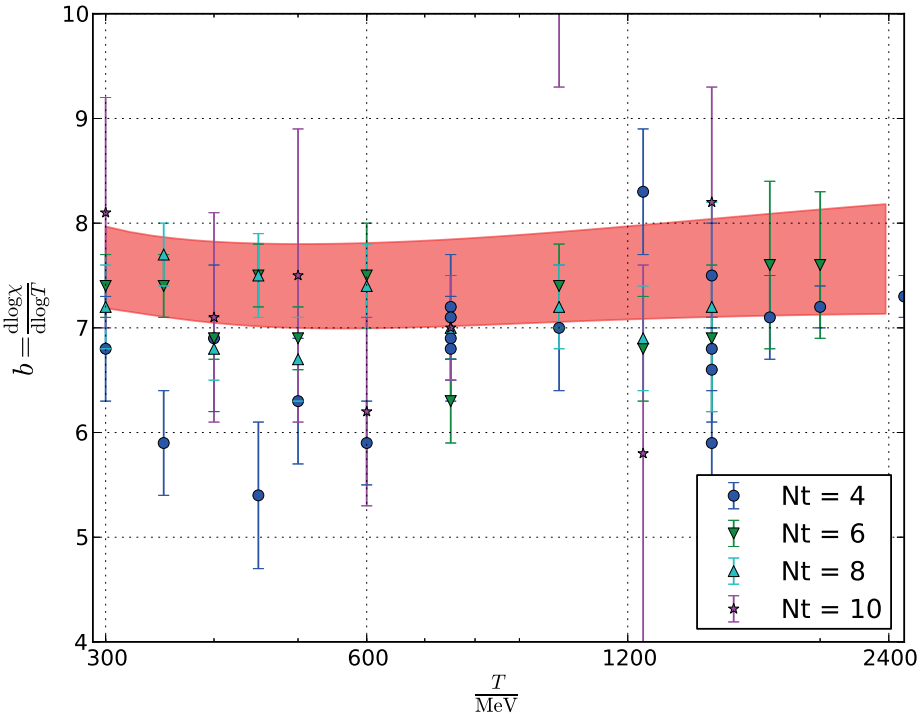

Figure 5.7: *The exponent b from $N_f = 3 + 1$ staggered simulations. The red band shows the continuum limit from $N_t = 4, 6, 8$ and 10 lattices.*

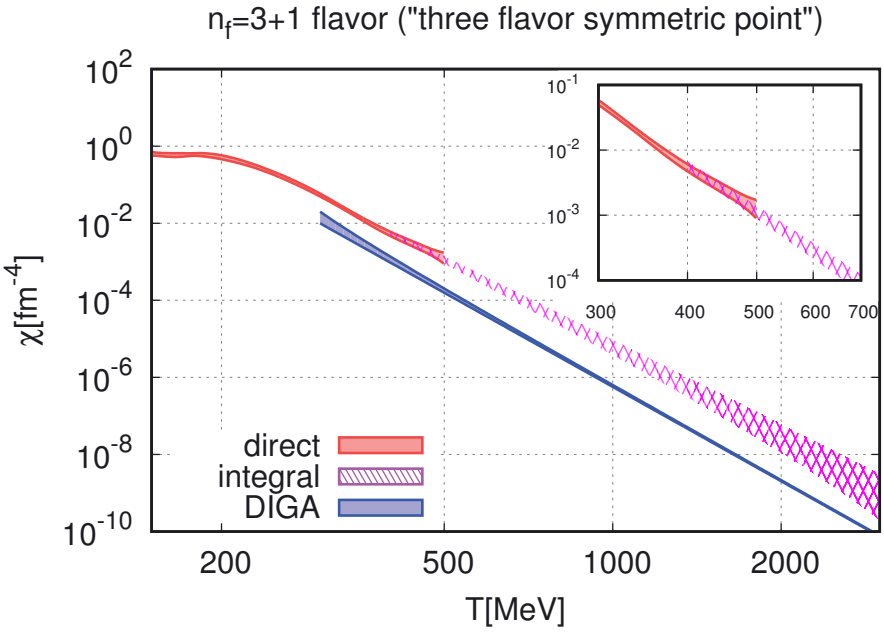

Figure 5.8: *The result for the continuum extrapolated topological susceptibility from $N_f = 3 + 1$ staggered simulations. It shows results from the direct approach up to 500 MeV, and results from the fixed sector integral method from 400 MeV. The two methods overlap nicely. It also shows the result from the dilute instanton gas approximation. [7]*

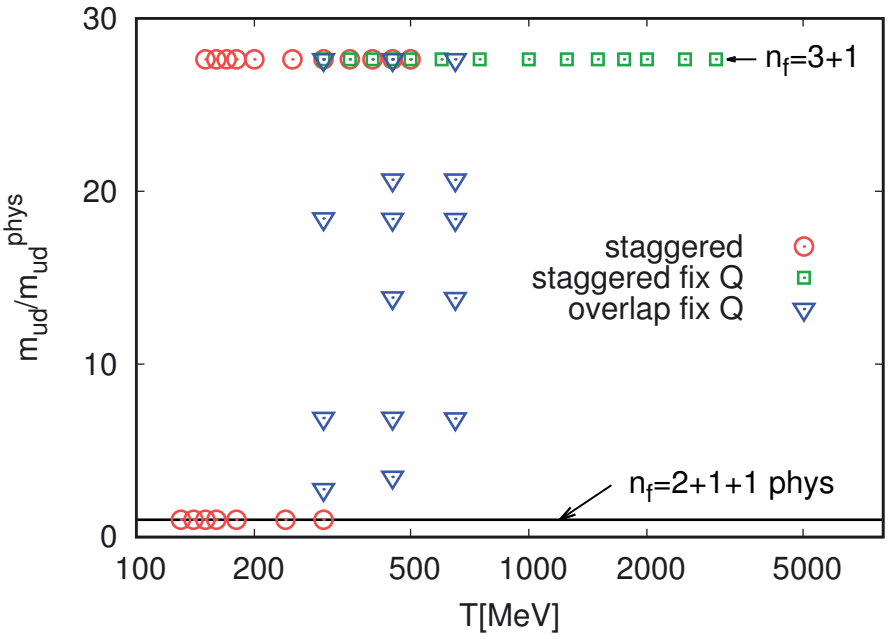

Figure 5.9: *An overview over all simulations done to obtain the topological susceptibility presented in 5.10. [7]*

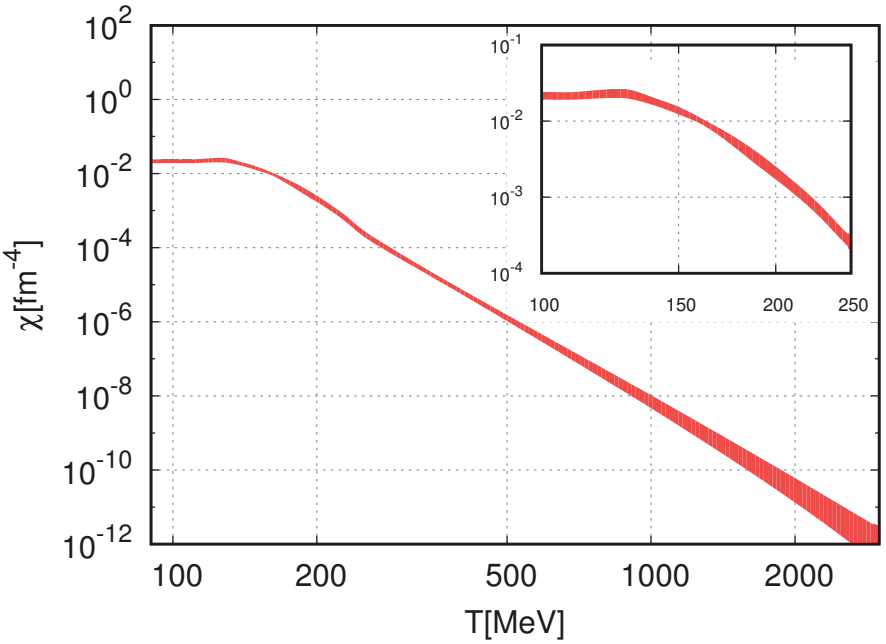

Figure 5.10: *The final result for the continuum extrapolated topological susceptibility. The enhancement shows the region around the QCD deconfinement transition. [7]*

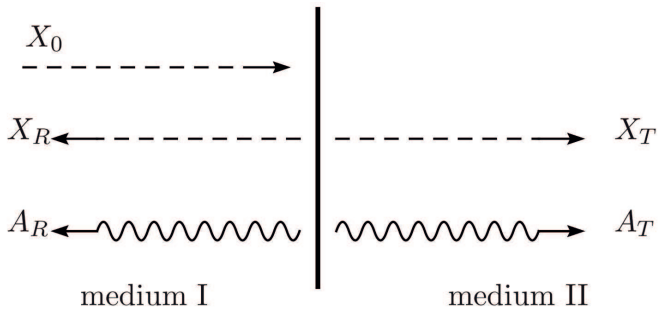

Figure 5.11: *Schematic of an axion hitting a dielectric surface [218]. The incoming axion wave X_0 leads, in addition to a reflected and a transmitted axion wave X_R and X_T, to a reflected and a transmitted photon wave A_R and A_T*

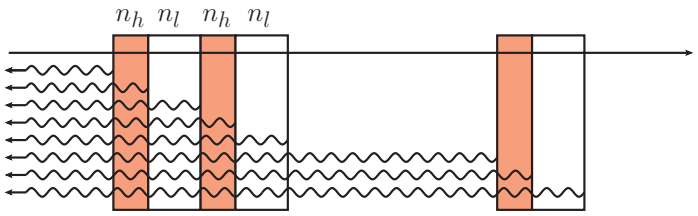

Figure 5.12: *Schematic of a dielectric mirror that is constructed to enhance the reflected photon wave [218].*

5.2 Dielectric mirror with axions

After narrowing down the mass range for axions in a possible scenario (see section 5.1), it is interesting to investigate how an experiment for axion detection might look like.

In [218] it was suggested to use a dielectric mirror. A direct mirror consist of several layers of dielectric materials that a stacked one after the other. For example one could have two materials one with a high refraction index n_h and one with low refraction index n_l that are alternating. This situation is shown in figure 5.12. On each surface there will be a transmitted and a reflected wave. The thickness of the dielectric layers can be chosen in a way that the reflected waves interfere positively, thus enhancing the reflected wave. If there is a small interaction between axions and photons, an axion hitting a dielectric surface would lead to the reflection of a photon. This is schematically shown in figure 5.11. The incoming axion wave X_0 leads, in addition to a reflected and a transmitted axion wave X_R and X_T, to a reflected and a transmitted photon wave A_R and A_T. The dielectric mirror can be used to enhance the reflected photon wave.

Since the interaction of the axion with matter is small they hardly loose any energy when passing through the dielectric mirror. Therefore it is possible to stack many dielectric layers. If they are strategically placed with a distance of half the wavelength of the photon in the respective medium, the generated photons will interfere positively, thus enhancing the photon wave enough to allow a detection. This scheme is shown in figure 5.12.

For the description of the axions as a plane wave in the framework of a classical field theory the interaction must happen sufficiently often. Therefore, to increase the interaction rate, a strong magnetic field is needed to increase the photon density until this assumption is valid [219].

To calculate the enhancement that can be achieved for this construction one can generalize the matrix formalism that is used for this kind of calculations in electrodynamics to an action which includes axions. In this section we will first shortly show the formalism for electrodynamics and than show how it can be generalized to include axions.

5.2.1 Light only

In this section we will shortly review the matrix formalism for the dielectric mirror in classical electrodynamics. Here the problem of the N layers stacked in a row is rewritten in a way that the influence of each layer can be calculated by a matrix multiplication. The presentation given here follows [220].

Electromagnetic waves are denoted by plane waves of the form

$$\vec{E} = \vec{E}_a e^{\mathrm{i}(\vec{k}\cdot\vec{x}-\omega t)}. \tag{5.17}$$

We will call the amplitude of the initial wave E_0. E_r is the amplitude of the reflected wave and E_t the amplitude of the transmitted wave. The reflection and transmission coefficints r and t are then $r = \frac{E_r}{E_0}$ and $t = \frac{E_t}{E_0}$. They can be calculated from the entries of the matrix $\widetilde{M} = \begin{pmatrix} \tilde{M}_{00} & \tilde{M}_{01} \\ \tilde{M}_{10} & \tilde{M}_{11} \end{pmatrix}$ by the equation

$$\begin{pmatrix} 1 \\ r \end{pmatrix} = \begin{pmatrix} \tilde{M}_{00} & \tilde{M}_{01} \\ \tilde{M}_{10} & \tilde{M}_{11} \end{pmatrix} \begin{pmatrix} t \\ 0 \end{pmatrix}$$

as

$$t = \frac{1}{\tilde{M}_{00}} \text{ and } r = \frac{\tilde{M}_{10}}{\tilde{M}_{00}}.$$

The matrix $\widetilde{M}$ is given as:

$$\widetilde{M} = \frac{1}{t_{0,1}} \begin{pmatrix} 1 & r_{0,1} \\ r_{0,1} & 1 \end{pmatrix} M_1 M_2 \dots M_{N-1}$$

where

$$M_n = \begin{pmatrix} e^{-i\delta_n} & 0 \\ 0 & e^{i\delta_n} \end{pmatrix} \begin{pmatrix} 1 & r_{n,n+1} \\ r_{n,n+1} & 1 \end{pmatrix} \frac{1}{t_{n,n+1}}.$$

Since the photon is massless, electrodynamic waves are transversal waves, meaning that $\vec{E} \perp \vec{k}$. This does not define the direction of $\vec{E}$ uniquely. Here we will look at two common polarisation. The first one is the s-polarisation where $\vec{E}$ is perpendicular to the plane denoted by the

incoming and the transmitted beam. The second one is p-polarisation where $\vec{E}$ is parallel to the same plane. For s-polarisation r and t are given as

$$r_{n,n+1} = \frac{n_n \cos\vartheta_n - n_{n+1}\cos\vartheta_{n+1}}{n_n \cos\vartheta_n + n_{n+1}\cos\vartheta_{n+1}} \tag{5.18}$$

$$t_{n,n+1} = \frac{2n_n \cos\vartheta_n}{n_n \cos\vartheta_n + n_{n+1}\cos\vartheta_{n+1}} \tag{5.19}$$

and for p-polarisation

$$r_{n,n+1} = \frac{n_{n+1} \cos\vartheta_n - n_n\cos\vartheta_{n+1}}{n_{n+1} \cos\vartheta_n + n_n\cos\vartheta_{n+1}} \tag{5.20}$$

$$t_{n,n+1} = \frac{2n_n \cos\vartheta_n}{n_{n+1} \cos\vartheta_n + n_n\cos\vartheta_{n+1}}. \tag{5.21}$$

Here ϑ is the angle between the incoming wave and the surface normal of the dielectric layer. The angle ϑ_{n+1} can be related to the angle ϑ_n by the Snell's law:

$$n_n \sin\vartheta_n = n_{n+1}\sin\vartheta_{n+1}$$

We can therefore calculate $\cos\vartheta_{n+1}$ as:

$$\cos\vartheta_{n+1} = \sqrt{1 - \frac{n_n^2}{n_{n+1}^2}(1-\cos^2\vartheta_n)}$$

δ_n is the product of the thickness of the layer with wave vector of the forward-travelling wave in that layer

$$\delta_n = (\text{thinkness of layer } n)(k_z \text{ for the forward} - \text{travelling wave in layer } n). \tag{5.22}$$

This yields

$$k_z = \frac{2\pi n_n \cos\vartheta_n}{\lambda_{vac}} \tag{5.23}$$

$$\delta_n = \frac{2\pi n_n \cos\vartheta_n}{\lambda_{vac}} d_n \tag{5.24}$$

With all these information it is straight forward to calculate the reflected intensity $R = |r|^2$. As an example we show R for the setup in table 5.1 in figure 5.13.

Table 5.1: *The set-up for our test calculation with* $\lambda = 550\,\text{nm}$

layer	d	n
0	-	1
1	$\frac{\lambda}{4n}$	1.38
2	$\frac{\lambda}{2n}$	2.2
3	$\frac{\lambda}{4n}$	1.96
4	-	1.5

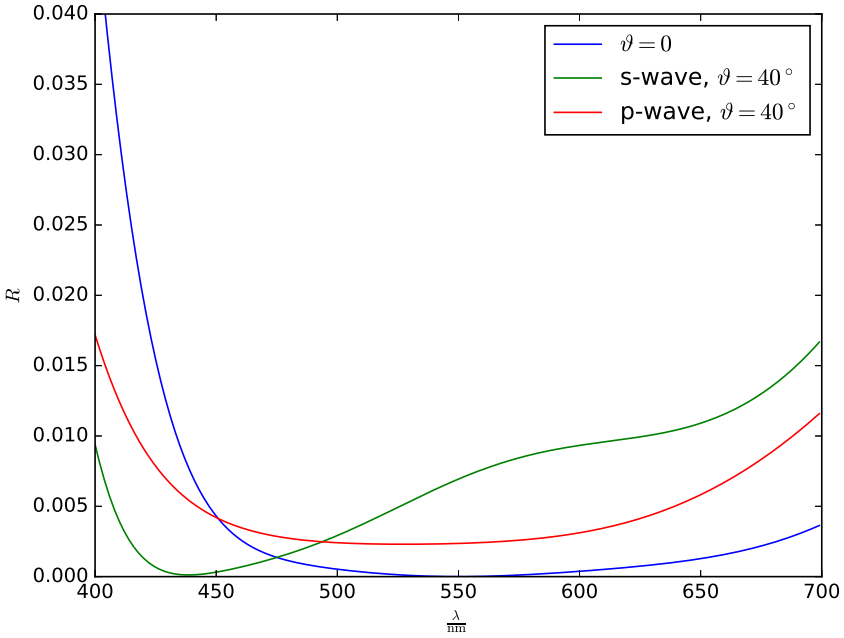

Figure 5.13: *Result for the reflected intensity $R = |r|^2$ from the set-up in table 5.1.*

5.2.2 Adding Axions

The formalism that will be used to construct a dielectric mirror for the detection of axions was introduced in [221]. It introduces a Lagrangian for an additional massive vector particle. This vector particles are another class of candidates for dark matter and are called *hidden photons* [222, 223, 224]. As we will discuss in the following the formalism that is used for the hidden photons can be easily adapted to describe axion as well. The Lagrangian that includes this hidden photons reads [221]

$$\mathcal{L} = -\frac{1}{4}F_{\mu\nu}F^{\mu\nu} - \frac{1}{4}X_{\mu\nu}X^{\mu\nu} - \frac{1}{2}\chi X^{\mu\nu}F_{\mu\nu} + \frac{m^2}{2}X_\mu X^\mu + J_\mu A^\mu. \tag{5.25}$$

Here A^μ, $F^{\mu\nu}$ and J_μ are the photon field, the field strength tensor and the charged current from ordinary electrodynamics. X^μ is the additional vector field of the hidden photon with the mass m and the respective field strength tensor

$$X^\mu = \partial^\mu X^\nu - \partial^\nu X^\mu. \tag{5.26}$$

χ is a dimensionless coupling that gives the strength of the so called kinetic mixing. The possible parameter space for χ and m is shown in figure 5.14. After a transformation $X^\mu \longrightarrow X^\mu + \chi A^\mu + \mathcal{O}(\chi^2)$ the Lagrangian can be rewritten in the flavour eigenstates and takes the from [221]

$$\mathcal{L} = -\frac{1}{4}F_{\mu\nu}F^{\mu\nu} - \frac{1}{4}X_{\mu\nu}X^{\mu\nu} + \frac{m^2}{2}\left(X_\mu - \chi A_\mu\right)\left(X^\mu - \chi A^\mu\right) + J_\mu A^\mu. \tag{5.27}$$

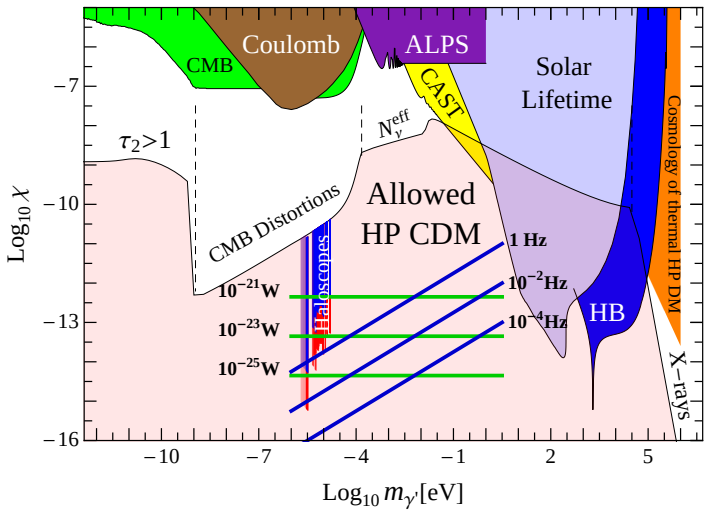

Figure 5.14: *Limits on the coupling χ and the mass m for hidden photons as presented in [218, 225]. The plot includes data from [221, 226, 227].*

Due to the mass term $\frac{m^2}{2}X_\mu X^\mu$ this Lagrangian is not gauge invariant. This can be mitigated by the Stueckelberg mechanism [228, 229] that keeps the Lagrangian invariant under some modified gauge transformation [221].

On the other hand axions are pseudo-scalar particles that couple to two photons, and can be described by the Lagrangian [225]

$$\mathcal{L} = -\frac{1}{4}F_{\mu\nu}F^{\mu\nu} + \frac{1}{2}\partial_\mu x \partial^\mu - \frac{1}{2}m_x^2 x^2 - \frac{g_{x\gamma\gamma}}{4} x F_{\mu\nu}\tilde{F}^{\mu\nu}, \tag{5.28}$$

where $g_{x\gamma\gamma}$ is the coupling strength and x is the scalar axion field with a mass m_x. The allowed parameter space for $g_{x\gamma\gamma}$ and m_x is shown in figure 5.15. It can be shown, that in the presence of an magnetic background field B this Lagrangian gives the same equation of motion as the Lagrangian in equation (5.27) with the following substitutions [218, 225]

$$A_\mu \longrightarrow A_\parallel \tag{5.29}$$

$$X_\mu \longrightarrow x \tag{5.30}$$

$$\chi \longrightarrow \frac{g_{x\gamma\gamma}B\omega}{m^2} \tag{5.31}$$

in equations (5.44) to (5.47). This can be understood in a way, that the role of X^μ is taken over by the vector field xB^μ. The coupling between the photons and the axion is maximal if the magnetic field is perpendicular to the incoming axion. If this is not the case there will be an additional factor $\sin\theta_B$ in the coupling where θ_B is the angle between the magnetic field and the incoming axion. In the following we will keep the notation from the Lagrangian of the hidden photon, keeping in mind, that it is easy to change to axion.

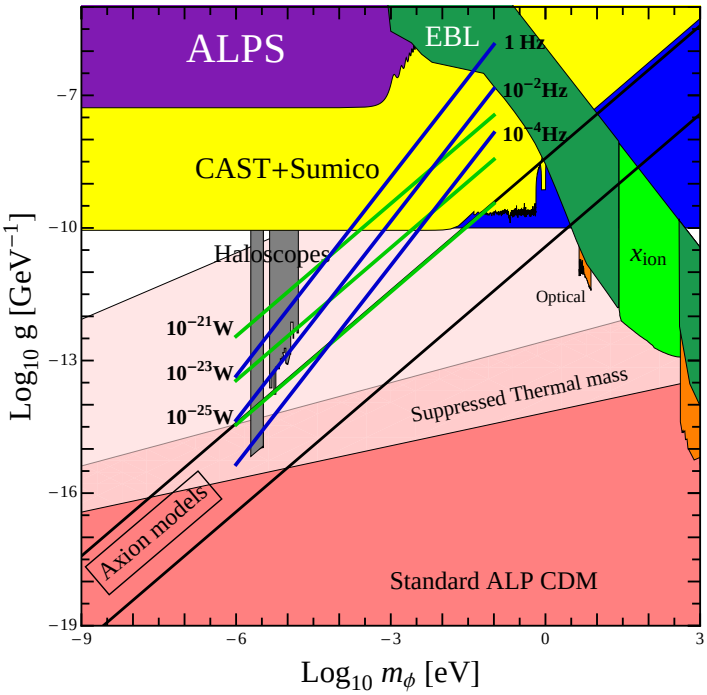

Figure 5.15: *Limits on the parameter space of $g_{x\gamma\gamma}$ and $m_x = m_\phi$ from [225]. The allowed parameter space is shon in the different shades of red.*

The next step is to add axions to the formalism described for electrodynamic waves in section 5.2.1. This will enlarge the matrices to the size of 4×4. We start from the Lagrangian for the interaction of photons and axions/HP in the form [218]

$$\mathcal{L} = -\frac{1}{4}F_{\mu\nu}F^{\mu\nu} - \frac{1}{4}X_{\mu\nu}X^{\mu\nu} + \frac{m^2}{2}(X_\mu X^\mu - 2\chi A_\mu X^\mu + \chi^2 A_\mu A^\mu),$$

neglecting for now the charged current J_μ. From this we can derive the equations of motion:

$$\partial_\rho \frac{\partial \mathcal{L}}{\partial(\partial_\rho A_\sigma)} = \frac{\partial \mathcal{L}}{\partial A_\sigma} \tag{5.32}$$

$$-\partial_\rho F^{\rho\sigma} = m^2(-\chi X^\sigma + \chi^2 A^\sigma) \tag{5.33}$$

and

$$\partial_\rho \frac{\partial \mathcal{L}}{\partial(\partial_\rho X_\sigma)} = \frac{\partial \mathcal{L}}{\partial X_\sigma} \tag{5.34}$$

$$-\partial_\rho X^{\rho\sigma} = m^2(X^\sigma - \chi A^\sigma). \tag{5.35}$$

As in [218] we use the gauge fixing $A^0 \approx X^0 \approx 0$ [230]. Now we split up the two equations in the temporal and the spacial part. For $\sigma = 0$ we get

$$\partial^0 \partial_i A^i = 0 \tag{5.36}$$

$$\partial^0 \partial_i X^i = 0 \tag{5.37}$$

and for $\sigma = j$ this yields

$$\partial^j \partial_i A^i - \partial_\rho \partial^\rho A^j = m^2(\chi^2 A^j - \chi X^j) \tag{5.38}$$
$$\partial^j \partial_i X^i - \partial_\rho \partial^\rho X^j = m^2(X^j - \chi A^j). \tag{5.39}$$

Now we use the ansatzes given in [230]. For photon like waves:

$$\begin{pmatrix} A \\ X \end{pmatrix} = \hat{A} \begin{pmatrix} 1 \\ \chi_{\text{eff}} \end{pmatrix} e^{-i(\omega t - \vec{k}\vec{x})}$$

And for axion/HP like waves:

$$\begin{pmatrix} A \\ X \end{pmatrix} = \hat{X} \begin{pmatrix} -\chi_{\text{eff}} \\ 1 \end{pmatrix} e^{-i(\omega t - \vec{p}\vec{x})}$$

Using the ansatz for A of the photon like wave we get for $\sigma = 0$:

$$\partial^0 \partial_i A^i = \partial_0 i\vec{k}\hat{A} e^{-i(\omega t - \vec{k}\vec{x})} \tag{5.40}$$
$$= \omega \vec{k} \hat{A} e^{-i(\omega t - \vec{k}\vec{x})} \tag{5.41}$$
$$= 0 \tag{5.42}$$

Since $w \neq 0 \Rightarrow \vec{k}\hat{A} = 0$. This means that A is a transversal wave. For $\sigma = j$ on the other hand we have the equation

$$-(-\omega^2 + \vec{k}^2)A^j = m^2(\chi^2 A^j - \chi X^j). \tag{5.43}$$

Analogously we get the for X :

$$-(-\omega^2 + \vec{k}^2)X^j \;\; = \; m^2(X^j - \chi A^j)$$

X has to be a transversal wave as well. Repeating the calculation for the axion/HP like waves, we obtain four equations to determine $\vec{k}$, $\vec{p}$ and χ_{eff}:

$$(\omega^2 - k^2) - M^2 - m^2(\chi^2 - \chi\chi_{eff}) = 0 \tag{5.44}$$
$$(\omega^2 - k^2)\chi_{eff} - m^2(-\chi + \chi_{eff}) = 0 \tag{5.45}$$
$$-(\omega^2 - p^2)\chi_{eff} + M^2\chi_{eff} + m^2(\chi^2\chi_{eff} + \chi) = 0 \tag{5.46}$$
$$\omega^2 - p^2 - m^2(\chi\chi_{eff} + 1) = 0 \tag{5.47}$$

Here $M = \omega^2(1 - n^2)$ has been introduced to describe the interaction of the photons with matter. This yields:

$$\chi_{eff} = \chi \frac{m^2}{m^2 - M^2} \tag{5.48}$$
$$p^2 = \omega^2 - m^2(\chi\chi_{eff} + 1) \tag{5.49}$$
$$k^2 = \omega^2 - M^2 - m^2(\chi^2 - \chi\chi_{eff}) \tag{5.50}$$

χ_{eff} can be derived consistently both from equation (5.44) and (5.45) and from equation (5.46) and (5.47), up to first order in χ.

We choose our coordinate system in a way that the dielectric layer is in the $y = 0$ plane and we want the waves and its first derivative with respect to y to be continous at this plane. We assume for now that the axion enters the dielectric mirror perpendicular to the dielectric mirror. We get the following set of equations:

$$X_0 \begin{pmatrix} -\chi_1 \\ 1 \end{pmatrix} e^{-i\omega t} + X_R \begin{pmatrix} -\chi_1 \\ 1 \end{pmatrix} e^{-i\omega t} \tag{5.51}$$

$$+A_0 \begin{pmatrix} 1 \\ \chi_1 \end{pmatrix} e^{-i\omega t} + A_R \begin{pmatrix} 1 \\ \chi_1 \end{pmatrix} e^{-i\omega t} \tag{5.52}$$

$$=X_T \begin{pmatrix} -\chi_2 \\ 1 \end{pmatrix} e^{-i\omega t} + A_T \begin{pmatrix} 1 \\ \chi_2 \end{pmatrix} e^{-i\omega t} \tag{5.53}$$

and

$$p_1 X_0 \begin{pmatrix} -\chi_1 \\ 1 \end{pmatrix} e^{-i\omega t} - p_1 X_R \begin{pmatrix} -\chi_1 \\ 1 \end{pmatrix} e^{-i\omega t} \tag{5.54}$$

$$+k_1 A_0 \begin{pmatrix} 1 \\ \chi_1 \end{pmatrix} e^{-i\omega t} - k_1 A_R \begin{pmatrix} 1 \\ \chi_1 \end{pmatrix} e^{-i\omega t} \tag{5.55}$$

$$=p_2 X_T \begin{pmatrix} -\chi_2 \\ 1 \end{pmatrix} e^{-i\omega t} + k_2 A_T \begin{pmatrix} 1 \\ \chi_2 \end{pmatrix} e^{-i\omega t} \tag{5.56}$$

Since this equations have to hold for every t from now on, we will use $t = 0$.

However there is one difficulty. We get $p_1 \ll k_1$ from $\omega \approx m$. If we set $\omega = m$ and look at the equation for p we get:

$$p^2 = \omega^2 - m^2(\chi\chi_{eff} + 1) \tag{5.57}$$

$$\approx m^2 - m^2(\chi\chi_{eff} + 1) \tag{5.58}$$

$$= -m^2\chi\chi_{eff} < 0 \tag{5.59}$$

This makes or p very small but imaginary. Since k is real this means that there is no reflection of the light. However if we choose our m slightly smaller than ω nothing like this will happen. For the following pictures we set $\omega = \frac{m}{1+10^{-6}}$.

Now we can solve the system of linear equations for $\frac{X_T}{X_0}$, $\frac{X_R}{X_0}$, $\frac{A_T}{X_0}$ and $\frac{A_R}{X_0}$ for given $\frac{A_0}{X_0}$. Since the system is linear, this could be done analytically. However since the equations are quite lengthy for this work the system was solved numerically. From this solution we can get the matrices t and r that are chosen in a way that

$$\begin{pmatrix} X_T \\ A_T \end{pmatrix} = t \begin{pmatrix} X_0 \\ A_0 \end{pmatrix} \tag{5.60}$$

and

$$\begin{pmatrix} X_R \\ A_R \end{pmatrix} = r \begin{pmatrix} X_0 \\ A_0 \end{pmatrix}. \tag{5.61}$$

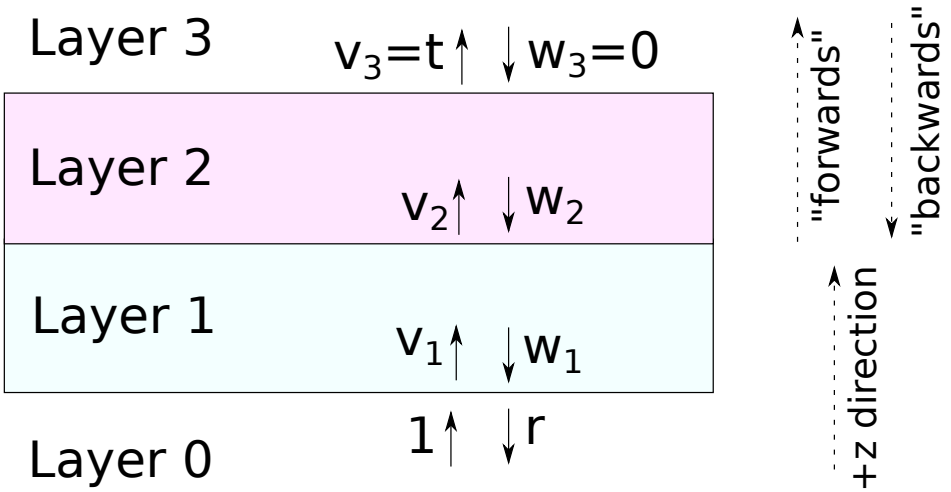

Figure 5.16: *Illustration of the waves moving forward and backward in each layer.[220]*

This implies that r and t are now matrices of size 2×2.

As a next step we need to determine what happens to a wave that passes from a layer n to the next layer $n+1$. Each wave consists of a forward moving part v_i and a backward moving part w_i. Each wave has an axion part and a photon part. If $t_{n,n+1}$ is the transition matrix from layer n to $n+1$ and $r_{n,n+1}$ the corresponding reflection matrix, we can use the illustration in figure 5.16 from [220] to determine

$$v_{n+1} = t_{n,n+1} v_n e^{\mathrm{i}\delta_n} + r_{n+1,n} w_{n+1} \tag{5.62}$$

$$w_n = e^{\mathrm{i}\delta_n} \left(t_{n+1,n} w_{n+1} + r_{n,n+1} e^{\mathrm{i}\delta_n} v_n \right) \tag{5.63}$$

where

$$\delta_n = \begin{pmatrix} p_n d_n \cos\vartheta_n & 0 \\ 0 & k_n d_n \cos\varphi_n \end{pmatrix} \tag{5.64}$$

with d_n being the thickness of the nth layer. This equations are constructed analogously to the calculation in [220]. However we have to keep in mind that r and t are now matrices instead of numbers. We then can solve this equation for v_n and w_n yielding

$$\begin{pmatrix} v_n \\ w_n \end{pmatrix} = \begin{pmatrix} e^{-\mathrm{i}\delta_n} & 0 \\ 0 & e^{\mathrm{i}\delta_n} \end{pmatrix} \begin{pmatrix} t^{-1}_{n,n+1} & -t^{-1}_{n,n+1} r_{n+1,n} \\ r_{n,n+1} t^{-1}_{n,n+1} & t_{n+1,n} - r_{n,n+1} t^{-1}_{n,n+1} r_{n+1,n} \end{pmatrix} \begin{pmatrix} v_{n+1} \\ w_{n+1} \end{pmatrix}. \tag{5.65}$$

Now we can read of the matrix M_n as

$$M_n = \begin{pmatrix} e^{-\mathrm{i}\delta_n} & 0 \\ 0 & e^{\mathrm{i}\delta_n} \end{pmatrix} \begin{pmatrix} t^{-1}_{n,n+1} & -t^{-1}_{n,n+1} r_{n+1,n} \\ r_{n,n+1} t^{-1}_{n,n+1} & t_{n+1,n} - r_{n,n+1} t^{-1}_{n,n+1} r_{n+1,n} \end{pmatrix} \tag{5.66}$$

and as before

$$\tilde{M} = M_0 M_1 \dots M_{N-1} \tag{5.67}$$

where we set $\delta_0 = 0$. This allows us to write

$$\begin{pmatrix} 1 \\ 0 \\ r_X \\ r_A \end{pmatrix} = \tilde{M} \begin{pmatrix} t_X \\ t_A \\ 0 \\ 0 \end{pmatrix} \tag{5.68}$$

with r_X and r_A being the reflected amount of the axion and the photon wave and t_X and t_A being the transmitted amount. Solving equation (5.68) yields

$$t_X = \frac{1}{\tilde{M}_{00} - \frac{\tilde{M}_{01}\tilde{M}_{10}}{\tilde{M}_{11}}} \tag{5.69}$$

$$t_A = -\frac{\tilde{M}_{10}}{\tilde{M}_{11}} t_X \tag{5.70}$$

$$r_X = \tilde{M}_{20} t_X + \tilde{M}_{21} t_A \tag{5.71}$$

$$r_A = \tilde{M}_{30} t_X + \tilde{M}_{31} t_A. \tag{5.72}$$

From this we finally get the reflected intensity of the photon wave as

$$R_A = |r_A|^2. \tag{5.73}$$

5.3 Results

In this section we are going to show some results gained from the calculation above, which might be useful for a possible experiment. In our example we use a frequency for the axion of $\omega = 60$ μeV and N layers of a medium with $n = 3.2$, which could be sapphire, alternating with air, where $n = 1$.

We start by calculating the amplification that comes from having N layers compared to a single layer, when the incoming axion is perpendicular to the medium's surface. In figure 5.17 we can see that the amplification rises with the number of layers. We also see that the maximum amplification is reached at the mass for which the construction is obtimized for, in our case $m \approx 60$ μeV. There the amplification is given by N^2 as already determined in [218]. We can also see that the peak gets narrower for an increasing number of layers. Therefore it is interesting to look at the integral of the peak. We integrated over a mass range between 56 μeV and 70 μeV and normalized the integral to the integral of the peak for a dielectric mirror with one layer. As it can be seen in figure 5.18, the integral rises linear with the numbers of layers. Since in an experiment one will have to scan a large mass range for the axions one has to find a compromise between a wider peak, that allows to scan for more masses at the same time and a large number of plates that increases the intensity.

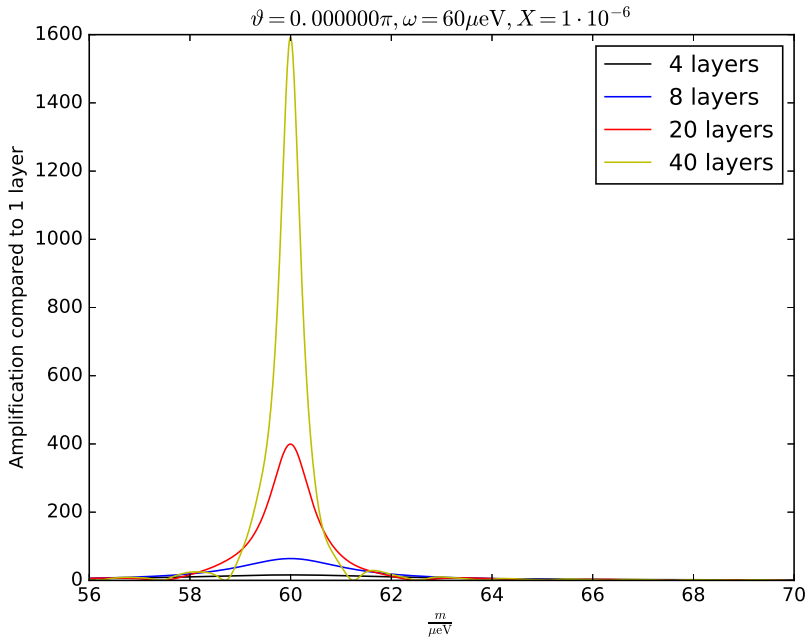

Figure 5.17: *The amplification compared to a single layer at* $\vartheta = 0$

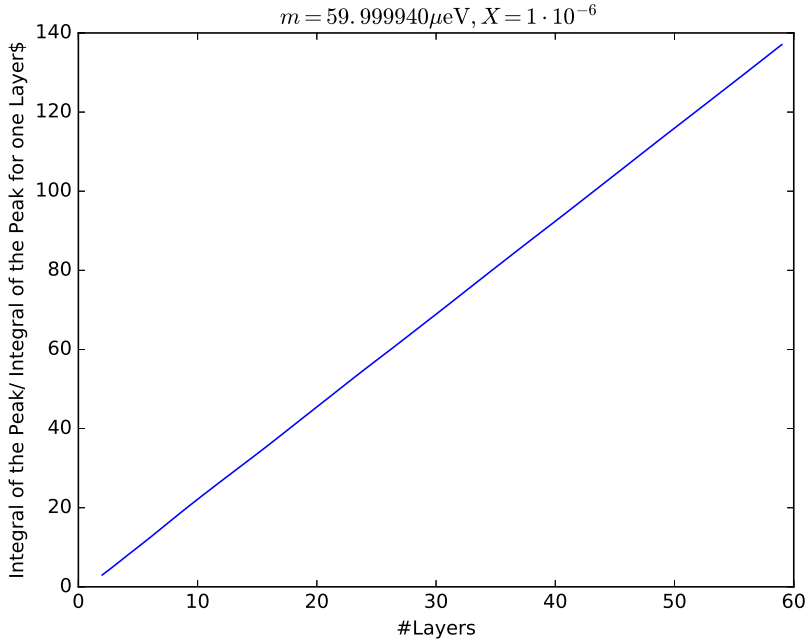

Figure 5.18: *The integral over the peak for different number of layers in the dielectric mirror. The integration range was chosen to be between 56* μeV *and 70* μeV

6 Conclusion and outlook

The understanding of the early universe and the investigation of dark matter are fascinating topics. In this thesis a small step in both areas was made. The first part of this thesis investigated the QCD phase diagram at finite baryon chemical potential with lattice QCD. Since this can not be done directly due to the sign problem, we used simulations at imaginary baryon chemical potential to extrapolate to real chemical potential. An extrapolation up to $\mu_B \approx 400$ MeV was possible. All simulations were done at the strangeness neutral point to match conditions in heavy ion collision experiments.

First the cross over temperature was investigated. It was determined from three main observables: the chiral susceptibility $\chi_{\bar{\psi}\psi}$, the chiral condensate $\bar{\psi}\psi$ and several definitions of the strange susceptibility χ_{SS}. The crossover temperature was defined as the position of the maximum for the peak like observable $\chi_{\bar{\psi}\psi}$ and as the point of inflection for the observable that show a sigmoid like shape $\bar{\psi}\psi$ and χ_{SS}. For the curvature of the cross over line we determined a value of

$$\kappa = 0.0149 \pm 0.0021. \tag{6.1}$$

We also investigated the equation of state. We determined the Taylor coefficients of the pressure up to $\mathcal{O}(\mu_B^6)$ in the continuum limit. We then calculated the pressure and the trace anomaly along the isentropic trajectories. The trajectories were matched to the RHIC beam energies.

In principal it would be straight forward to enhance this calculations by increasing the statics or adding simulations at different values for the imaginary chemical potential. One might then be able to extrapolate further in the realm of positive chemical potential. However before this is done, the position of the critical end point should be determined to check whether a further extrapolation is actually useful. There are other calculations that might be done on the same data set, though. For example it might be interesting to calculate some fluctuations to determine not only the cross over but also a freeze-out curve.

In the second part of this thesis some calculations were presented that investigate the axion as a possible dark matter candidate. As a first step the topological susceptibility was computed. Since this is a quantity that is difficult to measure on the lattice two methods to enhance the computations, the eigenvalue reweighting technique and the fixed sector integral method, were described. The topological susceptibility together with the equation of state allow for an estimate of the axion mass, if one assumes that a given amount of the dark matter consists of axions that were produced in the misalignment mechanism. This leads to an estimate for the axion mass between 50 μeV and 1500 μeV. This is still a large range that might prove difficult to cover in an experiment. Therefore a further enhancement of this computations would be helpful.

As a second step an aspects of an experimental setup to detect potential axions was introduced, based on the idea of a dielectric mirror that reflects photons while an axion passes through it. In this thesis some first computations for the properties of such a dielectric mirror were performed. The enhancement depending on the number of plates has been investigated. The next steps would be to allow axions that enter from different angles and to compute the influence of defects in the material or the positioning of the plates.

Bibliography

[1] Jülich Supercomputing Centre, *Juqueen: Ibm blue gene/q supercomputer system at the jülich supercomputing centre*, *Journal of large-scale research facilities* **A1** (2015) 1.

[2] A. Linde, *Elementarteilchen und inflationärer Kosmos*. Spektrum Akademischer Verlag, 1990.

[3] A. D. Linde, *Phase Transitions in Gauge Theories and Cosmology*, *Rept.Prog.Phys.* **42** (1979) 389.

[4] V. A. R. Dmitry S. Gorbunov, *Introduction to the Theory of the Early Universe-Hot Big Bang Thory*. World Scientific, 2011.

[5] R. Bellwied, S. Borsanyi, Z. Fodor, J. Günther, S. D. Katz, C. Ratti et al., *The QCD phase diagram from analytic continuation*, *Phys. Lett.* **B751** (2015) 559–564, [1507.07510].

[6] J. Gunther, R. Bellwied, S. Borsanyi, Z. Fodor, S. D. Katz, A. Pasztor et al., *The QCD equation of state at finite density from analytical continuation*, 1607.02493.

[7] S. Borsanyi et al., *Calculation of the axion mass based on high-temperature lattice quantum chromodynamics*, *Nature* **539** (2016) 69–71, [1606.07494].

[8] J. Noronha-Hostler, R. Bellwied, J. Gunther, P. Parotto, A. Pasztor, I. P. Vazquez et al., *Kaon fluctuations from lattice QCD*, 1607.02527.

[9] S. Borsanyi, *Frontiers of finite temperature lattice field theory*, in *Quark confinement and the hadron spectrum*, 2016.

[10] A. Challinor, *CMB anisotropy science: a review*, *IAU Symp.* **288** (2013) 42, [1210.6008].

[11] Y. Aoki, Z. Fodor, S. D. Katz and K. K. Szabo, *The QCD transition temperature: Results with physical masses in the continuum limit*, *Phys. Lett.* **B643** (2006) 46–54, [hep-lat/0609068].

[12] Y. Aoki, S. Borsanyi, S. Durr, Z. Fodor, S. D. Katz, S. Krieg et al., *The QCD transition temperature: results with physical masses in the continuum limit II.*, *JHEP* **06** (2009) 088, [0903.4155].

[13] Wuppertal-Budapest collaboration, S. Borsanyi, Z. Fodor, C. Hoelbling, S. D. Katz, S. Krieg, C. Ratti et al., *Is there still any T_c mystery in lattice QCD? Results with physical masses in the continuum limit III*, *JHEP* **09** (2010) 073, [1005.3508].

[14] D. A. Kirzhnits and A. D. Linde, *Macroscopic Consequences of the Weinberg Model*, *Phys. Lett.* **B42** (1972) 471–474.

[15] J. Heitger, "Numerical Simulations of Gauge-Higgs Models on the Lattice." 1997.

[16] S. Durr et al., *Ab-Initio Determination of Light Hadron Masses*, *Science* **322** (2008) 1224–1227, [0906.3599].

[17] *https://blog.higgshunters.org/2014/11/28/introduction-to-particle-physics-part-3-order-from-chaos-the-standard-model-arrives/*, October, 2016.

[18] SNO collaboration, Q. R. Ahmad et al., *Direct evidence for neutrino flavor transformation from neutral current interactions in the Sudbury Neutrino Observatory*, *Phys. Rev. Lett.* **89** (2002) 011301, [nucl-ex/0204008].

[19] Super-Kamiokande collaboration, Y. Fukuda et al., *Evidence for oscillation of atmospheric neutrinos*, *Phys. Rev. Lett.* **81** (1998) 1562–1567, [hep-ex/9807003].

[20] P. W. Higgs, *Broken symmetries, massless particles and gauge fields*, *Phys. Lett.* **12** (1964) 132–133.

[21] P. W. Higgs, *Broken Symmetries and the Masses of Gauge Bosons*, *Phys. Rev. Lett.* **13** (1964) 508–509.

[22] P. W. Higgs, *Spontaneous Symmetry Breakdown without Massless Bosons*, *Phys. Rev.* **145** (1966) 1156–1163.

[23] F. Englert and R. Brout, *Broken Symmetry and the Mass of Gauge Vector Mesons*, *Phys. Rev. Lett.* **13** (1964) 321–323.

[24] G. S. Guralnik, C. R. Hagen and T. W. B. Kibble, *Global Conservation Laws and Massless Particles*, *Phys. Rev. Lett.* **13** (1964) 585–587.

[25] G. Aad et al., *Observation of a new particle in the search for the standard model higgs boson with the ATLAS detector at the LHC*, *Physics Letters B* **716** (2012) 1 – 29.

[26] S. Chatrchyan et al., *Observation of a new boson at a mass of 125 gev with the CMS experiment at the LHC*, *Physics Letters B* **716** (2012) 30 – 61.

[27] C. Gattringer and C. B. Lang, *Quantum Chromodynamics on the Lattice - An Introductory Presentation*, in *Lecture Notes in Physics*, vol. 788. Springer, 2010.

[28] D. V. S. Michael E. Peskin, *An Introduction to Quantum Field Theory*. ABP Westview Press, 1995.

[29] L.-F. L. Ta-Pei Cheng, *Gauge theory of elementary particle physics*. Oxford university press, 1984.

[30] T. Muta, *Foundations of Quantum Chromodynamics*. World Scientific, 1987.

[31] D. V. S. Michael E. Peskin, *An Introduction to Quantum Field Theory*. Westerview Press, 1995.

[32] C. A. Baker et al., *An Improved experimental limit on the electric dipole moment of the neutron*, *Phys. Rev. Lett.* **97** (2006) 131801, [hep-ex/0602020].

[33] M. S. T. Edward W. Kolb, *The Early Universe*. Addison-Wesley publishing company, 1990.

[34] S. Borsanyi et al., *Ab initio calculation of the neutron-proton mass difference*, *Science* **347** (2015) 1452–1455, [1406.4088].

[35] J. Smit, *Introduction to Quantum Fields on a Lattice*. Cambridge University Press, 2002.

[36] G. P. Lepage, *Lattice QCD for novices*, in *Strong interactions at low and intermediate energies. Proceedings, 13th Annual Hampton University Graduate Studies, HUGS'98, Newport News, USA, May 26-June 12, 1998*, pp. 49–90, 1998. hep-lat/0506036.

[37] C. Davies, *Lattice QCD*, in *Heavy flavor physics: Theory and experimental results in heavy quark physics and CP violation. Proceedings, 55th Scottish Universities Summer School in Physics, SUSSP 2001, St. Andrews, UK, August 7-23, 2001*, pp. 105–146, 2002. hep-ph/0205181.

[38] A. Wipf, *Statistical approach to quantum field theory*, *Lect.Notes Phys.* **864** (2013) .

[39] K. Symanzik, *Continuum Limit and Improved Action in Lattice Theories. 1. Principles and phi**4 Theory*, *Nucl. Phys.* **B226** (1983) 187–204.

[40] K. Symanzik, *Continuum Limit and Improved Action in Lattice Theories. 2. O(N) Nonlinear Sigma Model in Perturbation Theory*, *Nucl. Phys.* **B226** (1983) 205–227.

[41] M. Luscher and P. Weisz, *On-Shell Improved Lattice Gauge Theories*, *Commun. Math. Phys.* **97** (1985) 59.

[42] T. Kurth, *Precision Physics from the Lattice-Calculation of the Hadron Spectrum, Quark Masses and Kaon Bag Parameter*. PhD thesis, Bergische Universität Wuppertal, 2011.

[43] H. B. Nielsen and M. Ninomiya, *No Go Theorem for Regularizing Chiral Fermions*, *Phys. Lett.* **B105** (1981) 219–223.

[44] H. B. Nielsen and M. Ninomiya, *Absence of Neutrinos on a Lattice. 1. Proof by Homotopy Theory*, *Nucl. Phys.* **B185** (1981) 20.

[45] H. B. Nielsen and M. Ninomiya, *Absence of Neutrinos on a Lattice. 2. Intuitive Topological Proof*, *Nucl. Phys.* **B193** (1981) 173–194.

[46] L. Varnhorst, *Der Chirale Phasenübergang in $N_f = 6$-QCD*, Master's thesis, Bergische Universität Wuppertal, 2013.

[47] WHOT-QCD collaboration, T. Umeda, S. Ejiri, R. Iwami and K. Kanaya, *Towards the QCD equation of state at the physical point using Wilson fermion*, *PoS* **LATTICE2015** (2016) 209, [1511.04649].

[48] H. Neuberger, *Exactly massless quarks on the lattice*, *Phys. Lett.* **B417** (1998) 141–144, [hep-lat/9707022].

[49] P. H. Ginsparg and K. G. Wilson, *A Remnant of Chiral Symmetry on the Lattice*, *Phys. Rev.* **D25** (1982) 2649.

[50] N. Metropolis, A. W. Rosenbluth, M. N. Rosenbluth, A. H. Teller and E. Teller, *Equation of state calculations by fast computing machines*, *J. Chem. Phys.* **21** (1953) 1087–1092.

[51] N. Cabibbo and E. Marinari, *A New Method for Updating SU(N) Matrices in Computer Simulations of Gauge Theories*, *Phys. Lett.* **B119** (1982) 387–390.

[52] D. Barkai, K. J. M. Moriarty and C. Rebbi, *A Modified Conjugate Gradient Solver for Very Large Systems*, *Comput. Phys. Commun.* **36** (1985) 1.

[53] S. L. B. Moshier, *Methods and programs for mathematical functions*. Ellis Horwood Limited, 1989.

[54] S. Capitani, *Lattice Perturbation Theory*, .

[55] D. J. Gross and F. Wilczek, *Ultraviolet Behavior of Nonabelian Gauge Theories*, *Phys. Rev. Lett.* **30** (1973) 1343–1346.

[56] H. D. Politzer, *Reliable Perturbative Results for Strong Interactions?*, *Phys. Rev. Lett.* **30** (1973) 1346–1349.

[57] D. R. T. Jones, *Two Loop Diagrams in Yang-Mills Theory*, *Nucl. Phys.* **B75** (1974) 531.

[58] W. E. Caswell, *Asymptotic Behavior of Nonabelian Gauge Theories to Two Loop Order*, *Phys. Rev. Lett.* **33** (1974) 244.

[59] K. G. Wilson, *Confinement of Quarks*, *Phys. Rev.* **D10** (1974) 2445–2459.

[60] M. Creutz, *Monte Carlo Study of Quantized SU(2) Gauge Theory*, *Phys. Rev.* **D21** (1980) 2308–2315.

[61] M. Creutz, *Confinement and the Critical Dimensionality of Space-Time*, *Phys. Rev. Lett.* **43** (1979) 553–556.

[62] J. Kuti, J. Polonyi and K. Szlachanyi, *Monte Carlo Study of SU(2) Gauge Theory at Finite Temperature*, *Phys.Lett.* **B98** (1981) 199.

[63] L. D. McLerran and B. Svetitsky, *A Monte Carlo Study of SU(2) Yang-Mills Theory at Finite Temperature*, *Phys. Lett.* **B98** (1981) 195.

[64] J. Engels, F. Karsch, H. Satz and I. Montvay, *High Temperature SU(2) Gluon Matter on the Lattice*, *Phys. Lett.* **B101** (1981) 89.

[65] L. G. Yaffe and B. Svetitsky, *First Order Phase Transition in the SU(3) Gauge Theory at Finite Temperature*, *Phys. Rev.* **D26** (1982) 963.

[66] J. B. Kogut, H. Matsuoka, M. Stone, H. W. Wyld, S. H. Shenker, J. Shigemitsu et al., *Quark and Gluon Latent Heats at the Deconfinement Phase Transition in SU(3) Gauge Theory*, *Phys. Rev. Lett.* **51** (1983) 869.

[67] F. Karsch and R. Petronzio, *Gluon Thermodynamics Near the Continuum Limit*, *Phys. Lett.* **B139** (1984) 403–407.

[68] A. Kennedy and B. Pendleton, *Improved Heat Bath Method for Monte Carlo Calculations in Lattice Gauge Theories*, *Phys.Lett.* **B156** (1985) 393–399.

[69] Z. Fodor and K. Jansen, *Overrelaxation algorithm for coupled gauge Higgs systems*, *Phys.Lett.* **B331** (1994) 119–123, [hep-lat/9403024].

[70] Z. Fodor, J. Hein, K. Jansen, A. Jaster and I. Montvay, *Simulating the electroweak phase transition in the SU(2) Higgs model*, *Nucl.Phys.* **B439** (1995) 147–186, [hep-lat/9409017].

[71] S. Duane, A. D. Kennedy, B. J. Pendleton and D. Roweth, *Hybrid Monte Carlo*, *Phys. Lett.* **B195** (1987) 216–222.

[72] P. Bacilieri et al., *On the Order of the Deconfining Phase Transition in Pure Gauge QCD*, *Phys. Rev. Lett.* **61** (1988) 1545–1548.

[73] F. R. Brown, N. H. Christ, Y. F. Deng, M. S. Gao and T. J. Woch, *Nature of the Deconfining Phase Transition in SU(3) Lattice Gauge Theory*, *Phys. Rev. Lett.* **61** (1988) 2058.

[74] A. Ukawa, *QCD PHASE TRANSITIONS AT FINITE TEMPERATURES*, *Nucl. Phys. Proc. Suppl.* **17** (1990) 118–136.

[75] M. Fukugita, H. Mino, M. Okawa and A. Ukawa, *Finite size study of the finite temperature chiral phase transition in QCD with light quarks*, *Nucl. Phys. Proc. Suppl.* **20** (1991) 258–262.

[76] A. Vaccarino, *The Flavor dependence of the QCD finite temperature phase transition*, *Nucl. Phys. Proc. Suppl.* **20** (1991) 263–267.

[77] P. F. Hsieh, *FULL QCD ON AN 8**3 x 2 LATTICE*, *Nucl. Phys. Proc. Suppl.* **17** (1990) 239–242.

[78] J. B. Kogut and D. K. Sinclair, *Pressures, Energy Densities and Chiral Condensates in SU(3) Lattice Gauge Theory With Dynamical Fermions*, *Nucl. Phys.* **B344** (1990) 238–254.

[79] S. A. Gottlieb, W. Liu, R. L. Renken, R. L. Sugar and D. Toussaint, *Hadron Masses with Two Quark Flavors*, *Phys. Rev.* **D38** (1988) 2245.

[80] S. A. Gottlieb, W. Liu, R. L. Renken, R. L. Sugar and D. Toussaint, *QCD Thermodynamics With Eight Time Slices*, *Phys. Rev.* **D41** (1990) 622.

[81] MT(c) collaboration, R. V. Gavai, S. Gupta, A. Irback, F. Karsch, S. Meyer, B. Petersson et al., *The Finite Temperature Phase Transition in Four Flavor QCD on an 8 X 12^3 Lattice*, *Phys. Lett.* **B232** (1989) 491–497.

[82] G. Boyd, J. Engels, F. Karsch, E. Laermann, C. Legeland, M. Lutgemeier et al., *Equation of state for the SU(3) gauge theory*, *Phys. Rev. Lett.* **75** (1995) 4169–4172, [hep-lat/9506025].

[83] K. Kanaya, *Finite temperature QCD on the lattice*, *Nucl. Phys. Proc. Suppl.* **47** (1996) 144–159, [hep-lat/9510040].

[84] Y. Iwasaki, K. Kanaya, S. Kaya, S. Sakai and T. Yoshie, *QCD phase transition with strange quark in Wilson formalism for fermions*, *Z. Phys.* **C71** (1996) 343–346, [hep-lat/9505017].

[85] C. W. Bernard et al., *The hot QCD equation of state from lattice simulations*, in *DPF '96, The Minneapolis Meeting: Proceedings of the 9th Meeting of the Division of Particles and Fields of the American Physical Society, Twin City Campus, University of Minnesota, Minneapolis, 11-15 August 1996*, pp. 1156–1158, 1996.

[86] J. B. Kogut, M. P. Lombardo and D. K. Sinclair, *Quenched QCD at finite density*, *Phys. Rev.* **D51** (1995) 1282–1291, [hep-lat/9401039].

[87] W. Wilcox, S. Trendafilov and E. Mendel, *Finite density results for Wilson fermions using the volume method*, *Nucl. Phys. Proc. Suppl.* **42** (1995) 557, [hep-lat/9501011].

[88] JLQCD, CP-PACS collaboration, A. Ukawa, *Computational cost of full QCD simulations experienced by CP-PACS and JLQCD Collaborations*, *Nucl. Phys. Proc. Suppl.* **106** (2002) 195–196.

[89] K. Jansen, *Lattice QCD: A Critical status report*, *PoS* **LATTICE2008** (2008) 010, [0810.5634].

[90] K. Jansen, A. Shindler, C. Urbach and U. Wenger, *HMC algorithm with multiple time scale integration and mass preconditioning*, *PoS* **LAT2005** (2006) 118, [hep-lat/0510064].

[91] Z. Fodor and S. Katz, "The Phase diagram of quantum chromodynamics." 2009.

[92] H. B. Meyer, *QCD at non-zero temperature from the lattice*, *PoS* **LATTICE2015** (2016) 014, [1512.06634].

[93] P. Hasenfratz and F. Karsch, *Chemical Potential on the Lattice*, *Phys. Lett.* **B125** (1983) 308–310.

[94] I. M. Barbour, S. E. Morrison, E. G. Klepfish, J. B. Kogut and M.-P. Lombardo, *Results on finite density QCD*, *Nucl. Phys. Proc. Suppl.* **60A** (1998) 220–234, [hep-lat/9705042].

[95] Z. Fodor and S. D. Katz, *A New method to study lattice QCD at finite temperature and chemical potential*, *Phys. Lett.* **B534** (2002) 87–92, [hep-lat/0104001].

[96] Z. Fodor and S. D. Katz, *Lattice determination of the critical point of QCD at finite T and mu*, *JHEP* **03** (2002) 014, [hep-lat/0106002].

[97] F. Csikor, G. I. Egri, Z. Fodor, S. D. Katz, K. K. Szabo and A. I. Toth, *The QCD equation of state at finite T and mu*, *Nucl. Phys. Proc. Suppl.* **119** (2003) 547–549, [hep-lat/0209114].

[98] C. R. Allton, S. Ejiri, S. J. Hands, O. Kaczmarek, F. Karsch, E. Laermann et al., *The QCD thermal phase transition in the presence of a small chemical potential*, *Phys. Rev.* **D66** (2002) 074507, [hep-lat/0204010].

[99] C. R. Allton, M. Doring, S. Ejiri, S. J. Hands, O. Kaczmarek, F. Karsch et al., *Thermodynamics of two flavor QCD to sixth order in quark chemical potential*, *Phys. Rev.* **D71** (2005) 054508, [hep-lat/0501030].

[100] R. V. Gavai and S. Gupta, *QCD at finite chemical potential with six time slices*, *Phys. Rev.* **D78** (2008) 114503, [0806.2233].

[101] MILC collaboration, S. Basak et al., *QCD equation of state at non-zero chemical potential*, *PoS* **LATTICE2008** (2008) 171, [0910.0276].

[102] O. Kaczmarek, F. Karsch, E. Laermann, C. Miao, S. Mukherjee, P. Petreczky et al., *Phase boundary for the chiral transition in (2+1) -flavor QCD at small values of the chemical potential*, *Phys. Rev.* **D83** (2011) 014504, [1011.3130].

[103] Z. Fodor, S. D. Katz and C. Schmidt, *The Density of states method at non-zero chemical potential*, *JHEP* **03** (2007) 121, [hep-lat/0701022].

[104] A. Alexandru, C. Gattringer, H. P. Schadler, K. Splittorff and J. J. M. Verbaarschot, *Distribution of Canonical Determinants in QCD*, *Phys. Rev.* **D91** (2015) 074501, [1411.4143].

[105] A. Alexandru, M. Faber, I. Horvath and K.-F. Liu, *Lattice QCD at finite density via a new canonical approach*, *Phys. Rev.* **D72** (2005) 114513, [hep-lat/0507020].

[106] S. Kratochvila and P. de Forcrand, *The Canonical approach to finite density QCD*, *PoS* **LAT2005** (2006) 167, [hep-lat/0509143].

[107] S. Ejiri, *Canonical partition function and finite density phase transition in lattice QCD*, *Phys. Rev.* **D78** (2008) 074507, [0804.3227].

[108] C. Gattringer, *New developments for dual methods in lattice field theory at non-zero density*, *PoS* **LATTICE2013** (2014) 002, [1401.7788].

[109] L. Scorzato, *The Lefschetz thimble and the sign problem*, *PoS* **LATTICE2015** (2016) 016, [1512.08039].

[110] A. Alexandru, G. Basar and P. Bedaque, *Monte Carlo algorithm for simulating fermions on Lefschetz thimbles*, *Phys. Rev.* **D93** (2016) 014504, [1510.03258].

[111] E. Seiler, D. Sexty and I.-O. Stamatescu, *Gauge cooling in complex Langevin for QCD with heavy quarks*, *Phys. Lett.* **B723** (2013) 213–216, [1211.3709].

[112] D. Sexty, *Simulating full QCD at nonzero density using the complex Langevin equation*, *Phys. Lett.* **B729** (2014) 108–111, [1307.7748].

[113] F. R. Brown, F. P. Butler, H. Chen, N. H. Christ, Z.-h. Dong, W. Schaffer et al., *On the existence of a phase transition for QCD with three light quarks*, *Phys. Rev. Lett.* **65** (1990) 2491–2494.

[114] Y. Aoki, G. Endrodi, Z. Fodor, S. D. Katz and K. K. Szabo, *The Order of the quantum chromodynamics transition predicted by the standard model of particle physics*, *Nature* **443** (2006) 675–678, [hep-lat/0611014].

[115] C. Bonati, M. D'Elia, M. Mariti, M. Mesiti, F. Negro and F. Sanfilippo, *Roberge-Weiss endpoint at the physical point of $N_f = 2 + 1$ QCD*, *Phys. Rev.* **D93** (2016) 074504, [1602.01426].

[116] C. Bonati, M. D'Elia, P. de Forcrand, O. Philipsen and F. Sanfilippo, *The chiral phase transition for two-flavour QCD at imaginary and zero chemical potential*, *PoS* **LATTICE2013** (2014) 219, [1311.0473].

[117] STAR collaboration, M. M. Aggarwal et al., *An Experimental Exploration of the QCD Phase Diagram: The Search for the Critical Point and the Onset of De-confinement*, 1007.2613.

[118] F. Karsch et al., *Conserved Charge Fluctuations from Lattice QCD and the Beam Energy Scan*, *Nucl. Phys.* **A956** (2016) 352–355, [1512.06987].

[119] B.-J. Schäfer, "Chiral thermodynamics in a finite box." Talk at HMEC, November, 2016.

[120] D. H. Rischke, *The Quark gluon plasma in equilibrium*, *Prog. Part. Nucl. Phys.* **52** (2004) 197–296, [nucl-th/0305030].

[121] M. Buballa, *NJL model analysis of quark matter at large density*, *Phys. Rept.* **407** (2005) 205–376, [hep-ph/0402234].

[122] N. Ishii, T. Doi, H. Iida, M. Oka, F. Okiharu, H. Suganuma et al., *Anisotropic lattice QCD studies of penta-quarks and tetra-quarks*, *AIP Conf. Proc.* **842** (2006) 492–494, [hep-lat/0601003].

[123] J.-J. Wu and B. S. Zou, *Penta-quark States with Strangeness, Hidden Charm and Beauty*, *JPS Conf. Proc.* **10** (2016) 010016, [1512.02770].

[124] E. Braaten and M. Lu, *Line Shapes of the Z(4430)*, *Phys. Rev.* **D79** (2009) 051503, [0712.3885].

[125] LHCb collaboration, R. Aaij et al., *Model-independent confirmation of the $Z(4430)^-$ state*, *Phys. Rev.* **D92** (2015) 112009, [1510.01951].

[126] D0 collaboration, V. M. Abazov et al., *Evidence for a $B_s^0\pi^\pm$ state*, *Phys. Rev. Lett.* **117** (2016) 022003, [1602.07588].

[127] C. P. et al. (Particle Data Group), *Review of Particle Physics*, *Chin. Phys. C* **40** (2016) 100001.

[128] Z. Fodor and C. Hoelbling, *Light Hadron Masses from Lattice QCD*, *Rev. Mod. Phys.* **84** (2012) 449, [1203.4789].

[129] E. Megias, E. Ruiz Arriola and L. L. Salcedo, *The Hadron Resonance Gas Model: Thermodynamics of QCD and Polyakov Loop*, 1207.7287.

[130] R. Dashen, S.-K. Ma and H. J. Bernstein, *S Matrix formulation of statistical mechanics*, *Phys. Rev.* **187** (1969) 345–370.

[131] V. Vovchenko, D. V. Anchishkin and M. I. Gorenstein, *Hadron Resonance Gas Equation of State from Lattice QCD*, *Phys. Rev.* **C91** (2015) 024905, [1412.5478].

[132] A. Andronic, P. Braun-Munzinger, J. Stachel and M. Winn, *Interacting hadron resonance gas meets lattice QCD*, *Phys. Lett.* **B718** (2012) 80–85, [1201.0693].

[133] A. Bazavov et al., *Additional Strange Hadrons from QCD Thermodynamics and Strangeness Freezeout in Heavy Ion Collisions*, *Phys. Rev. Lett.* **113** (2014) 072001, [1404.6511].

[134] R. Pasechnik and M. Šumbera, *Phenomenological review on Quark-Gluon Plasma: concepts vs observations*, 1611.01533.

[135] P. Braun-Munzinger and J. Stachel, *The quest for the quark-gluon plasma*, *Nature* **448** (2007) 302–309.

[136] B. S. S. Sarkar, H. Satz, *The physics of the quark-gluon plasma*, *Lect. Notes Phys.* **785** (2010) 369.

[137] J. Rafelski, ed., *Melting Hadrons, Boiling Quarks - From Hagedorn Temperature to Ultra-Relativistic Heavy-Ion Collisions at CERN*. Springer Open, 2016.

[138] Y. B. Zeldovich and A. D. Sakharov, *Mass formulas for mesons and baryons in the quark model*, *Acta Phys. Hung.* **22** (1967) 153–157.

[139] J. C. Collins and M. J. Perry, *Superdense Matter: Neutrons Or Asymptotically Free Quarks?*, *Phys. Rev. Lett.* **34** (1975) 1353.

[140] BRAHMS collaboration, I. Arsene et al., *Quark gluon plasma and color glass condensate at RHIC? The Perspective from the BRAHMS experiment*, *Nucl. Phys.* **A757** (2005) 1–27, [nucl-ex/0410020].

[141] B. B. Back et al., *The PHOBOS perspective on discoveries at RHIC*, *Nucl. Phys.* **A757** (2005) 28–101, [nucl-ex/0410022].

[142] STAR collaboration, J. Adams et al., *Experimental and theoretical challenges in the search for the quark gluon plasma: The STAR Collaboration's critical assessment of the evidence from RHIC collisions*, *Nucl. Phys.* **A757** (2005) 102–183, [nucl-ex/0501009].

[143] PHENIX collaboration, K. Adcox et al., *Formation of dense partonic matter in relativistic nucleus-nucleus collisions at RHIC: Experimental evaluation by the PHENIX collaboration*, *Nucl. Phys.* **A757** (2005) 184–283, [nucl-ex/0410003].

[144] J. Schukraft and R. Stock, *Toward the Limits of Matter: Ultra-relativistic nuclear collisions at CERN*, 1505.06853.

[145] M. Gyulassy and L. McLerran, *New forms of QCD matter discovered at RHIC*, *Nucl. Phys.* **A750** (2005) 30–63, [nucl-th/0405013].

[146] E. Shuryak, *Physics of Strongly coupled Quark-Gluon Plasma*, *Prog. Part. Nucl. Phys.* **62** (2009) 48–101, [0807.3033].

[147] M. H. Thoma, *The Quark-gluon-plasma liquid*, *J. Phys.* **G31** (2005) L7, [hep-ph/0503154].

[148] HotQCD collaboration, A. Bazavov et al., *Equation of state in (2+1)-flavor QCD*, *Phys. Rev.* **D90** (2014) 094503, [1407.6387].

[149] S. Borsanyi, Z. Fodor, C. Hoelbling, S. D. Katz, S. Krieg and K. K. Szabo, *Full result for the QCD equation of state with 2+1 flavors*, *Phys. Lett.* **B730** (2014) 99–104, [1309.5258].

[150] C. M. Hung and E. V. Shuryak, *Hydrodynamics near the QCD phase transition: Looking for the longest lived fireball*, *Phys. Rev. Lett.* **75** (1995) 4003–4006, [hep-ph/9412360].

[151] E. Braaten and R. D. Pisarski, *Simple effective Lagrangian for hard thermal loops*, *Phys. Rev.* **D45** (1992) R1827.

[152] J. O. Andersen and M. Strickland, *Resummation in hot field theories*, *Annals Phys.* **317** (2005) 281–353, [hep-ph/0404164].

[153] K. Kajantie, M. Laine, K. Rummukainen and M. E. Shaposhnikov, *Generic rules for high temperature dimensional reduction and their application to the standard model*, *Nucl.Phys.* **B458** (1996) 90–136, [hep-ph/9508379].

[154] E. Braaten and R. D. Pisarski, *Soft Amplitudes in Hot Gauge Theories: A General Analysis*, *Nucl. Phys.* **B337** (1990) 569–634.

[155] A. Rebhan, *Hard thermal loops and QCD thermodynamics*, in *QCD perspectives on hot and dense matter. Proceedings, NATO Advanced Study Institute, Summer School, Cargese, France, August 6-18, 2001*, pp. 327–351, 2001. hep-ph/0111341.

[156] R. D. Pisarski, *Scattering Amplitudes in Hot Gauge Theories*, *Phys. Rev. Lett.* **63** (1989) 1129.

[157] M. Gell-Mann and K. A. Brueckner, *Correlation Energy of an Electron Gas at High Density*, *Phys. Rev.* **106** (1957) 364–368.

[158] I. T. Drummond, R. R. Horgan, P. V. Landshoff and A. Rebhan, *Foam diagram summation at finite temperature*, *Nucl. Phys.* **B524** (1998) 579–600, [hep-ph/9708426].

[159] B. Beinlich, F. Karsch, E. Laermann and A. Peikert, *String tension and thermodynamics with tree level and tadpole improved actions*, *Eur. Phys. J.* **C6** (1999) 133–140, [hep-lat/9707023].

[160] J. O. Andersen, E. Braaten and M. Strickland, *Screened perturbation theory to three loops*, *Phys. Rev.* **D63** (2001) 105008, [hep-ph/0007159].

[161] K. Kajantie, M. Laine, K. Rummukainen and Y. Schroder, *The Pressure of hot QCD up to g6 ln(1/g)*, *Phys. Rev.* **D67** (2003) 105008, [hep-ph/0211321].

[162] H. T. Ding, S. Mukherjee, H. Ohno, P. Petreczky and H. P. Schadler, *Diagonal and off-diagonal quark number susceptibilities at high temperatures*, *Phys. Rev.* **D92** (2015) 074043, [1507.06637].

[163] R. Bellwied, S. Borsanyi, Z. Fodor, S. D. Katz, A. Pasztor, C. Ratti et al., *Fluctuations and correlations in high temperature QCD*, *Phys. Rev.* **D92** (2015) 114505, [1507.04627].

[164] N. Haque, A. Bandyopadhyay, J. O. Andersen, M. G. Mustafa, M. Strickland and N. Su, *Three-loop HTLpt thermodynamics at finite temperature and chemical potential*, *JHEP* **05** (2014) 027, [1402.6907].

[165] S. Borsányi, *Fluctuations at finite temperature and density*, *PoS* **LATTICE2015** (2016) 015, [1511.06541].

[166] O. Wantz and E. P. S. Shellard, *Axion Cosmology Revisited*, *Phys. Rev.* **D82** (2010) 123508, [0910.1066].

[167] R. D. Peccei, *QCD, strong CP and axions*, *J. Korean Phys. Soc.* **29** (1996) S199–S208, [hep-ph/9606475].

[168] C. G. Callan, Jr., R. F. Dashen and D. J. Gross, *The Structure of the Gauge Theory Vacuum*, *Phys. Lett.* **B63** (1976) 334–340.

[169] R. D. Peccei, *The Strong CP problem and axions*, *Lect. Notes Phys.* **741** (2008) 3–17, [hep-ph/0607268].

[170] R. D. Peccei and H. R. Quinn, *Constraints Imposed by CP Conservation in the Presence of Instantons*, *Phys. Rev.* **D16** (1977) 1791–1797.

[171] S. Weinberg, *A New Light Boson?*, *Phys. Rev. Lett.* **40** (1978) 223–226.

[172] F. Wilczek, *Problem of Strong p and t Invariance in the Presence of Instantons*, *Phys. Rev. Lett.* **40** (1978) 279–282.

[173] G. Odyniec, *Future of the beam energy scan program at RHIC*, *EPJ Web Conf.* **95** (2015) 03027.

[174] R. Bellwied, S. Borsanyi, Z. Fodor, J. Gunther, S. D. Katz, A. Pasztor et al., *Towards the QCD phase diagram from analytical continuation*, *Nucl. Phys.* **A956** (2016) 797–800, [1601.00466].

[175] J. Günther, R. Bellwied, S. Borsanyi, Z. Fodor, S. D. Katz, C. Ratti et al., *The curvature of the crossover line in the (T, μ)-phase diagram of QCD*, *PoS* **LATTICE2015** (2016) 142.

[176] J. P. Blaizot, E. Iancu and A. Rebhan, *Quark number susceptibilities from HTL resummed thermodynamics*, *Phys. Lett.* **B523** (2001) 143–150, [hep-ph/0110369].

[177] J. Günther, *The QCD equation of state at finite density from analytical continuation*, in *International Symposium on Lattice Field Theory*, 2016.

[178] C. Morningstar and M. J. Peardon, *Analytic smearing of SU(3) link variables in lattice QCD*, *Phys. Rev.* **D69** (2004) 054501, [hep-lat/0311018].

[179] C. McNeile, C. T. H. Davies, E. Follana, K. Hornbostel and G. P. Lepage, *High-Precision c and b Masses, and QCD Coupling from Current-Current Correlators in Lattice and Continuum QCD*, *Phys. Rev.* **D82** (2010) 034512, [1004.4285].

[180] M. D'Elia and F. Sanfilippo, *The Order of the Roberge-Weiss endpoint (finite size transition) in QCD*, *Phys. Rev.* **D80** (2009) 111501, [0909.0254].

[181] C. Pinke and O. Philipsen, *The nature of the Roberge-Weiss transition in $N_f = 2$ QCD with Wilson fermions*, *PoS* **LATTICE2013** (2014) 209.

[182] L.-K. Wu and X.-F. Meng, *Nature of Roberge-Weiss transition endpoints for heavy quarks in $N_f = 2$ lattice QCD with Wilson fermions*, *Phys. Rev.* **D90** (2014) 094506, [1405.2425].

[183] L. Cosmai, A. Papa and P. Cea, *Curvature of the pseudocritical line in (2+1)-flavor QCD with HISQ fermions*, *PoS* **LATTICE2015** (2016) 143, [1510.06847].

[184] P. Cea, L. Cosmai and A. Papa, *Critical line of 2+1 flavor QCD: Toward the continuum limit*, *Phys. Rev.* **D93** (2016) 014507, [1508.07599].

[185] C. Bonati, M. D'Elia, M. Mariti, M. Mesiti, F. Negro and F. Sanfilippo, *Curvature of the chiral pseudocritical line in QCD: Continuum extrapolated results*, *Phys. Rev.* **D92** (2015) 054503, [1507.03571].

[186] M. D'Elia, C. Bonati, M. Mariti, M. Mesiti, F. Negro and F. Sanfilippo, *The QCD pseudocritical line from imaginary chemical potentials*, *PoS* **CPOD2014** (2015) 013.

[187] M. Mariti, C. Bonati, M. D'elia, M. Mesiti, F. Negro and F. Sanfilippo, *Magnetic properties of the QCD medium*, *PoS* **LATTICE2014** (2015) 237.

[188] C. Schmidt, *The QCD equation of state and fluctuations of conserved charges at non-zero temperature and density* , in *Quark confinement and the hadron spectrum*, 2016.

[189] G. Endrodi, Z. Fodor, S. D. Katz and K. K. Szabo, *The QCD phase diagram at nonzero quark density*, *JHEP* **04** (2011) 001, [1102.1356].

[190] F. Becattini, J. Manninen and M. Gazdzicki, *Energy and system size dependence of chemical freeze-out in relativistic nuclear collisions*, *Phys. Rev.* **C73** (2006) 044905, [hep-ph/0511092].

[191] J. Cleymans, H. Oeschler, K. Redlich and S. Wheaton, *Comparison of chemical freeze-out criteria in heavy-ion collisions*, *Phys. Rev.* **C73** (2006) 034905, [hep-ph/0511094].

[192] A. Andronic, P. Braun-Munzinger and J. Stachel, *Thermal hadron production in relativistic nuclear collisions: The Hadron mass spectrum, the horn, and the QCD phase transition*, *Phys. Lett.* **B673** (2009) 142–145, [0812.1186].

[193] F. Becattini, M. Bleicher, T. Kollegger, M. Mitrovski, T. Schuster and R. Stock, *Hadronization and Hadronic Freeze-Out in Relativistic Nuclear Collisions*, *Phys. Rev.* **C85** (2012) 044921, [1201.6349].

[194] M. Bluhm, P. Alba, W. Alberico, R. Bellwied, V. M. Sarti, M. Nahrgang et al., *Parametrization for chemical freeze-out conditions from net-charge fluctuations measured at RHIC*, *J. Phys. Conf. Ser.* **612** (2015) 012041, [1412.5934].

[195] C. S. Fischer, J. Luecker and C. A. Welzbacher, *Locating the critical end point of QCD*, *Nucl. Phys.* **A931** (2014) 774–779, [1410.0124].

[196] C. S. Fischer, J. Luecker and C. A. Welzbacher, *Phase structure of three and four flavor QCD*, *Phys. Rev.* **D90** (2014) 034022, [1405.4762].

[197] R. Hentschke, *Statistische Mechanik*. Wiley-VCH, 2004.

[198] BNL-Bielefeld-CCNU collaboration, P. Hegde, *The QCD equation of state to $\mathcal{O}(\mu_B^4)$*, *PoS* **LATTICE2014** (2014) 226, [1412.6727].

[199] T. Toimela, *The Next Term in the Thermodynamic Potential of QCD*, *Phys. Lett.* **B124** (1983) 407–409.

[200] B. Friman, F. Karsch, K. Redlich and V. Skokov, *Fluctuations as probe of the QCD phase transition and freeze-out in heavy ion collisions at LHC and RHIC*, *Eur. Phys. J.* **C71** (2011) 1694, [1103.3511].

[201] BNL–Bielefeld–CCNU collaboration, P. Hegde, *The QCD equation of state to $\mathcal{O}(\mu_B^4)$ from lattice QCD*, *Nucl. Phys.* **A931** (2014) 851–855, [1408.6305].

[202] S. Borsanyi, G. Endrodi, Z. Fodor, S. D. Katz, S. Krieg, C. Ratti et al., *QCD equation of state at nonzero chemical potential: continuum results with physical quark masses at order mu^2*, *JHEP* **08** (2012) 053, [1204.6710].

[203] P. Alba, W. Alberico, R. Bellwied, M. Bluhm, V. Mantovani Sarti, M. Nahrgang et al., *Freeze-out conditions from net-proton and net-charge fluctuations at RHIC*, *Phys. Lett.* **B738** (2014) 305–310, [1403.4903].

[204] M. Luscher, *Exact chiral symmetry on the lattice and the Ginsparg-Wilson relation*, *Phys. Lett.* **B428** (1998) 342–345, [hep-lat/9802011].

[205] P. Hasenfratz, V. Laliena and F. Niedermayer, *The Index theorem in QCD with a finite cutoff*, *Phys. Lett.* **B427** (1998) 125–131, [hep-lat/9801021].

[206] D. H. Adams, *Axial anomaly and topological charge in lattice gauge theory with overlap Dirac operator*, *Annals Phys.* **296** (2002) 131–151, [hep-lat/9812003].

[207] M. Lüscher, *Properties and uses of the Wilson flow in lattice QCD*, *JHEP* **08** (2010) 071, [1006.4518].

[208] S. Durr and C. Hoelbling, *A Comparative study of overlap and staggered fermions in the Schwinger model*, *Nucl. Phys. Proc. Suppl.* **140** (2005) 680–682, [hep-lat/0408039].

[209] S. Borsanyi, M. Dierigl, Z. Fodor, S. D. Katz, S. W. Mages, D. Nogradi et al., *Axion cosmology, lattice QCD and the dilute instanton gas*, *Phys. Lett.* **B752** (2016) 175–181, [1508.06917].

[210] G. 't Hooft, *Computation of the Quantum Effects Due to a Four-Dimensional Pseudoparticle*, *Phys. Rev.* **D14** (1976) 3432–3450.

[211] C. G. Callan, Jr., R. F. Dashen and D. J. Gross, *Toward a Theory of the Strong Interactions*, *Phys. Rev.* **D17** (1978) 2717.

[212] ALPHA collaboration, S. Schaefer, R. Sommer and F. Virotta, *Critical slowing down and error analysis in lattice QCD simulations*, *Nucl. Phys.* **B845** (2011) 93–119, [1009.5228].

[213] A. Laio, G. Martinelli and F. Sanfilippo, *Metadynamics surfing on topology barriers: the CP^{N-1} case*, *JHEP* **07** (2016) 089, [1508.07270].

[214] M. Luscher and S. Schaefer, *Lattice QCD without topology barriers*, *JHEP* **07** (2011) 036, [1105.4749].

[215] S. Mages, B. C. Toth, S. Borsanyi, Z. Fodor, S. Katz and K. K. Szabo, *Lattice QCD on Non-Orientable Manifolds*, 1512.06804.

[216] J. Frison, R. Kitano, H. Matsufuru, S. Mori and N. Yamada, *Topological susceptibility at high temperature on the lattice*, *JHEP* **09** (2016) 021, [1606.07175].

[217] H. Akaike, *Information theory and an extension of the maximum likelihood principle*. Springer, 1992.

[218] J. Jaeckel and J. Redondo, *Resonant to broadband searches for cold dark matter consisting of weakly interacting slim particles*, *Phys. Rev.* **D88** (2013) 115002, [1308.1103].

[219] B. C. Toth, "private converstation." October, 2016.

[220] S. J. Byrnes, *Multilayer optical calculations*, 1603.02720.

[221] A. E. Nelson and J. Scholtz, *Dark Light, Dark Matter and the Misalignment Mechanism*, *Phys. Rev.* **D84** (2011) 103501, [1105.2812].

[222] M. Bullimore, J. P. Conlon and L. T. Witkowski, *Kinetic mixing of U(1)s for local string models*, *JHEP* **11** (2010) 142, [1009.2380].

[223] M. Goodsell, J. Jaeckel, J. Redondo and A. Ringwald, *Naturally Light Hidden Photons in LARGE Volume String Compactifications*, *JHEP* **11** (2009) 027, [0909.0515].

[224] S. A. Abel, M. D. Goodsell, J. Jaeckel, V. V. Khoze and A. Ringwald, *Kinetic Mixing of the Photon with Hidden U(1)s in String Phenomenology*, *JHEP* **07** (2008) 124, [0803.1449].

[225] D. Horns, J. Jaeckel, A. Lindner, A. Lobanov, J. Redondo and A. Ringwald, *Searching for WISPy Cold Dark Matter with a Dish Antenna*, *JCAP* **1304** (2013) 016, [1212.2970].

[226] P. Arias, D. Cadamuro, M. Goodsell, J. Jaeckel, J. Redondo and A. Ringwald, *WISPy Cold Dark Matter*, *JCAP* **1206** (2012) 013, [1201.5902].

[227] J. Jaeckel, *A force beyond the Standard Model - Status of the quest for hidden photons*, *Frascati Phys. Ser.* **56** (2012) 172–192, [1303.1821].

[228] E. C. G. Stueckelberg, *Interaction forces in electrodynamics and in the field theory of nuclear forces*, *Helv. Phys. Acta* **11** (1938) 299–328.

[229] D. Feldman, Z. Liu and P. Nath, *The Stueckelberg Z-prime Extension with Kinetic Mixing and Milli-Charged Dark Matter From the Hidden Sector*, *Phys. Rev.* **D75** (2007) 115001, [hep-ph/0702123].

[230] J. Jaeckel and J. Redondo, *An antenna for directional detection of WISPy dark matter*, *JCAP* **1311** (2013) 016, [1307.7181].

Erklärung

Hiermit erkläre ich, Jana Günther, dass ich das Thema

Lattice investigations of the QCD phase diagram

selbstständig und ohne fremde Hilfe bearbeitet, nur die angegebenen Quellen und Hilfsmittel benutzt und alle wörtlich oder inhaltlich übernommenen Literaturstellen als solche gekennzeichnet habe.

Wuppertal, den 15. Dezember 2016

Jana Günther